Fast Wavelet Solution for Electromagnetic Integral Equations

by

Wujun Quan

A Thesis Submitted to the Faculty of Graduate Studies of the University of Manitoba in Partial Fulfillment of the Requirements for the Degree of

DOCTOR OF PHILOSOPHY

Department of Electrical and Computer Engineering

The University of Manitoba

Winnipeg, Manitoba, Canada

THE UNIVERSITY OF MANITOBA

FACULTY OF GRADUATE STUDIES

*****

COPYRIGHT PERMISSION

Fast Wavelet Solution for Electromagnetic Integral Equations

BY

Wujun Quan

A Thesis/Practicum submitted to the Faculty of Graduate Studies of The University of Manitoba in partial fulfillment of the requirement of the degree

Of

DOCTOR OF PHILOSOPHY

TABLE OF CONTENTS

Abstract

Numerical techniques that employ integral equation formulations are favorably used for the analysis of electromagnetic radiation and scattering. The conventional method of moments yields full dense matrix equations whose numerical computation is expensive. In the past decade, considerable efforts have been made to further reduce the computational cost. One of the most recent fast algorithms available in literature is the use of wavelets, which is gaining an increasing amount of attention from researchers in computational electromagnetics community.

In this thesis, wavelet applications for a fast solution of electromagnetic integral equations are thoroughly studied. Wavelet bases offer the advantage of highly sparse moment-method matrix equations, which can be solved efficiently. The performance of semi-orthogonal and orthogonal wavelets when used for a fast solution of Fredholm integral equations, which arise in the formulation of wave scattering by two-dimensional conducting cylinders, is first investigated. This basic research consists in the analysis of matrix sparsity, solution accuracy, and matrix condition number, and provides a guideline for the selection of wavelets used for the fast solution of electromagnetic integral equations. It was discovered that the orthogonal wavelets are optimal in terms of the condition number. Then, two kinds of wavelet applications to the method of moments, i.e., the matrix transform approach and the change-of-bases scheme, are compared for the first time for the solution of coupled scalar integral equations governing the problem of scattering by two-dimensional dielectric bodies. The study shows that the change-of-bases scheme gives rise to a better performance in terms of matrix sparsity, while the matrix transform approach provides a

problem-independent transform mechanism. Further, the matrix transform approach with orthogonal wavelets is extended to a fast analysis of the scattering by arbitrary bodies of revolution, whose mathematical model contains coupled vector integro-differential equations. Finally, the application of wavelets is effectively used for a fast solution of scattering problems by 3-D inhomogeneous bodies of arbitrary shape, which is formulated as a volume integral equation involving equivalent sources.

Several solution methods for the resultant sparse matrix equations, obtained with the use of wavelets, are also investigated. The conjugate or bi-conjugate gradient (BiCG) iterative algorithms are popular solvers used in the computational electromagnetics community. A sparse conjugate gradient algorithm is effectively used for a fast solution of Fredholm integral equations. A sparse BiCG, with an efficient wavelet transform technique for Toeplitz matrices, is also presented for the fast solution of 3-D volume integral equations associated with the scattering problem by 3-D inhomogeneous bodies. A solution technique using a sparse generalized minimal residual method is demonstrated for the analysis of scattering by conducting bodies of revolution, which is described by a vector integro-differential equation. A sparse LU solver with an approximate minimum degree ordering algorithm is proposed for the analysis of scattering by dielectric bodies of revolution, involving coupled vector integro-differential equations, where the resultant moment-method matrices inherently possess a higher condition number.

Acknowledgements

The author wishes to express his sincere gratitude to his advisor, Dr. I. R. Ciric, for his invaluable advice, suggestions, and encouragement throughout the Ph.D. research program.

Special thanks are due to Professors R. Azad, G. Bridges, and W. Kinsner, the members of the advisory committee of his Ph.D. thesis, for their helpful suggestions, time, and supervision.

Financial support in the form of a research assistantship from the NSERC research grant of Dr. I. R. Ciric, a graduate fellowship from the University of Manitoba, teaching assistantships from the Department of Electrical and Computer Engineering, and a partial tuition from the Manitoba HVDC Research Centre Inc., is greatly acknowledged.

Finally, the author wishes to convey his special thanks to his wife, Linda Y. Jin, and daughter Sophia Y. Quan, for their understanding and support in the course of this research work.

List of Tables

List of Figures

Chapter 1

INTRODUCTION

§1.1. Forword

Research in the area of computational electromagnetics is actively pursued nowadays not only by electrical engineers, but also by mathematicians and computer scientists, and numerical techniques for solving electromagnetic field problems have been intensely studied in the last few decades. This is due to the importance of this research in many practical areas, such as prediction of the radar cross section (RCS) of large complex objects, like aircraft, wave scattering analysis for stealth technology, interaction of the electromagnetic waves with biological media, and propagation of signals in high-speed and microwave circuits [61].

Numerical techniques that utilize integral equation formulations have been widely used for the analysis of radiation and scattering by bodies of simple or complex shape, since the integral equation formulations reduce the domain of the operator equation to a finite and often a smaller one than that in the partial differential equation approach, with all boundary conditions implicitly taken into account. However, the integral equation approach leads to full dense matrices and thus yields a special category of computational technologies, especially for electrically large field structures. Considerable efforts have been made by many researchers to reduce the computational complexity recently, notably by developing various conjugate gradient-fast Fourier transform (CG-FFT) methods, fast multipole

methods, multilevel algorithms, and by the use of wavelets in the method of moments (MoM).

In this thesis, the use of wavelets for the fast solution of electromagnetic integral equations is investigated. In the following Sections, the existing fast solution techniques and the current research status on the wavelet applications in the MoM are reviewed, and the objective of the research work is delineated.

§1.2. Review of Fast Solution Techniques for Integral Equations

The integral equation approach leads to a dense matrix equation whose numerical solution requires $O(N^3)$ arithmetic operations for direct solvers and $O(N^2)$ operations for iterative solvers, where N is the number of unknowns. The following algorithms have been proposed to further reduce the computational complexity.

CG-FFT Methods

For Toeplitz matrices, the fast Fourier transform (FFT) can be used to perform the matrix-vector products with $O(N \log N)$ arithmetic operations. This technique is usually combined with conjugate gradient (CG) iterative algorithms yielding the so-called CG-FFT methods, which need only a computer memory of $O(N)$.

The CG-FFT methods have been effectively used for a fast solution of electromagnetic integral equations. Its application for planar and two-dimensional radiation problems can be found in [19], [21], and for the computation of microstrip S-parameters in [36]. For three-dimensional scattering formulated in terms of integral equations, various schemes have also been proposed in the past to obtain (block) Toeplitz MoM matrices, including the

point-matching method, Galerkin's method with the rooftop basis functions [48], and a weak form of CG-FFT [27]. The CG-FFT method was also used to expedite the solution of scattering by a cluster of randomly distributed spheres and randomly distributed cylinders, whose scattering is characterized by the so-called T matrix [58]. When the subscatterers are not in a regular array, a precorrected method is used to derive a Toeplitz matrix, which employs the fast multipole translation operators to shift the centers of the subscatterers. It has been reported that the CG-FFT method can be applied to the scattering by inhomogeneous bodies with high contrast [61].

Fast Multipole Methods

Like the CG-FFT method, the fast multipole method (FMM), initiated in [22], achieves its speed by using an indirect fast computation of matrix-vector products in the context of an iterative solution for a matrix equation with $O(N^{1.5})$ arithmetic operations [34], [61]. The main idea of the FMM is to reduce the number of scattering centers by first dividing the subscatterers into groups, and then translating the centers of a group to its inner subscatterers by using translation operators, which are derived analytically by virtue of the multipole expansion of the integral kernels.

Several techniques have been proposed to improve the efficiency of the FMM during the past decade. The ray-propagation algorithm [39] is proposed to further reduce the complexity of a matrix-vector multiply to $O(N^{4/3})$ operations, where the number of translation operators is reduced by employing the ray physics. The multilevel FMM uses concepts from the multiscale analysis, such that the complexity of a matrix-vector multiply is reduced to $O(N \log N)$ [47].

Multilevel Algorithms

Unlike the CG-FFT method and the FMM, which reduce the complexity of the matrix-vector products, the multilevel algorithm accelerates the convergence rate of an iterative method by correcting the defect (residual error) at a finer level with lower level solutions based on a hierarchy of nested approximation spaces [9]. A solution to a problem P is sought for by first defining a hierarchical set of problems $P = P_0, P_1, \cdots, P_L$, where P_i is in some sense a coarser approximation of P_{i-1}. The solution of P_L is first found and, then, level-by-level, the solution of P_{i-1} is obtained from that of P_i. The convergence and computational complexity of such algorithms was studied in [15], [17], [18].

One popular approach to construct a multilevel algorithm is to use simple basis functions such as rectangular or triangular pulse functions on multiple grids, such a multigrid method being advocated in [14] for solving sparse systems of equations arising from the discretization of partial differential equations. This algorithm was first applied for a fast solution of the Fredholm integral equations in [8] and [17], and has been recently employed for the solution of electromagnetic integral equations in [31] and [78].

Alternatively, hierarchical bases independent of grids such as the multi-p basis [68] can be utilized to construct the multilevel algorithm. The multi-p hierarchical bases are constructed with piecewise Legendre polynomials, and have been widely used in the p-version of the finite element method. These bases have been used in the integral equations to treat singularities, e.g. for problems in mechanical engineering, relative to polynomial domains. Our paper [68] exhibits the efficiency of the two-level algorithm employing the multi-p bases.

The key in the construction of the multilevel algorithms is to find efficient multilevel operators, i.e., projection and prolongation operators. In the multilevel FMM in [47], these are obtained from analytical translation operators, the efficiency of the procedure being illustrated by implementing a two-level algorithm.

Use of Wavelets

There have been many attempts to generate sparse matrices by transforming appropriately the original dense matrices, with most of their elements having very small values that can be neglected, and thus the matrix-vector products can be expedited by employing a sparse matrix technology. Among these sparse matrix approaches, the use of wavelets gained an increasing popularity.

A sparse preconditioner was used in [52], where a threshold procedure is directly applied to a matrix equation. As a result, the sparsity of the resultant matrices is problem dependent and limited. Impedance matrix localization method [32] has been proposed as a remedy, where a local cosine transform (a windowed Fourier transform) is used to transform a dense matrix into a sparse one. It has been reported that highly sparse matrices can be obtained for problems with smooth geometry.

The use of wavelets was first proposed in [24] for a fast solution of a class of integral equations with Calderon-Zygmund type of kernel, and then introduced [33] to the community of computational electromagnetics for a fast solution of the Fredholm integral equation of the first kind arising in the analysis of electromagnetic wave scattering problems. Due to the wavelet properties, i.e., orthogonality, localization, and vanishing moments, the

moment-method matrix equations represented in the wavelet domain have a larger content of elements with very small values.

§1.3. Research Status On the Wavelet Applications in the MoM

Two kinds of wavelets, orthogonal and semi-orthogonal, are frequently used in computational electromagnetics. The semi-orthogonal wavelets (SOW) are symmetric, compactly supported, and closed-form expressions are available. SOW were used for the solution of Fredholm integral equations in direct way in [44]. A SOW matrix transformation was also implemented in [63] for the electromagnetic scattering by systems of very thin parallel conducting cylinders and the matrix sparsity was analyzed quantitatively as a function of the threshold value.

The implementation of orthogonal wavelets with infinite support width such as the Battle-Lemarié wavelets and the Meyer wavelets requires a truncation operation that causes a certain numerical error [42]. In contrast, the Daubechies' orthogonal wavelets (DOW) that are compactly supported can be used without any truncation. The efficiency of the DOW for the solution of integral equations was analyzed in [45] for the scattering by conducting cylinders. The resulting sparse matrix equations were solved by using the conjugate gradient method with storage space required only for the nonzero entries of the sparse matrix.

The performance of SOW was compared with that of the Battle-Lemarié orthogonal wavelets in [64], where wavelets are employed in a direct way. SOW was also compared with the DOW in [63], where a matrix transformation was implemented to reduce the computational effort necessary to perform numerical integrations. It has been reported that

the use of the SOW yields more highly sparse matrices and better solution accuracy when a direct solver is adopted than the use of orthogonal wavelets.

Wavelet packet transforms have also been implemented in order to obtain more highly sparse matrices. Several algorithms were designed to select the best bases for a given problem, where the wavelet packet decomposition tree is optimized by minimizing a specified cost function. A procedure classified as "top-down near-best basis algorithm", with an additive cost function, was implemented in [59], [67], which is dependent on the excitation vector, the best bases being obtained by performing an optimization procedure on a given excitation vector in the MoM equations. An iterative algorithm for selecting best bases was also proposed in [66], where the residual error of the transformed MoM equations is defined as the cost function. In [74], an additive energy function, which is directly related to the sparsity of the transformed impedance matrices, was employed to seek for the best wavelet packet bases. One drawback of the above algorithms is the additional computational cost of searching procedure for the best wavelet packet decomposition tree. Recognizing this, a predefined wavelet packet transform algorithm was proposed in [75], [84], where the wavelet packet decomposition tree is prescribed based on the knowledge of Green's functions.

The condition number of wavelet transform matrices has been studied in our papers [70], [71], for TE wave scattering and in [72] for TM wave scattering by electrically large conducting cylinders. It was pointed out for the first time that orthogonal wavelets are better than semi-orthogonal wavelets in terms of the condition number. The same result has also been presented in [77] for the scattering by circular and L-shaped conducting, and in [79] cylinders for the scattering by 2-D metal strips.

Mathematical models treated by using wavelets are Fredholm integral equations associated with electromagnetic scattering by two-dimensional objects [33], [37], [44], [49] and by rough surfaces [76], coupled surface integral equations describing the eddy current problem of a two-conductor system in the low frequency area [57], scalar integro-differential equations arising from the thin-wire antenna problems [62], [64], and 3-D integral equations governing the scattering by conducting rectangular cavities [84].

Wavelet application in computational electromagnetics has been expanded to many areas such as the full wave analysis of microstrip floating line structures [41], boundary element analysis for multiconductor transmission lines in multilayered dielectrics [42], the computation of parameter matrices of multiple lossy transmission lines with the application of adaptive wavelet expansion method [38], and the waveguide mode identification [35], [40] and analysis of multiport structures using the semi-orthogonal wavelets with 2 vanishing moments [80]. Dielectric resonators have also been studied based on two-dimensional orthogonal wavelet transform algorithm [54]. However, the following issues have not been studied before we started our research:

- Systematic study of SOW in comparison with the DOW when used for the solution of integral equations;
- Application to coupled integral equations in high frequency electromagnetics;
- Application to coupled vector integro-differential equations;
- Application to the problems of three-dimensional electromagnetic scattering; and
- Efficient solution techniques for the sparse matrix equations obtained with the use of wavelets.

§1.4. Outline of the Work

With an attempt to make contributions to the problems listed above, the thesis is organized as follows:

In Chapter 2, wavelets are first introduced through reviewing hierarchical bases employed in computational electromagnetics. Then, features of typical families of wavelets available in literature are compared. Lastly, a review on the use of wavelets in the MoM for a fast solution of electromagnetic integral equations is presented.

Chapter 3 presents a performance comparison between semi-orthogonal and orthogonal wavelets when used for the solution of Fredholm integral equations, which arise from the scattering problem by two-dimensional conducting bodies. This comparison is based on the analysis of matrix sparsity, solution accuracy, and matrix condition number, and provides a guideline on the selection of wavelets used for the fast solution of electromagnetic integral equations.

In Chapter 4, two wavelet applications in the MoM, i.e., the matrix transform approach and the change-of-basis scheme by using orthogonal wavelets, are effectively used for the analysis of electromagnetic scattering by two-dimensional dielectric bodies, whose mathematical formulation is based on coupled scalar integral equations, and their performances are compared for the first time.

In Chapter 5, the matrix transform approach with orthogonal wavelets is extended to the problem of scattering by arbitrary bodies of revolution (BOR), which is formulated as coupled vector integro-differential equations. An efficient solution technique that uses a sparse generalized minimal residual (GMRES) method, which converges faster than other

iterative methods [65], is demonstrated for the analysis of scattering by conducting BORs, where the mathematical model is reduced to a vector integral-differential equation. As well, a sparse LU solver with an approximate minimum degree ordering algorithm [56] is proposed for the analysis of scattering by dielectric bodies of revolution, where the moment-method matrices inherently possess a higher condition number.

In Chapter 6, the use of wavelets is further extended to the analysis of three-dimensional electromagnetic scattering by inhomogeneous bodies of arbitrary geometry. The fields scattered by such objects are modeled using a volume integral equation involving equivalent sources. An efficient wavelet transform algorithm designed for Toeplitz matrices [73] is employed to speed up the 3-D wavelet transformation of MoM matrix equations and a sparse bi-conjugate gradient solver is utilized to obtain a fast solution of the resultant sparse matrix equations.

Conclusions of this research work as well as the related future work are summarized in Chapter 7. A detailed review of various wavelets, i.e., bi-orthogonal, semi-orthogonal, and orthogonal wavelets, with some examples, is provided in Appendix A. The computational algorithm for the semi-orthogonal wavelets is presented in Appendix B, and the structure charts of the computer programs used in this thesis are described in Appendix C.

Chapter 2

THEORY

In this chapter, wavelets are described through reviewing hierarchical bases employed in computational electromagnetics. Salient features of various wavelets are studied, and their applications in the MoM for fast solution of electromagnetic integral equations are summarized and discussed.

§2.1. Hierarchical Bases

Hierarchical bases generate a sequence of successive approximation spaces of $L^2(R)$

$$V_0 \subset V_1 \subset \cdots \subset V_{j-1} \subset V_j \subset \cdots \tag{2.1}$$

which constitutes a multiresolution analysis. Each subsequent space is generated as

$$V_{j+1} = V_j \oplus W_j \tag{2.2}$$

where W_j is the complement space of V_j in V_{j+1}, the symbol $\oplus$ stands for the direct sum and $V_j = Span\{\phi_j, j \in Z\}$, $W_j = Span\{\psi_j, j \in Z\}$, with properly chosen basis functions ϕ and ψ, and Z being the set of integers. Consequently, we have the hierarchical decomposition of V_m as

$$\boldsymbol{V}_m = \boldsymbol{V}_0 \oplus \boldsymbol{W}_0 \oplus \boldsymbol{W}_1 \oplus \cdots \oplus \boldsymbol{W}_{m-1} \tag{2.3}$$

Hierarchical basis functions have been frequently used in computational electromagnetics to construct multilevel iterative methods or to obtain sparse MoM matrix equations, which accelerate the solution speed. So far, various basis functions ϕ and ψ have been proposed by many researchers.

§2.1.1. Classical Hierarchical Bases

There are two classical hierarchical bases: one is constructed with the rectangular pulse function, and the other is constructed from the triangular pulse function. The hierarchical basis based on the rectangular pulse function is used in [31] to construct a multilevel algorithm for the solution of electromagnetic integral equations. The triangular pulse function possesses multilevel splitting property, i.e., $\phi(x) = 0.5\phi(2x+1) + \phi(2x) + 0.5\phi(2x-1)$ as shown in Fig. 2.1(a). Starting with the basis $\boldsymbol{V}_0$ and its complement $\boldsymbol{W}_0$, a class of hierarchical bases $\boldsymbol{W}_k$, $k = 1, 2, \cdots$ can be constructed as shown in Fig. 2.1(b), with triangular functions on the different level of grids, yields the hierarchical decomposition in (2.3).

In [78], the hierarchical bases are employed to formulate an adaptive multiscale moment method. It is noted that the two classical hierarchical bases are grid-dependant, and the relevant multilevel algorithms being called multigrid methods [14], [17].

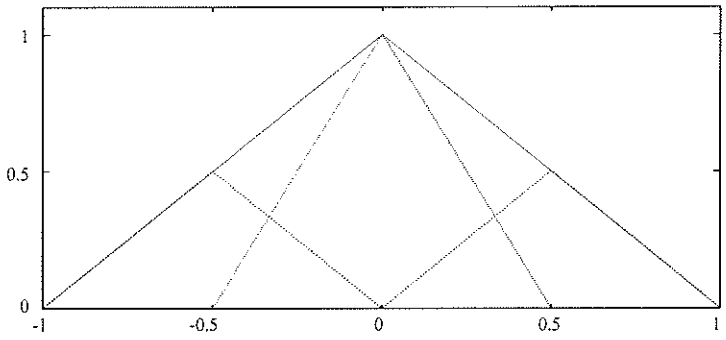

(a)

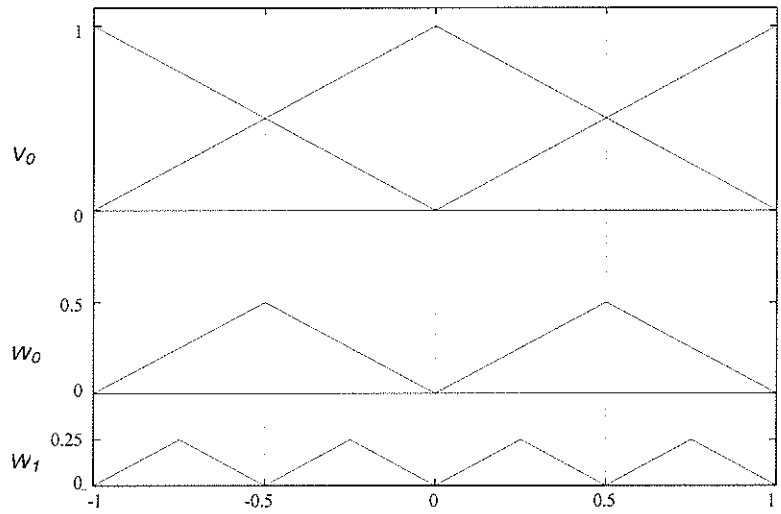

(b)

Fig. 2.1. Multilevel splitting triangular pulse functions $\phi(x)$: (a) $\phi(x)$ has the representation $\phi(x) = 0.5\phi(2x+1) + \phi(2x) + 0.5\phi(2x-1)$; (b) Hierarchical subspaces $\boldsymbol{V}_0$ and $\boldsymbol{W}_i$, $i = 0,1$ in the interval [-1, 1].

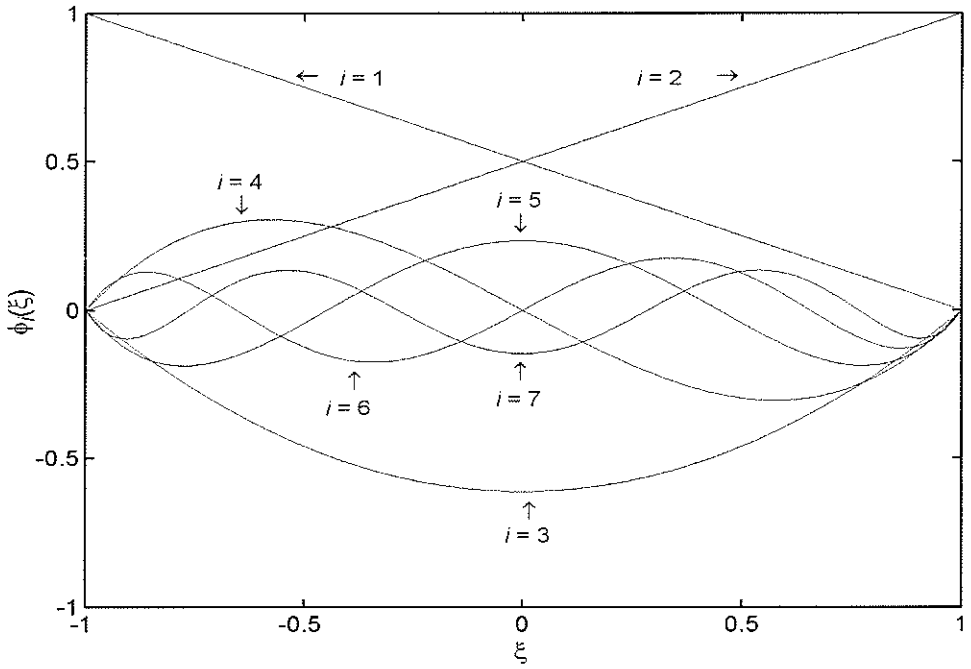

Fig. 2.2. Multi-*p* hierarchical basis functions.

§2.1.2. Multi-*p* Hierarchical Bases

The multi-*p* hierarchical basis functions are constructed with piecewise Legendre polynomials [49] as follows

$$\begin{cases} \phi_1(\xi) = (1-\xi)/2 \\ \phi_2(\xi) = (1+\xi)/2 \\ \phi_i(\xi) = \sqrt{(2i-3)/2}\int_{-1}^{\xi} P_{i-2}(t)dt, \qquad i = 3,\ 4,\ \cdots,\ p+1 \end{cases} \tag{2.4}$$

where $\phi_i, i \geq 3,$ is a polynomial of degree $i-1$ defined in terms of the Legendre polynomial P_{i-2}, the set of bases for $i \leq 7$ is shown in Fig. 2.2. They are hierarchical and generate a sequence of nested approximation spaces as in (2.1), where V_i is the span of the above polynomial basis functions with degree up to i, and the complementary subspace W_i in (2.2) is the span of polynomial basis functions of degree $i+1$.

The most important property of multi-*p* bases is that of being grid-independent, which is very useful in the numerical computation. Contrary to the classical hierarchical bases that employ a simple function on multilevel grids, the multi-*p* bases utilize multilevel basis functions with dynamic polynomial degrees on a fixed set of grids.

§2.1.3. Wavelet-Like Bases

Wavelet-like bases, also called multiwavelets [28], [29], are comprised of a finite set of scaling functions $\{\phi_i; i \in [1,k]\}$, where k is a positive integer. The scaling functions are constructed by orthogonalizing polynomial functions whose degree is less than k by the Gram-Schmidt process, and the corresponding multi-wavelets are

$$\psi_i(x) = \sqrt{2}\phi_i(2x-1), \quad i = 1, \cdots, k \tag{2.5}$$

whose translations and dilations in the form of

$$\psi_{j,m}^{n}(x) = 2^{m/2}\psi_j(2^m x - n), \quad j = 1, \cdots, k; m, n \in \mathbf{Z} \tag{2.6}$$

constitute a hierarchy of nested approximation spaces of L^2.

Wavelet-like bases are constructed to possess a combination of the properties of classical and multi-p hierarchical bases. They are also based on a set of multilevel grids with polynomials of different degree k. The wavelet-like bases are orthogonal and possess the most important properties of the wavelets, as indicated by their name, such as having k number of vanishing moments. The scaling functions $\{\phi_i; i \in [1, k]\}$ for $k = 4,\ 5$ are shown in Fig. 2.3.

§2.1.4. Wavelets

Differently from wavelet-like bases, wavelets form a hierarchy of nested approximation spaces of $\boldsymbol{L}^2$ and are constructed by translating and dilating a single scaling function and a single wavelet function. Their use is first introduced in [24], and has been extended to many areas. Typical examples of wavelets are shown in Appendix A.

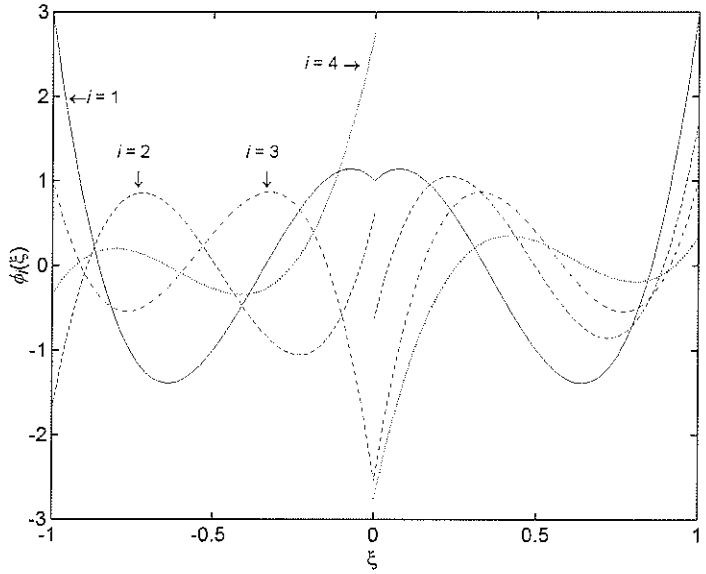

(a)

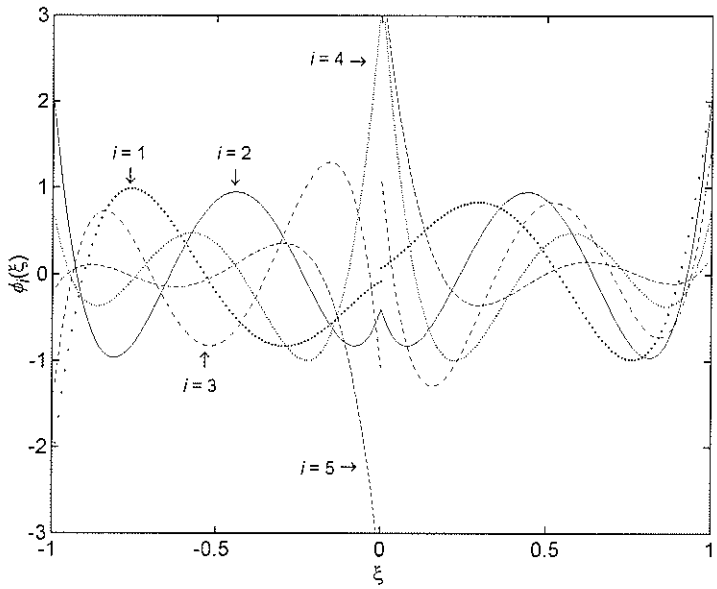

(b)

Fig. 2.3. Functions $\phi_1, \cdots, \phi_k$ for $k = 4$ in (a) and $k = 5$ in (b). ϕ_i is polynomial in the interval [0, 1] and is odd or even according to $\phi_i(\xi) = (-1)^{i+k-1}\phi_i(-\xi)$, $\xi = [-1, 0]$.

§2.2. Salient Features of Wavelets

Orthogonality

The wavelet transformation with orthogonal wavelets is a unitary transformation; the condition number of the transform matrices is equal to 1, which is an optimal case and is important in numerical computations. This means that an error in the original formulation will not grow, that the condition number will be preserved after the transformation, and that stable numerical computations are possible.

Compact support

The support width of wavelets is important in the implementation of the fast wavelet transform (FWT) algorithm [24]. If the scaling function and the wavelet function are compactly supported, their coefficient sequences are finite, so that the summations in the FWT are finite. Also the computational cost of FWT is proportional to the support width of wavelets selected. If they are not compactly supported, a fast decay is desired so that the filters can be truncated reasonably. It is reported, however, that this truncation causes a certain numerical error in computational electromagnetics [42].

Number of vanishing moments

Vanishing moments play an important role in data compression or large matrix compression [5]. Wavelets with a larger number of vanishing moments are desired to obtain a higher compression rate, which, however, increases the computational cost of FWT since wavelets with higher vanishing moments have a wider support width. The trade-off between

the number of vanishing moments and the FWT computational cost is one of criteria in the selection of wavelets when used for the fast solution of integral equations.

Analytical expression

An analytical expression for a scaling function or wavelet function does not always exist. In computational electromagnetics, it would be ideal to have closed form expressions such that the inner products associated with MoM can be exactly evaluated numerically. However, the change-of-basis scheme can be applied when no closed form expressions are available, the scheme utilizing only the coefficient sequences of wavelets.

There are other properties that are important in some specific applications. Rational filter coefficients are useful for computer implementation, since multiplication by a rational number on a computer corresponds to shifting bits, which is a very fast operation. Smoothness and symmetry of wavelets are useful in image compression, where the error after a threshold procedure can be easily detected visually.

As noted in [5] by Daubechies, it is impossible to construct wavelets that have all these properties, and there is a trade-off between them. The properties of some wavelets are compared in Table 2.1.

TABLE 2.1. COMPARISON OF VARIOUS FAMILIES OF WAVELETS.

Wavelet Family	Compact Support		Analytical Expression		Orthogonality	Symmetry
	Primary	Dual	Primary	Dual		
A	✓	✓	×	×	✓	×
B	✓	✓	✓	×	×	✓
C	✓	×	✓	×	☑	✓
D	×	×	×	×	✓	✓
E	×	×	×	×	✓	✓
F	✓	✓	×	×	✓	×

✓: Yes ×: No ☑: Semi

A: Daubechies' orthogonal wavelets

B: Biorthogonal spline wavelets

C: Semi-orthogonal wavelets

D: Meyer wavelets [4]

E: Battle-Lemarié wavelets [5]

F: Coiflets

§2.3. Use of Wavelets in the MoM

Consider a Fredholm integral equation of the first kind

$$f(s) = \mathcal{L}(u(s)) \tag{2.7}$$

with $\mathcal{L}$ being an integral operator defined as

$$\mathcal{L}(u(s)) = \int_C G(s,s')\,u(s')ds', \qquad s, s' \in C' \tag{2.8}$$

where u is the unknown function on C to be determined, with the kernel G and the function f being given. Equation (2.7) can be converted into a matrix equation by using MoM, and wavelets can be employed in the following ways.

§2.3.1. Direct Application

One may directly use wavelets as basis functions in MoM. The unknown function $u(s)$ can be approximated in terms of the scaling function ϕ and the wavelet ψ

$$u(s) = u^s(s) + u^d(s) \tag{2.9}$$

where

$$u^s(s) = P_{j_0}u(s) = \sum_{n=0}^{2^{j_0}-1} x_n^s \phi_{j_0,n}(s) \tag{2.10}$$

$$u^d(s) = Q_j u(s) = \sum_{m=j_0}^{j}\sum_{n=0}^{2^m-1} x_{m,n}^d \psi_{m,n}(s) \tag{2.11}$$

Here, j_0 is the coarsest resolution level, and x_n^s and $x_{m,n}^d$ are the expansion coefficients to be determined. P_{j_0} and Q_j are the projection operators onto spaces $\boldsymbol{V}_{j_0}$ and $\{\boldsymbol{W}_j;\ j \in [j_0, j]$, respectively.

Applying Galerkin's procedure to (2.7) leads to the following system of linear algebraic equations at the selected l-th resolution level

$$\boldsymbol{Z}\boldsymbol{I} = \boldsymbol{V} \tag{2.12}$$

with

$$\boldsymbol{Z} = \begin{bmatrix} \boldsymbol{B} & \boldsymbol{C} \\ \overline{\boldsymbol{C}} & \boldsymbol{D} \end{bmatrix}, \qquad \boldsymbol{V} = \begin{bmatrix} \boldsymbol{V}^s \\ \boldsymbol{V}^d \end{bmatrix}, \qquad \boldsymbol{I} = \begin{bmatrix} \boldsymbol{I}^s \\ \boldsymbol{I}^d \end{bmatrix} \tag{2.13}$$

whose elements are given by

$$\boldsymbol{I}^s = [x_0^s, x_1^s, \cdots, x_{2^{j_0}-1}^s]^T, \quad \boldsymbol{I}^d = [\boldsymbol{I}_{j_0}^d, \boldsymbol{I}_{j_0+1}^d \cdots, \boldsymbol{I}_{l-1}^d]^T \tag{2.14}$$

$$\begin{cases} V_n^s = \langle \phi_{j_0,n}, f \rangle \\ \boldsymbol{V}^d = [\boldsymbol{V}_{j_0}^d, \boldsymbol{V}_{j_0+1}^d \cdots, \boldsymbol{V}_{l-1}^d]^T \\ V_{m,n}^d = \langle \psi_{m,n}, f \rangle \end{cases} \tag{2.15}$$

$$\begin{cases} B_{n'n} = B^{j_0}_{n',n} = \langle \phi_{j_0,n'}, \mathcal{L}(\phi_{j_0,n}) \rangle \\ D_{m'n',mn} = D^{m}_{m'n',n} = \langle \psi_{m',n'}, \mathcal{L}(\psi_{m,n}) \rangle \\ C_{n',mn} = C^{m}_{n',n} = \langle \phi_{j_0,n'}, \mathcal{L}(\psi_{m,n}) \rangle \\ \overline{C}_{m'n',n} = \overline{C}^{m'}_{n',n} = \langle \psi_{m',n'}, \mathcal{L}(\phi_{j_0,n}) \rangle \end{cases} \tag{2.16}$$

where T indicates the transpose and $\boldsymbol{I}^d_m$ is a vector constructed from the coefficients of $m-$th scale in the form of $\boldsymbol{I}^d_m = [x^d_{m,0}, \cdots, x^d_{m,2^m-1}]^T$. The elements in (2.16) are ordered in consistency with (2.14) and the matrix operators are shown schematically in Fig. 2.4.

The direct application of wavelets in the MoM can be found typically in [33], [43], and [45] for orthogonal wavelets, and [44], [55] for semi-orthogonal wavelets, with the entries of resulting matrices evaluated numerically. Consequently, a large amount of computational work is required to perform numerical integrations.

§2.3.2. Change-of-Basis Scheme (CBS)

One may use wavelets in MoM through the change-of-basis scheme, which takes advantage of the FWT algorithm. The unknown function $u(s)$ is approximated in terms of the scaling functions ϕ

$$u(s) = P_l u(s) = \sum_n I_n \phi_{l,n}(s) \tag{2.17}$$

where P_l denotes the projection operator onto the space V_l, and (2.7) can be cast into the matrix equation (2.12) through the application of Galerkin's procedure, with

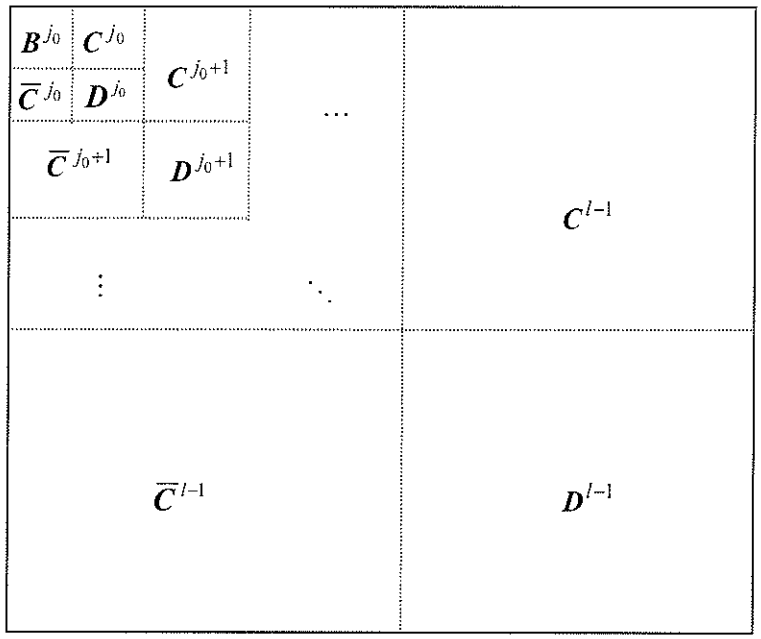

Fig. 2.4. Schematic description of the matrix operators $\boldsymbol{B}$, $\boldsymbol{C}$, $\overline{\boldsymbol{C}}$, and $\overline{\boldsymbol{D}}$ combined into the single matrix $\boldsymbol{Z}$.

$$Z_{mn} = \langle \phi_{l,m}, \mathcal{L}(\phi_{l,n}) \rangle, \qquad V_m = \langle \phi_{l,m}, f \rangle \tag{2.18}$$

Expressing the matrix equation in a recursive form as follows

$$\boldsymbol{Z}^j = \begin{bmatrix} \boldsymbol{Z}^{j-1} & \boldsymbol{C}^{j-1} \\ \boldsymbol{C}^{j-1} & \boldsymbol{D}^{j-1} \end{bmatrix}, \quad \boldsymbol{I}^j = \begin{bmatrix} \boldsymbol{I}^{j-1} \\ \boldsymbol{\Lambda}^{j-1} \end{bmatrix}, \quad \boldsymbol{V}^j = \begin{bmatrix} \boldsymbol{V}^{j-1} \\ \boldsymbol{\Gamma}^{j-1} \end{bmatrix} \tag{2.19}$$

the elements of the submatrices are

$$\begin{cases} Z_{kk'}^{j-1} = \sum_m \sum_n h_{2k-m} h_{2k'-n} Z_{mn}^j \\ C_{kk'}^{j-1} = \sum_m \sum_n h_{2k-m} g_{2k'-n} Z_{mn}^j \\ D_{kk'}^{j-1} = \sum_m \sum_n g_{2k-m} g_{2k'-n} Z_{mn}^j \\ \overline{C}_{kk'}^{j-1} = \sum_m \sum_n g_{2k-m} h_{2k'-n} Z_{mn}^j \end{cases} \tag{2.20}$$

$$I_{k'}^{j-1} = \sum_n h_{2k'-n} I_n^j, \quad \Lambda_{kk'}^{j-1} = \sum_n g_{2k'-n} I_n^j \tag{2.21}$$

$$V_{k'}^{j-1} = \sum_n h_{2k'-n} V_n^j, \quad \Gamma_{kk'}^{j-1} = \sum_n g_{2k'-n} V_n^j \tag{2.22}$$

By recursively computing (2.20)–(2.22), one can obtain the same matrix equation of the form (2.12) and (2.13) as that obtained by the direct application of wavelets. Note that the recursive algorithm is the FWT scheme that is applied to the MoM matrix equation and can be expressed in the matrix form as

$$\boldsymbol{WZW}^T(\boldsymbol{W}^T)^{-1}\boldsymbol{I} = \boldsymbol{WV} \tag{2.23}$$

which leads to a new equation

$$\boldsymbol{Z}'\boldsymbol{I}' = \boldsymbol{V}' \tag{2.24}$$

with

$$\boldsymbol{Z}' = \boldsymbol{WZW}^T, \quad \boldsymbol{I} = \boldsymbol{W}^T\boldsymbol{I}', \quad \boldsymbol{V} = \boldsymbol{WV} \tag{2.25}$$

where $\boldsymbol{W}$ denotes a transform matrix performing the FWT with relevant wavelets selected. For wavelets whose analytical expressions are not available, the scaling function ϕ at the highest level in (2.18) is usually approximated in practice by some local basis function such as rectangular or triangular basis function. The high computational cost in the direct application of wavelets is substantially reduced in this scheme [63], [70], [71].

§2.3.3. Matrix Transform Approach (MTA)

This idea of the matrix transform approach is borrowed from that of the change-of-basis scheme described above, where a system of linear equations of the form (2.12) is first obtained by a conventional MoM with some local basis functions such as rectangular or triangular pulse functions, and then a matrix transformation as described in (2.23) is applied, with the transform matrices constructed by using wavelets. Here, the wavelet transform matrices $\boldsymbol{W}$ simply act as a sparse preconditioner, and thus is problem independent. The transformed matrix $\boldsymbol{Z}'$ is highly sparse after thresholding due to the wavelet property of vanishing moments. The differences between the CBS and the MTA will be discussed in detail in Chapter 4.

§2.4. Summary

This Chapter has described some literature covering hierarchical bases and their applications in computational electromagnetics. The salient features of various wavelets are further studied and compared in this Chapter, and it was found that wavelets are optimal hierarchical basis functions.

Wavelets can be applied for the fast solution of electromagnetic integral equations in a number of ways. The direct application of wavelets as basis functions in the MoM results in intensive computational efforts to evaluate the entries of moment-method matrices, while it is substantially reduced in CBS or MTA, which fully exploit the advantage of the FWT algorithm. The main difference between the CBS and the MTA is the construction details of a wavelet transform matrix. The MTA simply uses one-dimensional wavelets and the wavelet transform matrix acts as a sparse preconditioner; multidimensional wavelets, however, are required in the case of the CBS for the solution of multidimensional integral equations.

Chapter 3

SELECTION OF WAVELETS USED FOR THE SOLUTION OF INTEGRAL EQUATIONS

§3.1. Introduction

The selection of the number of vanishing moments in a family of wavelets has been investigated in [45] for Daubechies' orthogonal wavelets (DOW), and in [63] for semi-orthogonal wavelets (SOW). It has been pointed out that 8 vanishing moments are optimal when the number of unknowns is less than 5000.

Two categories of wavelets, orthogonal and semi-orthogonal, are mainly used in computational electromagnetics. It has been reported that the use of SOW yields more highly sparse matrices and better solution accuracy when a direct solver is adopted than the use of orthogonal wavelets [63], [64]. However, the efficiency of the iterative solution methods for the sparse matrix equations obtained by using the SOW has not been investigated.

The focus of this Chapter is to compare systematically the SOW and the DOW when used for the solution of integral equations. Firstly, the effect of thresholding on the matrix sparsity and also on the solution accuracy, as well as the relationship between accuracy and matrix sparsity, are examined. Then the condition number of matrices involved is examined. Since the SOW transform yields a matrix with a larger condition number than that corresponding to the DOW transform, it is expected that the convergence rate for an iterative method is much better in the latter case. Numerical simulations are conducted for the

transverse magnetic (TM) and transverse electric (TE) scattering by conducting cylinders of an arbitrary size with the CG iterative method.

§3.2. Problem Formulation

Consider an infinitely long conducting cylinder excited by a TM or TE (to the $z-$axis) electromagnetic plane wave in free space. The induced current density $J(\boldsymbol{r})$ on the surface is related to the incident field $F(\boldsymbol{r})$ through the following integral equation

$$\int_C G(\boldsymbol{r},\boldsymbol{r}')J(\boldsymbol{r}')dl' = F(\boldsymbol{r}) \tag{3.1}$$

with C being the cylinder cross-section contour and G the Green's function.

In the case of TM incident wave, we have

$$\begin{cases} F(\boldsymbol{r}) = E_z^{inc}(\boldsymbol{r}) \\ G(\boldsymbol{r},\boldsymbol{r}') = \dfrac{k\eta}{4} H_0^{(2)}(k\,|\,\boldsymbol{r}-\boldsymbol{r}'\,|) \end{cases} \tag{3.2}$$

where E_z^{inc} is the incident electric field intensity, $H_0^{(2)}$ is the Hankel function of the second kind and zero order, and k and η are the wave number and the intrinsic impedance of free space, respectively.

In the case of TE incident wave, we have

$$\begin{cases} F(\boldsymbol{r}) = H_z^{inc}(\boldsymbol{r}) \\ G(\boldsymbol{r},\boldsymbol{r}') = \delta(\boldsymbol{r}-\boldsymbol{r}') + \dfrac{jk}{4} H_1^{(2)}(k\,|\,\boldsymbol{r}-\boldsymbol{r}'\,|)\cos[\boldsymbol{n}(\boldsymbol{r}'),\boldsymbol{r}-\boldsymbol{r}'] \end{cases} \tag{3.3}$$

with H_z^{inc} being the incident field intensity, $H_1^{(2)}$ the Hankel function of the second kind and first order, and $\boldsymbol{n}$ the unit normal vector directed out of the cylinder.

§3.3. Effect of the Condition Number

The condition number of a matrix $\boldsymbol{A}$ is defined as [2]

$$\gamma(\boldsymbol{A}) = \| \boldsymbol{A}^{-1} \| \cdot \| \boldsymbol{A} \| \tag{3.4}$$

where $\| \cdot \|$ denotes the Euclidean matrix norm, and can be computed through the singular value decomposition of the matrix $\boldsymbol{A}$ [2].

In the case of DOW, the wavelet transform matrix is orthogonal, that is, $\boldsymbol{W}^{-1} = \boldsymbol{W}^T$, and the condition number $\gamma(\boldsymbol{W}) = 1$. For SOW with m vanishing moments, the condition number of the transform matrix $\boldsymbol{W}$ of order $N \times N$ has been computed for different values of N, namely N = 128, 256, 512, and 1024. Numerical experiments show that the condition number is independent of N, but it depends on the number m, as shown in TABLE 3.1.

Using the properties of the Euclidean matrix norm, the following estimate exists

$$\gamma(\boldsymbol{Z}') = \gamma(\boldsymbol{W}\boldsymbol{Z}\boldsymbol{W}^T) \le \gamma^2(\boldsymbol{W})\gamma(\boldsymbol{Z}) \tag{3.5}$$

which means that the upper bound of the condition number of $\boldsymbol{Z}'$ is about $\gamma^2(\boldsymbol{W})$ times greater than $\gamma(\boldsymbol{Z})$ for SOW transformation.

The influence of the condition number of a system matrix on the convergence rate of the CG method was analyzed in [12] for symmetric and positive definite matrices. It was observed that the number of iterations required is approximately $\kappa = p\gamma^{1/2}$ to ensure a solution accuracy of p decimal places. This effect is also studied in [20] for MoM matrices arising from electromagnetic integral equations. Since the CG solver requires the system matrix to be positive definite, the original MoM matrix equations of the form (2.12) is converted into the normal equation $\boldsymbol{Z}^H \boldsymbol{Z}\boldsymbol{I} = \boldsymbol{Z}^H \boldsymbol{V}$, where H denotes the conjugate transpose. In this case, $\kappa = p\gamma(\boldsymbol{Z})$. Therefore, if the same accuracy is required, the number of iterations for solving the transformed matrix equation will be increased approximately by $\gamma^2(\boldsymbol{W})$ times with respect to that for solving the original MoM matrix equation.

TABLE 3.1. CONDITION NUMBER $\gamma(\boldsymbol{W})$ FOR SOW WITH m VANISHING MOMENTS.

m	1	2	3	4	5	6	7	8
$\gamma(\boldsymbol{W})$	1.0	2.60	5.13	9.97	19.32	37.43	72.53	140.53

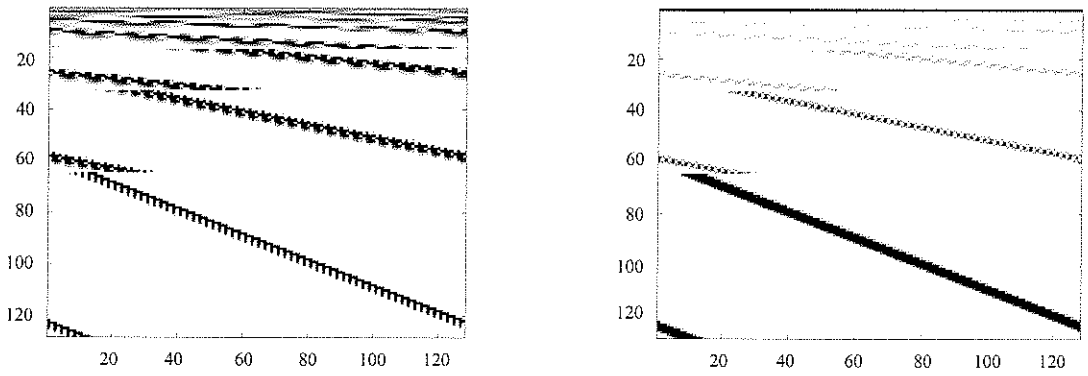

(a) (b)

Fig. 3.1. Gray-scaled images of the wavelet transform matrices of order 128 × 128 with 8 vanishing moments: (a) DOW, (b) SOW.

§3.4. Numerical Experiments

To measure the solution accuracy, the residual error for the equation (2.12) is defined as

$$\varepsilon(\boldsymbol{Z}) = \| \boldsymbol{Z}\boldsymbol{I}^{calc} - \boldsymbol{V} \| / \| \boldsymbol{V} \| \times 100(\%) \tag{3.6}$$

where $\boldsymbol{I}^{calc}$ is the computed solution. The sparsity of a matrix of order $N \times N$ is defined as

$$S = (1 - M_\delta / N^2) \times 100(\%) \tag{3.7}$$

where M_δ is the total number of nonzero elements of the matrix after thresholding with the threshold value δ, which is one of the input parameters of the computer program. Equation (3.1) is converted into the matrix equation of the form (2.12) by the point-matching MoM with fixed ceil size selected as one tenth of the wavelength of the incident wave in free space.

SOW and DOW with 8 vanishing moments have been employed to perform the wavelet transforms in (3.5) as in [45] and [63].

§3.4.1. TM Scattering

Sparsity and Solution Accuracy

Numerical computations are first conducted to compare the DOW and SOW in terms of matrix sparsity and the solution accuracy by the standard LU solver. The surface current distributions for a perfectly conducting cylinder of an electric radius $ka = 12.8$, computed when the sparsity $S = 83.3\%$ for both the DOW and the SOW, are shown in Fig. 3.2, where the analytical solution is given as reference. The matrix sparsity S and the residual error ε as functions of the threshold value δ are plotted in Fig. 3.3. The structures of the sparse matrices when a residual error of $\varepsilon(\boldsymbol{Z}) = 0.48\%$, for example, is imposed for the DOW and SOW are given in Fig. 3.4. Several conclusions can be drawn from the above experiments. Firstly, the use of SOW produces a matrix with very small values of some entries such that the threshold value is much smaller than that of the DOW. Secondly, in comparison with the DOW, the use of the SOW gives a better performance in terms of the residual error when the matrix sparsity is less than a certain value, namely 84.03% in this example, as shown in Fig. 3.5. Thirdly, the residual error increases irregularly with the increase of the matrix sparsity when using SOW, which indicates a worse condition number of the transform matrices.

Condition Number

We now present experimental results when the CG solver is used for the solution of the respective matrix equations. The condition number and the residual error after κ iterations

are listed in Table 3.3. For DOW, $\gamma(\boldsymbol{Z}) \approx \gamma(\boldsymbol{Z}')$ and the number of iterations to achieve a solution with the residual error $\varepsilon(\boldsymbol{Z}) \leq 10^{-3}\%$ is $\kappa(\boldsymbol{Z}) = \kappa(\boldsymbol{Z}')$. For SOW, however, $\gamma(\boldsymbol{Z}')$ is approximately $(10^2 \sim 10^4)\gamma(\boldsymbol{Z})$ as expected, and the residual error $\varepsilon(\boldsymbol{Z})$ cannot be decreased below 2% even after N iterations for all values of N considered. Practically, one solves the sparse matrix equation obtained after thresholding the entries of the transformed matrices. Table 3.2 shows the number of iterations κ versus the matrix sparsity in the DOW case when $N = 128$ and with the termination criterion chosen to be $\varepsilon(\boldsymbol{Z}) \leq 10^{-3}\%$. It can be seen that the number of iterations increases with the increase of the sparsity. The convergence rate of the CG solver for $N = 128$, when using DOW and SOW, is shown in Fig. 3.6. Clearly, a solution with an error $\varepsilon(\boldsymbol{Z}) \leq 2\%$ cannot be achieved with the CG solver when the SOW matrix transform is used in all cases considered.

§3.4.2. TE Scattering

Sparsity and Solution Accuracy

The same experimental procedure as in the TM scattering case is followed to compare the DOW and the SOW. Now the computed surface current distributions are compared to the analytical result for a circular cylinder with the electrical radius $ka = 25.6$ in Fig. 3.7, and the matrix sparsity and the residual error as functions of the threshold value are plotted in Fig. 3.8. It is again observed that the use of the SOW yields a sparse matrix with a small threshold value. The residual error versus the matrix sparsity is shown in Fig. 3.9. The use of SOW does not show any advantage in terms of the solution accuracy when $S > 85.7\%$.

Condition Number

The condition numbers after κ iterations of the CG solver are listed in Table 3.2. For the SOW, It is observed that $\gamma(\boldsymbol{Z}') \approx (10^3 \sim 10^4)\gamma(\boldsymbol{Z})$ and the residual error is $\varepsilon(\boldsymbol{Z}) > 3\%$ even after N iterations for all considered values of N. When $N = 256$, the convergence rates of the CG solver are shown in Fig. 3.10 for both the DOW and the SOW, where the convergence rate with the matrix sparsity $S = 88.5\%$ is also plotted. Obviously, a solution with $\varepsilon \leq 1\%$ cannot be achieved within N iterations in this example, too.

§3.5. Conclusions

In this chapter, the selection of wavelets used for the integral equation approach is studied systematically by examining the efficiency of the two categories of wavelets, namely the DOW and the SOW. The Euclidean norm of a matrix is employed and the singular value decomposition method is utilized to evaluate the matrix norm as well as the matrix condition number. The condition number of a MoM matrix is preserved after the DOW transformation, but is increased significantly after the SOW transformation. Numerical results for the electromagnetic scattering by conducting cylinders show that the condition number of a MoM matrix using the SOW with 8 vanishing moments is enlarged approximately $10^2 \sim 10^4$ times, in agreement with the theoretical predictions. As a consequence, the convergence rate of the CG solver is slow and a solution with the residual error less than 1% cannot be achieved for the examples considered. The results presented indicate that the DOW are optimal wavelets for the solution of integral equations when an iterative method of solution is employed.

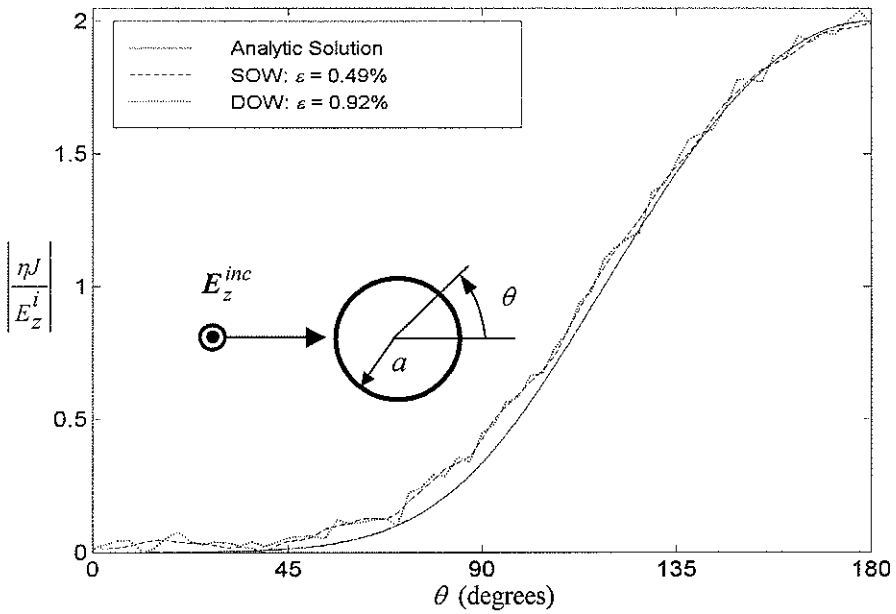

Fig. 3.2. Surface current distribution on a circular conducting cylinder with $ka = 12.8$ and the matrix sparsity $S = 83.3\%$.

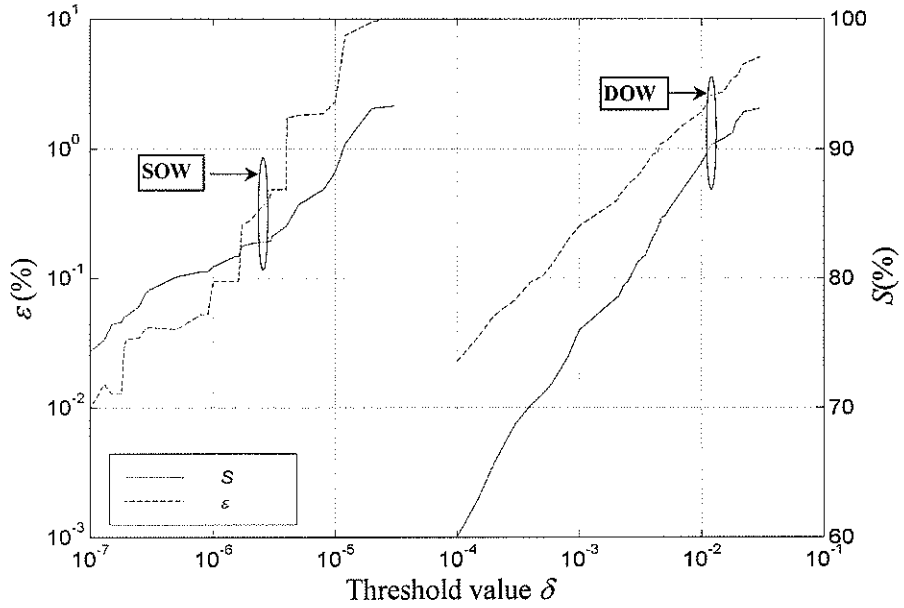

Fig. 3.3. Relative error ε and matrix sparsity S versus threshold value δ for the cylinder in Fig. 3.2.

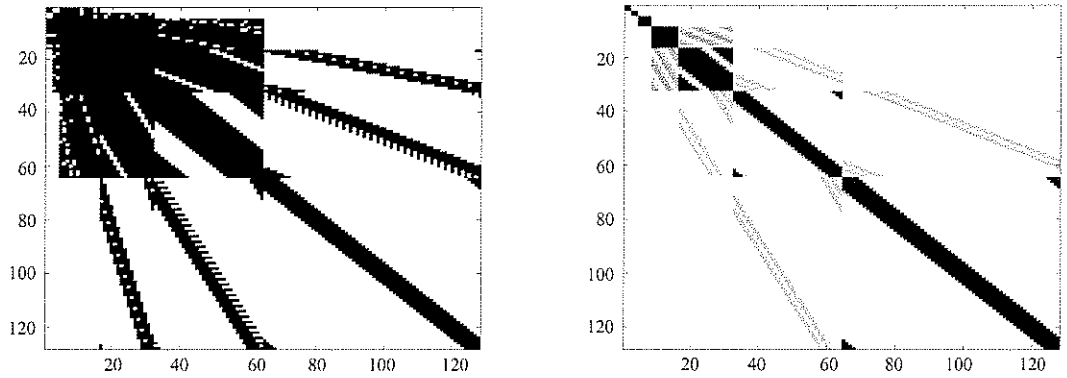

Fig. 3.4. Structures of sparse matrices after thresholding when the residual error $\varepsilon(\boldsymbol{Z}) = 0.48\%$: (a) DOW, $S = 79.47\%$; (b) SOW, $S = 82.98\%$.

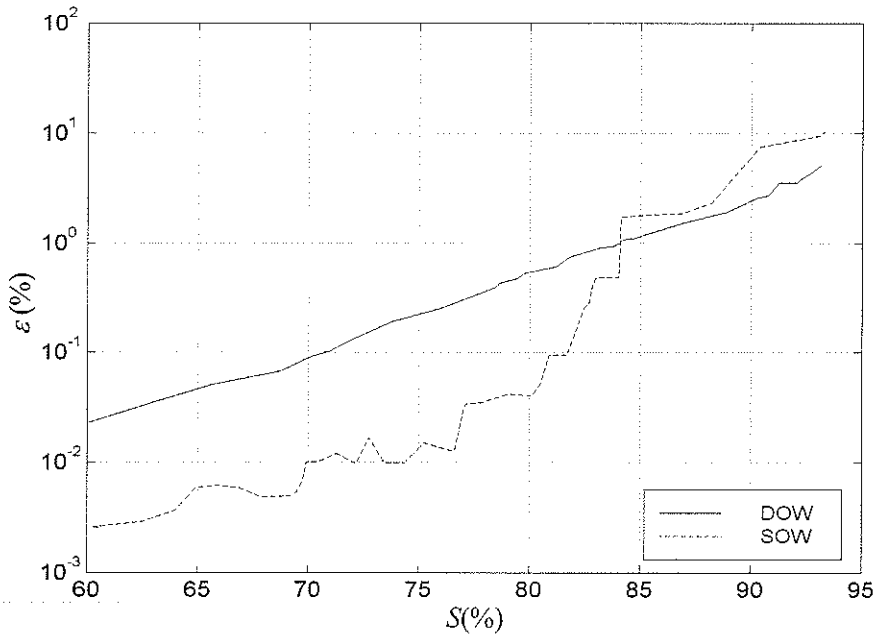

Fig. 3.5. Residual error ε versus matrix sparsity S.

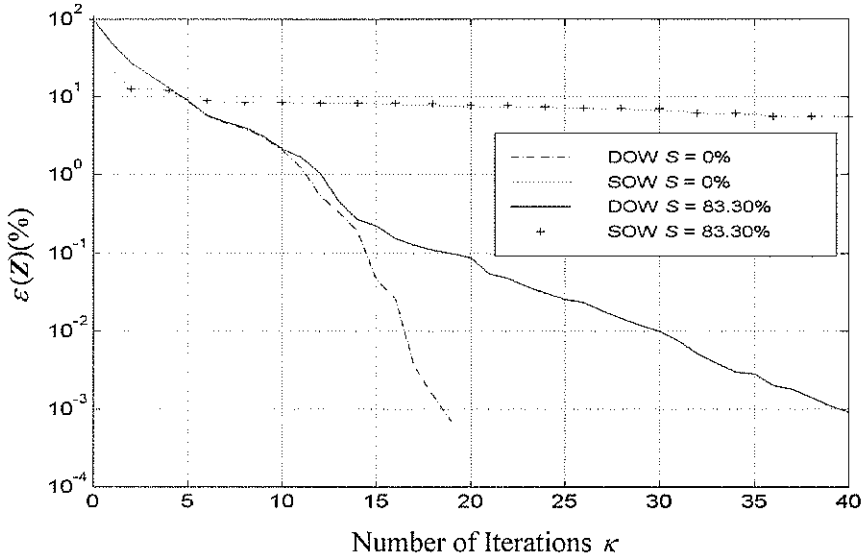

Fig. 3.6. Convergence rate of the CG solver when $N = 128$.

TABLE 3.2. NUMBER OF ITERATIONS κ VERSUS MATRIX SPARSITY S WHEN $N = 128$ AND THE TERMINATION CRITERION IS SET TO $\varepsilon(\boldsymbol{Z}) \le 10^{-3}$ % IN THE DOW CASE.

S(%)	60.06	70.97	75.98	78.44	83.30	84.77
κ	25	33	35	37	40	41

TABLE 3.3. CONDITION NUMBER γ AND RELATIVE ERROR $\varepsilon(\%)$ AFTER κ ITERATIONS FOR DIFFERENT MATRIX SIZES WITHOUT THRESHOLDING (TM CASE).

N	MoM			DOW			SOW		
	$\gamma(\boldsymbol{Z})$	κ	$\varepsilon(\boldsymbol{Z})$	$\gamma(\boldsymbol{Z}')$	κ	$\varepsilon(\boldsymbol{Z}')$	$\gamma(\boldsymbol{Z}')$	κ	$\varepsilon(\boldsymbol{Z}')$
128	13.83	19	6.68×10^{-4}	13.83	19	6.68×10^{-4}	3.17×10^{4}	129	2.27
256	29.50	50	9.19×10^{-4}	29.50	50	8.63×10^{-4}	1.14×10^{5}	257	2.79
512	103.97	101	6.90×10^{-4}	103.94	102	9.04×10^{-4}	1.40×10^{5}	513	3.12
1024	247.09	229	9.59×10^{-4}	246.97	234	8.51×10^{-4}	6.14×10^{4}	1025	4.17

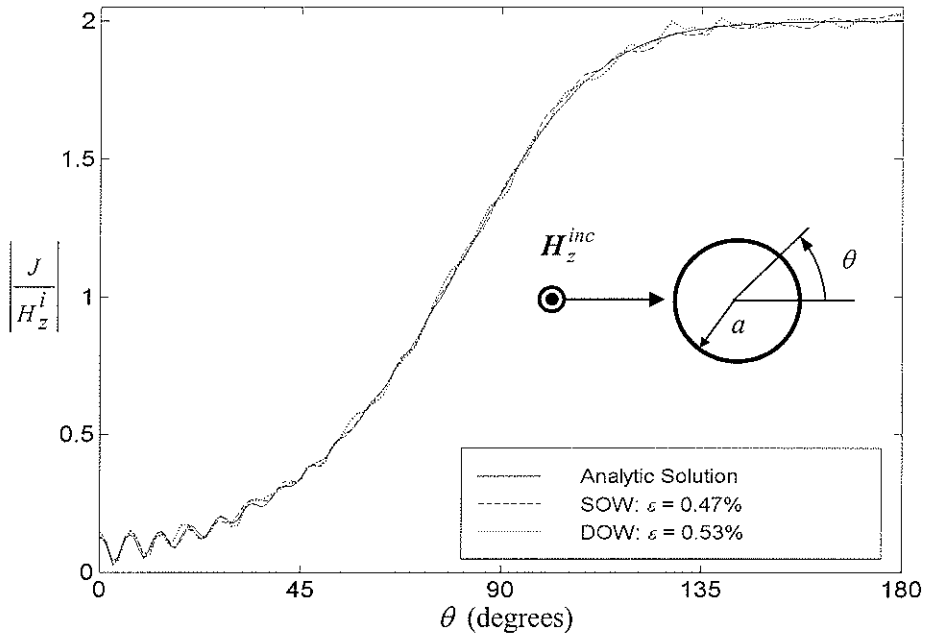

Fig. 3.7. Surface current distribution for a circular conducting cylinder with $ka = 25.6$ and the matrix sparsity $S = 88.5\%$.

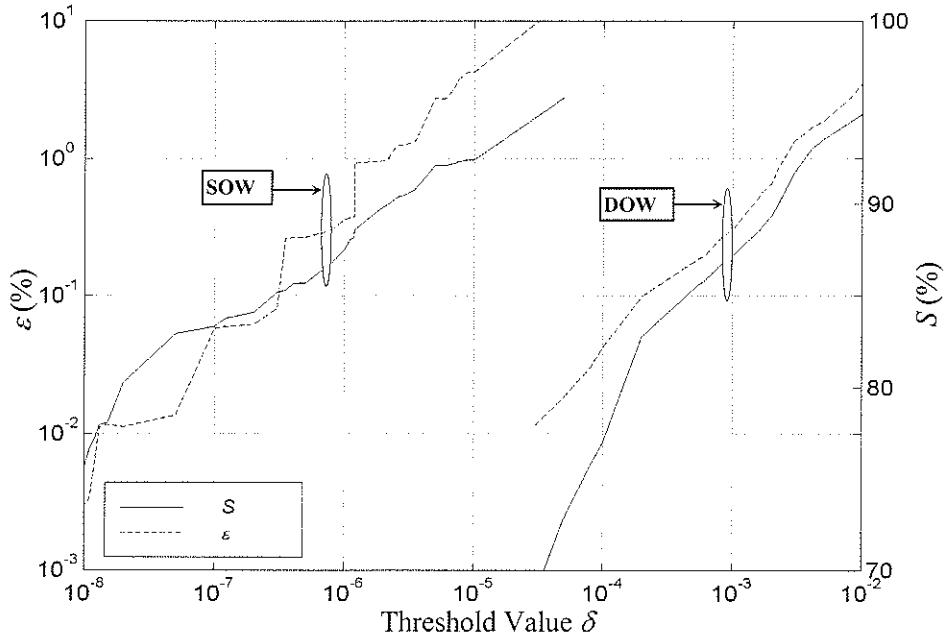

Fig. 3.8. Relative error ε and matrix sparsity S versus threshold value δ for the scatterer in Fig. 3.7.

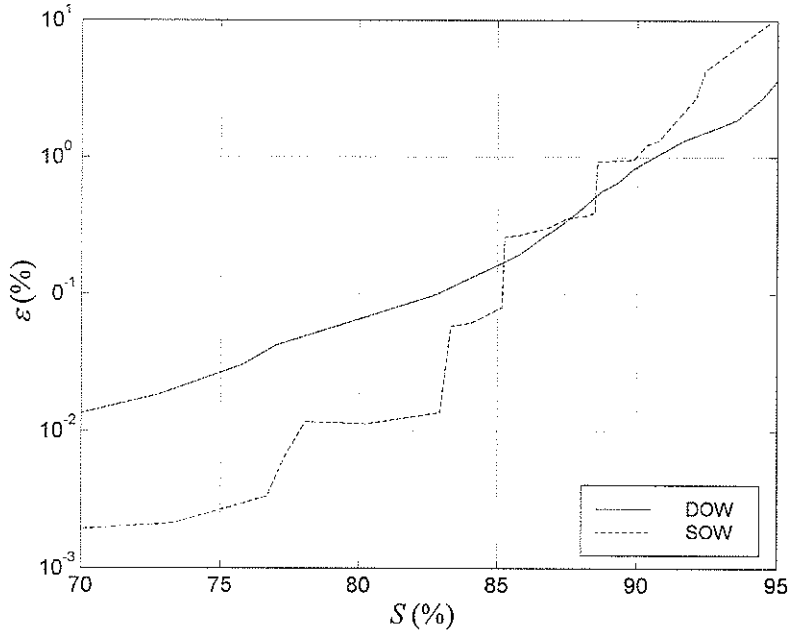

Fig. 3.9. Relative error ε versus matrix sparsity S.

TABLE 3.4. CONDITION NUMBER γ AND RELATIVE ERROR $\varepsilon(\%)$ AFTER κ ITERATIONS FOR DIFFERENT MATRIX SIZES WITHOUT THRESHOLDING (TE CASE).

N	MoM			DOW			SOW		
	$\gamma(\boldsymbol{Z})$	κ	$\varepsilon(\boldsymbol{Z})$	$\gamma(\boldsymbol{Z}')$	κ	$\varepsilon(\boldsymbol{Z}')$	$\gamma(\boldsymbol{Z}')$	κ	$\varepsilon(\boldsymbol{Z}')$
128	4.71	14	2.79×10^{-4}	4.72	14	2.79×10^{-4}	3.36×10^{4}	129	3.07
256	12.43	36	6.21×10^{-4}	12.43	36	7.06×10^{-4}	1.17×10^{5}	257	4.44
512	80.02	55	9.38×10^{-4}	80.04	55	9.35×10^{-4}	1.40×10^{5}	513	5.68
1024	1.86×10^{3}	114	9.06×10^{-4}	1.87×10^{3}	115	9.52×10^{-4}	8.03×10^{5}	1025	8.40

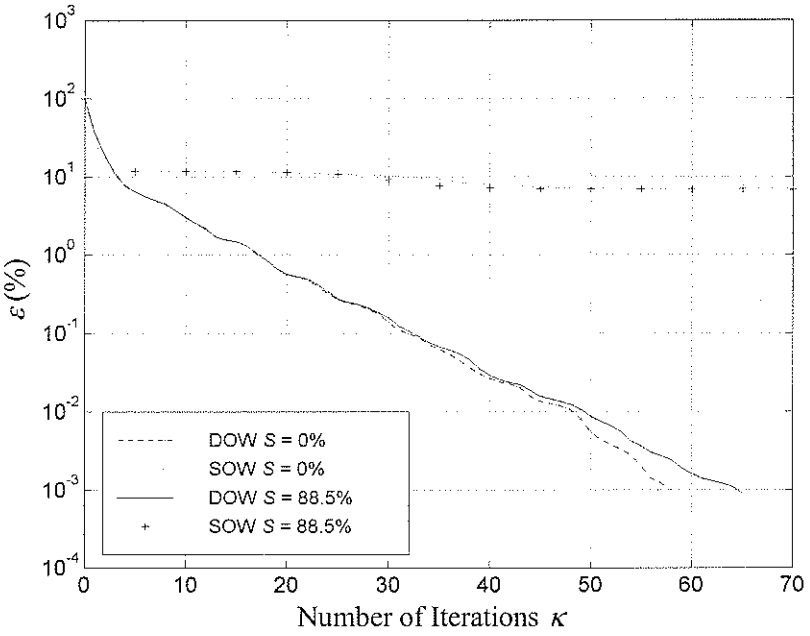

Fig. 3.10. Convergence rate of the CG solver for $N = 256$.

Chapter 4

SCATTERING BY DIELECTRIC BODIES

§4.1. Introduction

For orthogonal wavelets, both the MTA and the CBS described in Chapter 2 can be used for a fast solution of integral equations. The two methods are differentiated by the construction details of the wavelet transform matrix $\boldsymbol{W}$. In the case of the MTA, $\boldsymbol{W}$ is constructed by simply using one-dimensional wavelets, while in the case of the CBS it is constructed with multi-dimensional wavelets, which are tensor products of one-dimensional wavelets. It is noted that for problems formulated based on one-dimensional Fredholm integral equations, as those studied in Chapter 3, the CBS and the MTA are identical, since the unknowns associated with the integral equations are single vectors, and the one-dimensional FWT is required in both methods.

In this Chapter, the use of wavelets in the MoM for a fast analysis of scattering by two-dimensional dielectric bodies is studied. The mathematical formulation employs coupled surface integral equations, and the unknowns to be determined are two independent vectors. The main focus is to compare the performances of the CBS and the MTA, with numerical experiments conducted for various dielectric bodies.

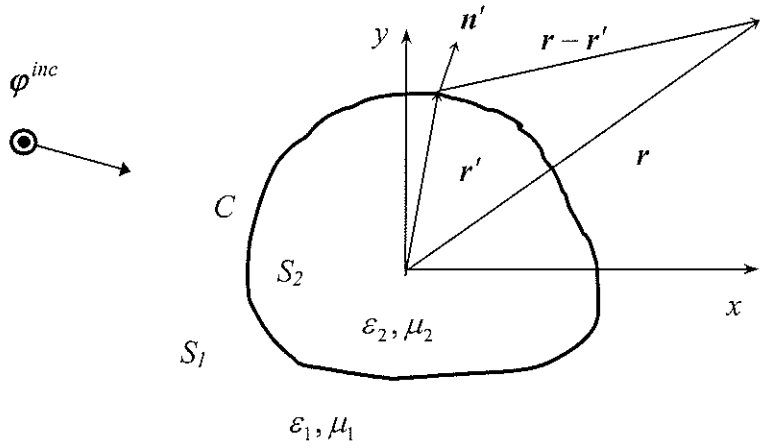

Fig. 4.1. Two-dimensional dielectric obstacle immersed in an incident field φ^{inc}.

§4.2. Problem Formulation

Consider the scattering problem by a dielectric obstacle in a 2-dimensional space as shown in Fig. 4.1, illuminated by an incident electromagnetic plane wave. The illuminating field $\varphi^{inc} = z\varphi^{inc}$ has only a $z-$component and is independent of the $z-$axis. The governing equation for the fields is the scalar Helmholtz equation,

$$\begin{cases} (\nabla^2 + k_1^2)\varphi_1^s(\boldsymbol{r}) = 0, & r \in S_1 \\ (\nabla^2 + k_2^2)\varphi_2(\boldsymbol{r}) = 0, & r \in S_2 \end{cases} \tag{4.1}$$

where $k_i = \omega\sqrt{\varepsilon_i \mu_i}$ is the medium wave number, ε_i and μ_i being the permittivity and permeability of the respective region S_i, $i = 1, 2$. The total field φ_1 in S_1 is

$$\varphi_1 = \varphi^{inc} + \varphi_1^s \tag{4.2}$$

We define Green's functions in the respective regions to satisfy the following equations in two dimensions

$$(\nabla^2 + k_i^2) g_i(\boldsymbol{r}) = -\delta(\boldsymbol{r} - \boldsymbol{r}'), \qquad i = 1, 2 \tag{4.3}$$

and the radiation condition at infinity

$$g_i(\boldsymbol{r}, \boldsymbol{r}') = \frac{1}{4j} H_0^{(2)}(k_i \mid \boldsymbol{r} - \boldsymbol{r}' \mid) \tag{4.4}$$

where $\boldsymbol{r}, \boldsymbol{r}'$ are position vectors and $H_0^{(2)}$ the Hankel function of the second kind and zero order.

From (4.1)–(4.3) and with some mathematical manipulations, we have

$$\begin{cases} \int_S [g_1(\boldsymbol{r}, \boldsymbol{r}') \nabla^2 \varphi_1(\boldsymbol{r}) - \varphi_1(\boldsymbol{r}) \nabla^2 g_1(\boldsymbol{r}, \boldsymbol{r}')] d\boldsymbol{s} = \varphi^{inc}(\boldsymbol{r}') - \varphi_1(\boldsymbol{r}'), & \boldsymbol{r}' \in S_1 \\ \int_S [g_2(\boldsymbol{r}, \boldsymbol{r}') \nabla^2 \varphi_2(\boldsymbol{r}) - \varphi_2(\boldsymbol{r}) \nabla^2 g_2(\boldsymbol{r}, \boldsymbol{r}')] d\boldsymbol{s} = \varphi_2(\boldsymbol{r}'), & \boldsymbol{r}' \in S_2 \end{cases} \tag{4.5}$$

By applying the Green's second identity [1], the integrals on the left-hand side of (4.5) become contour integrals over the cross-sectional contour C bounding the dielectric region S_2. Consequently,

$$\begin{cases} \int_C g_1(\boldsymbol{r},\boldsymbol{r}')\boldsymbol{n}'\cdot\nabla'\varphi_1(\boldsymbol{r}')dl' - \int_C \varphi_1(\boldsymbol{r}')\boldsymbol{n}'\cdot\nabla' g_1(\boldsymbol{r},\boldsymbol{r}')dl' = \varphi^{inc} - \varphi_1(\boldsymbol{r}), & \boldsymbol{r}\in S_1 \\ \int_C g_2(\boldsymbol{r},\boldsymbol{r}')\boldsymbol{n}'\cdot\nabla'\varphi_2(\boldsymbol{r}')dl' - \int_C \varphi_2(\boldsymbol{r}')\boldsymbol{n}'\cdot\nabla' g_2(\boldsymbol{r},\boldsymbol{r}')dl' = \varphi_2(\boldsymbol{r}), & \boldsymbol{r}\in S_2 \end{cases} \tag{4.6}$$

φ_i and $\boldsymbol{n}'\cdot\nabla'\varphi_i$ act as surface sources, and satisfy the boundary conditions of the form

$$\begin{cases} \varphi_1(\boldsymbol{r}) = \varphi_2(\boldsymbol{r}) \\ p_1\boldsymbol{n}\cdot\nabla\varphi_1(\boldsymbol{r}) = p_2\boldsymbol{n}\cdot\nabla\varphi_2(\boldsymbol{r}), & \boldsymbol{r}\in C \end{cases} \tag{4.7}$$

with $p_i = \mu_i, i = 1,2$ when φ is an electric filed and $p_i = \varepsilon_i$ when φ is a magnetic field. With implying (4.7), (4.6) can be written symbolically as

$$\begin{cases} \mathcal{L}_{11}(\boldsymbol{n}'\cdot\nabla'\varphi(\boldsymbol{r}')) + \mathcal{L}_{12}(\varphi(\boldsymbol{r}')) = \varphi^{inc}(\boldsymbol{r}) \\ \mathcal{L}_{21}(\boldsymbol{n}'\cdot\nabla'\varphi(\boldsymbol{r}')) + \mathcal{L}_{22}(\varphi(\boldsymbol{r}')) = 0, & \boldsymbol{r}\in C \end{cases} \tag{4.8}$$

where the integral operators are

$$\begin{cases} \mathcal{L}_{11}(\boldsymbol{n}'\cdot\nabla'\varphi(\boldsymbol{r}')) = \int_C g_1(\boldsymbol{r},\boldsymbol{r}')\boldsymbol{n}'\cdot\nabla'\varphi(\boldsymbol{r}')dl' \\ \mathcal{L}_{12}(\varphi(\boldsymbol{r}')) = -\int_C \varphi(\boldsymbol{r}')\boldsymbol{n}'\cdot\nabla' g_1(\boldsymbol{r},\boldsymbol{r}')dl' + \varphi(\boldsymbol{r}) \\ \mathcal{L}_{21}(\boldsymbol{n}'\cdot\nabla'\varphi(\boldsymbol{r}')) = \dfrac{p_1}{p_2}\int_C g_2(\boldsymbol{r},\boldsymbol{r}')\boldsymbol{n}'\cdot\nabla'\varphi(\boldsymbol{r}')dl' \\ \mathcal{L}_{22}(\varphi(\boldsymbol{r}')) = -\int_C \varphi(\boldsymbol{r}')\boldsymbol{n}'\cdot\nabla' g_2(\boldsymbol{r},\boldsymbol{r}')dl' - \varphi(\boldsymbol{r}) \end{cases} \tag{4.9}$$

Thus, the integral equations (4.8) contain two independent unknowns φ and $\boldsymbol{n}' \cdot \nabla' \varphi$ on C. Consequently, (4.8) can be treated as linear operator equations and solved with the MoM.

§4.3. Numerical Method

To solve (4.8) with the MoM, we let

$$\begin{cases} \boldsymbol{n}' \cdot \nabla' \varphi(\boldsymbol{r}') = \sum_{n=1}^{N} a_n f_{1,n}(\boldsymbol{r}') \\ \varphi(\boldsymbol{r}') = \sum_{n=1}^{N} b_n f_{2,n}(\boldsymbol{r}') \end{cases} \tag{4.10}$$

where $f_{1,n}(\boldsymbol{r}')$ and $f_{2,n}(\boldsymbol{r}')$ are the selected basis functions. Then, (4.8) becomes

$$\begin{cases} \sum_{n=1}^{N} a_n \mathcal{L}_{11}(f_{1,n}(\boldsymbol{r}')) + \sum_{n=1}^{N} b_n \mathcal{L}_{12}(f_{2,n}(\boldsymbol{r}')) = 0 \\ \sum_{n=1}^{N} a_n \mathcal{L}_{21}(f_{1,n}(\boldsymbol{r}')) + \sum_{n=1}^{N} b_n \mathcal{L}_{22}(f_{2,n}(\boldsymbol{r}')) = \varphi^{inc}(\boldsymbol{r}) \end{cases} \tag{4.11}$$

Applying the weighted residual procedure with selected weighting functions $w_{1,m}(\boldsymbol{r}')$ and $w_{2,m}(\boldsymbol{r}')$ for $m = 1, N$ leads to a system of $2N$ linear algebraic equations in the form of

$$\begin{cases} \sum_{n=1}^{N} a_n \langle w_{1,m},\ \mathcal{L}_{11}(f_{1,n}(\boldsymbol{r}')) \rangle + \sum_{n=1}^{N} b_n \langle w_{1,m},\ \mathcal{L}_{12}(f_{2,n}(\boldsymbol{r}')) \rangle = 0 \\ \sum_{n=1}^{N} a_n \langle w_{2,m},\ \mathcal{L}_{21}(f_{1,n}(\boldsymbol{r}')) \rangle + \sum_{n=1}^{N} b_n \langle w_{2,m},\ \mathcal{L}_{22}(f_{2,n}(\boldsymbol{r}')) \rangle = \langle w_{2,m}, \varphi^{inc}(\boldsymbol{r}) \rangle \end{cases} \tag{4.12}$$

which can be written in the form of a matrix equation as

$$\begin{bmatrix} \boldsymbol{Z}_{11} & \boldsymbol{Z}_{12} \\ \boldsymbol{Z}_{21} & \boldsymbol{Z}_{22} \end{bmatrix} \begin{bmatrix} \boldsymbol{I}_1 \\ \boldsymbol{I}_2 \end{bmatrix} = \begin{bmatrix} \boldsymbol{V}_1 \\ 0 \end{bmatrix} \tag{4.13}$$

with

$$\begin{cases} [Z_{ij}]_{mn} = \langle w_{i,m}, \mathcal{L}_{ij}(f_{j,n}) \rangle \\ [V_1]_m = \langle w_{1,m}, \varphi^{inc} \rangle \\ [I_1]_m = a_m, \quad [I_2]_m = b_m, \qquad\qquad i, j = 1, 2 \end{cases} \tag{4.14}$$

Equation (4.13) can be transformed into (2.24) by using either the CBS or the MTA with the wavelet transform matrix $\boldsymbol{W}$. In the case of the CBS, the multidimensional wavelets are required to construct $\boldsymbol{W}$, which can be obtained by simply using tensor products. To illustrate the idea, consider the case of a plane. Let

$$\Phi(x, y) = \phi(x)\phi(y) = \phi \otimes \phi(x, y) \tag{4.15}$$

with ϕ being the scaling functions for the selected wavelets and define $V_0 = Span\{\Phi(x - k_1, y - k_2;\ k_1,\ k_2 \in \mathbf{Z}\}$. Of course, if the set $\{\phi(x - l; l \in \mathbf{Z}\}$ is an orthogonal basis, the set $\{\Phi(x - k_1, y - k_2\}$ form an orthogonal basis for V_0. By dyadic scaling, one can obtain a multiresolutional analysis. The complement space W_0 of V_0 in V_1 is similarly generated by the translations of the three functions

$$\Psi^{(1)} = \phi \otimes \psi, \quad \Psi^{(2)} = \psi \otimes \phi, \quad \Psi^{(3)} = \psi \otimes \psi \tag{4.16}$$

where ψ is the corresponding wavelet function.

For a given function $\forall f(x,y) \in \boldsymbol{L}^2$, the following projection exists

$$f(x,y) = \sum_{i,l}\sum_{j,k} \langle f, \psi_{i,l} \otimes \psi_{j,k} \rangle \, \psi_{i,l} \otimes \psi_{j,k} \tag{4.17}$$

Thus, the wavelet transform matrix $\boldsymbol{W}$ can be obtained in a way similar as in the one-dimensional case. The gray-scaled images of the wavelet transform matrices of order 512×512 for Daubechies' wavelets with 8 vanishing moments are shown in Fig. 4.2, which clearly shows their differences.

The transformed matrices $\boldsymbol{Z}'$ with the CBS and the MTA are usually highly sparse due to the salient features of wavelets. However, the CBS will result in a better performance than the MTA in terms of matrix sparsity and solution accuracy, since the latter simply treats the unknown $\boldsymbol{I} = [\boldsymbol{I}_1, \boldsymbol{I}_2]^T$ in (4.13) as a vector, and the discontinuity between the two sub-unknowns $\boldsymbol{I}_1$ and $\boldsymbol{I}_2$ generates more matrix elements with a higher value.

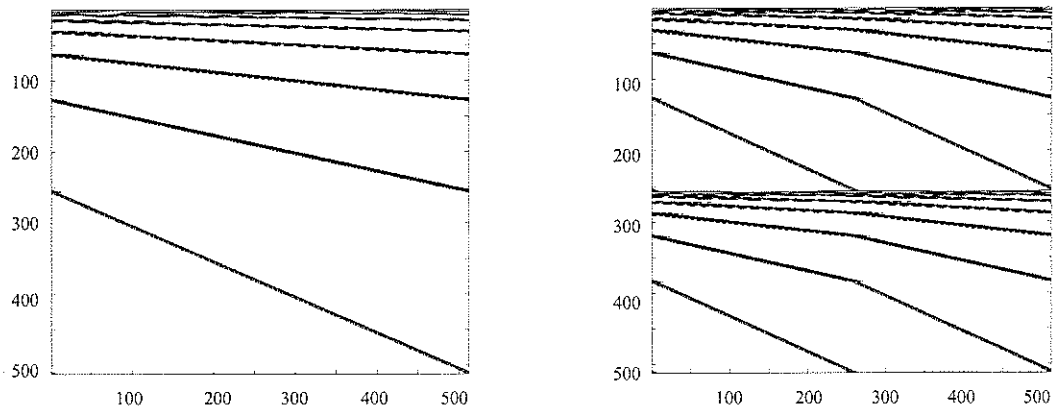

(a) (b)

Fig. 4.2. Gray-scaled images of wavelet transform matrices: (a) MTA; (b) CBS.

§4.4. Numerical Experiments

The above procedure was implemented to analyze numerically the electromagnetic wave scattering by various dielectric bodies. The basis functions $f_{i,n}(t)$ in (4.10) and the weighting functions $w_{i,n}(t)$ in (4.12) were chosen to be rectangular pulse functions. Daubechies' wavelets with 8 vanishing moments have been employed for the construction of wavelet transform matrices. To measure the performance of CBS and MTA, the relative solution error is defined as

$$S_{err} = \| \boldsymbol{I} - \boldsymbol{I}_{\delta} \| / \| \boldsymbol{I} \| \times 100\% \tag{4.18}$$

where $\boldsymbol{I}$ is the solution obtained with the conventional MoM and $\boldsymbol{I}_{\delta}$ is the one obtained by the present method with the threshold value δ.

The first example considered is a circular cylinder of relative permittivity $\varepsilon_r = 2.5$ and the electric radius $k_0 a = 50$ in free space, illuminated by a plane wave as shown in Fig. 4.6, where k_0 is the wave number of free space. To compare the efficiencies of the CBS and the MTA, computations were performed for different threshold values of δ, and the number of basis functions was kept $N = 512$. The sparsity S of the matrix $\boldsymbol{Z}'$ as a function of threshold value δ and the solution error S_{err} versus the matrix sparsity S are plotted in Figs 4.3 and 4.4, respectively. Both the MTA and the CBS result in highly sparse matrix equations, but the latter produces a higher matrix sparsity than the former, e.g., about 5% when $S_{err} = 10.50\ \%$. The structure of sparse matrices is shown in Fig. 4.5 for the case of $S_{err} = 10.50\ \%$, the corresponding E_z, $\boldsymbol{n} \cdot \nabla E_z$ and far-field RCS are plotted in Figs 4.6–4.9. Fig. 4.7 and Fig. 4.8 shows E_z on the surface of the cylinder and that inside and outside of

the cylinder along the y-axis, where the conventional MoM and the analytic solution are given as references.

The second example considered is the above circular dielectric cylinder with relative permittivity $\varepsilon_r = 40$. The number of basis functions was kept $N = 512$ as above. The relationship between S and δ is shown in Fig. 4.10, and that between S_{err} and S is given in Fig. 4.11. The MTA and the CBS produce highly sparse matrix equations, and the CBS again gives higher a matrix sparsity then MTA about 7% when $S_{err} = 10.05\%$. The sparse matrix structures are shown in Fig. 4.12, and corresponding E_z, $\boldsymbol{n} \cdot \nabla E_z$ and far-field RCS are plotted in Figs 4.13–4.16. Fig. 4.14 and Fig. 4.15 shows E_z on the surface of the cylinder and that inside and outside of the cylinder along the $y-$axis, here again the conventional MoM and the analytic solution are given as references

§4.5. Conclusions

MTA and CBS with orthogonal wavelets are studied for the analysis of scattering by two-dimensional dielectric bodies, formulated as coupled surface integral equations with two independent unknowns. Their efficiency is compared in terms of the matrix sparsity and the solution accuracy obtained with the standard LU solver. Numerical experiments are conducted for two-dimensional dielectric bodies of large size with typically large and small values of permittivity, namely $\varepsilon_r = 2.5, 40$. The MTA and the CBS both result in highly sparse matrix equations within the acceptable range of solution error, namely $S_{err} < 10.5\%$ in the examples considered, and CBS produces higher sparse matrices about 5% in the first example and 7% in the second example.

The MTA and the CBS are differentiated by the construction of wavelet transform matrices. The MTA simply requires one-dimensional wavelet, while the CBS needs multidimensional wavelets, which are tensor products of one-dimensional wavelets. The CBS gives rise to a better performance than the MTA in terms of matrix sparsity, the MTA, however, provides a problem-independent transform mechanism at the cost of matrix sparsity.

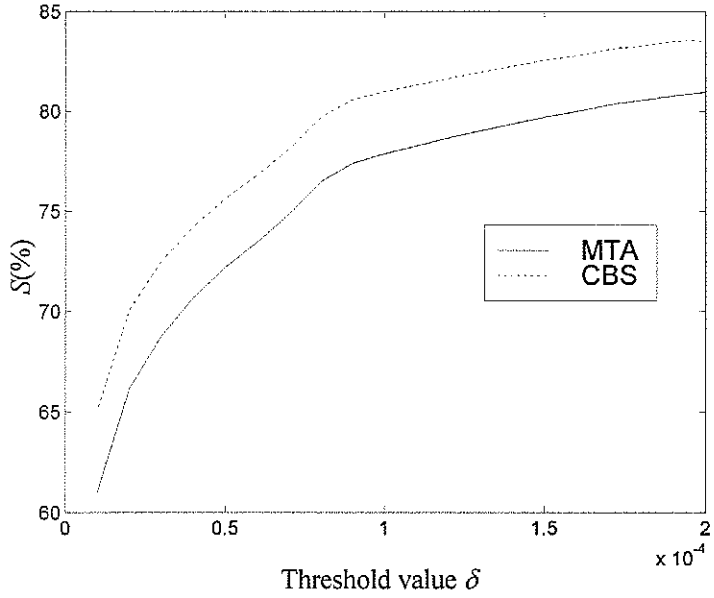

Fig. 4.3. Sparsity S as a function of threshold value δ for the dielectric cylinder in Fig. 4.6.

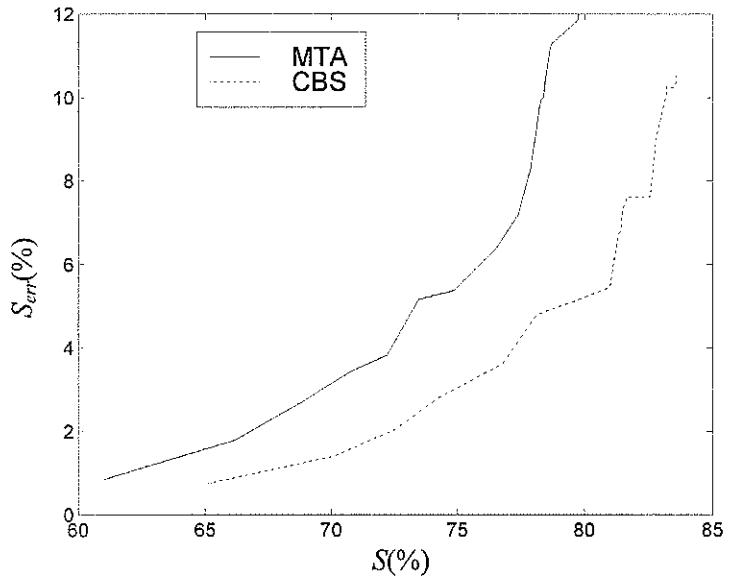

Fig. 4.4. Relative solution error S_{err} versus matrix sparsity S for the dielectric cylinder in Fig. 4.6.

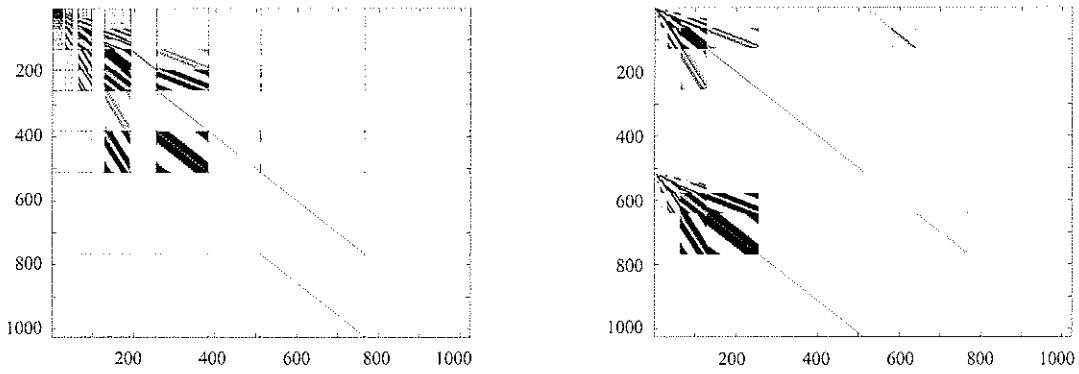

Fig. 4.5. Gray-scaled images of the transformed matrix $\boldsymbol{Z}'$ for the dielectric cylinder in Fig. 4.6 when $S_{err} = 10.50\%$: (a) S = 78.47% obtained with MTA and $\delta = 1.151 \times 10^{-4}$; (b) $S = 83.57\%$ obtained with CBS and $\delta = 1.95 \times 10^{-4}$.

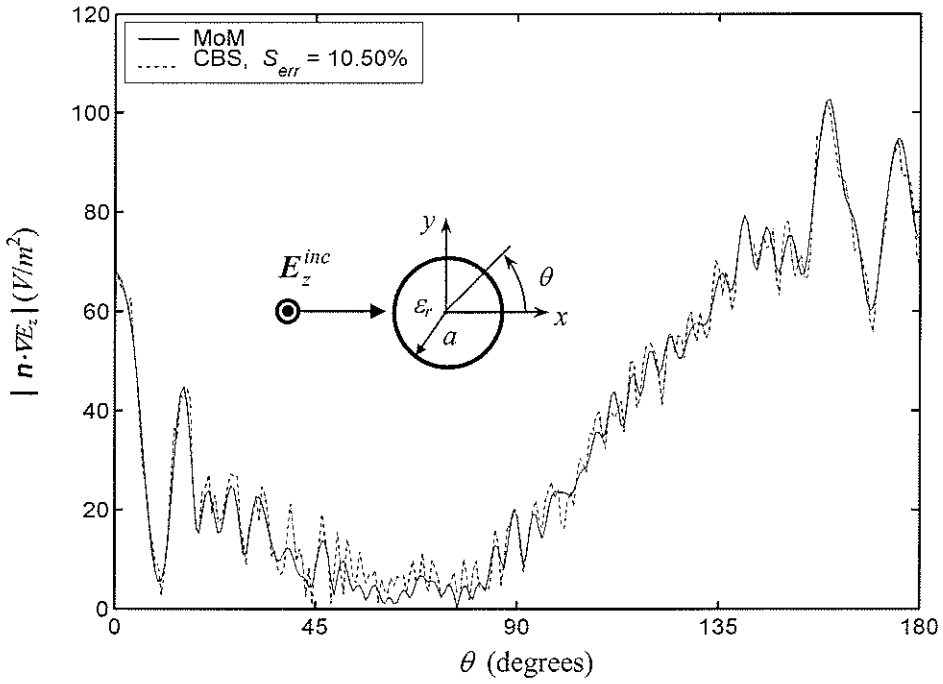

Fig. 4.6. $\boldsymbol{n}\cdot\nabla E_z$ on the surface of the dielectric cylinder of radius $k_0 a = 50$ and the relative dielectric constant $\varepsilon_r = 2.5$, when $S_{err} = 10.50\%$ for $E_z^{inc} = 1$ (V/m).

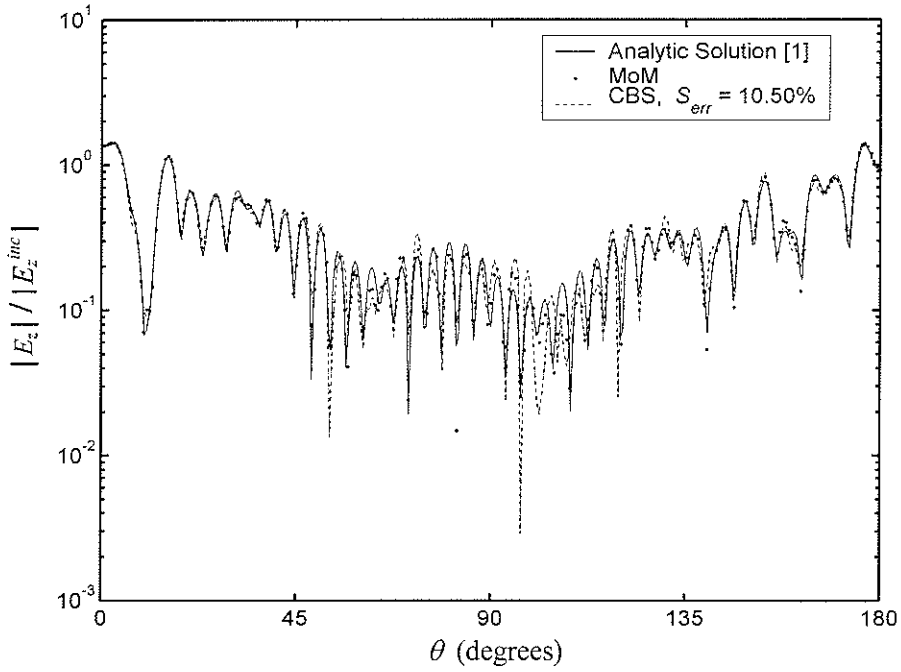

Fig. 4.7. E_z on the surface of the dielectric cylinder in Fig. 4.6.

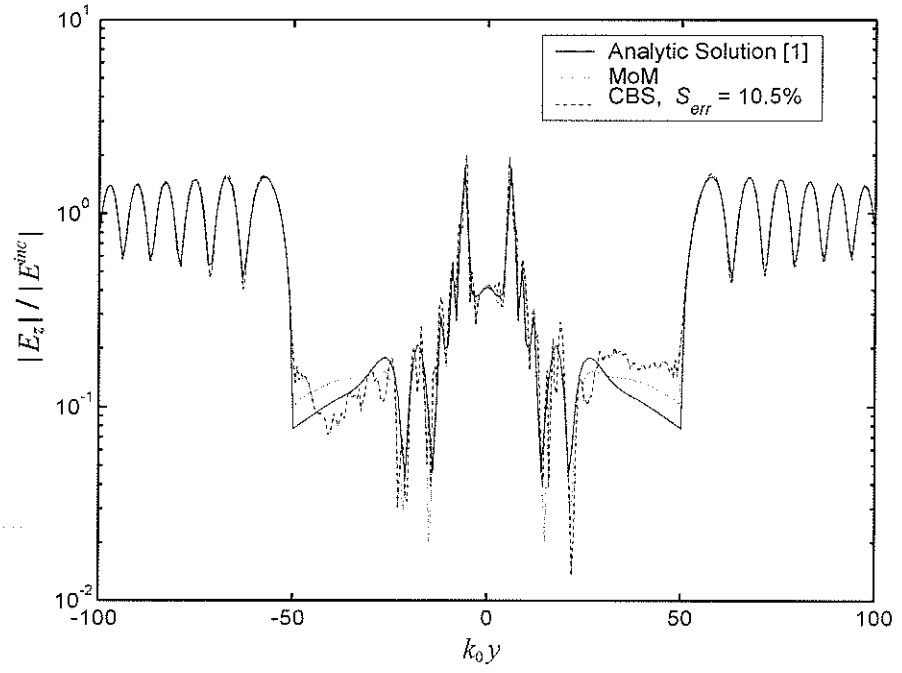

Fig. 4.8. E_z on the $y-$axis across the dielectric cylinder in Fig. 4.6.

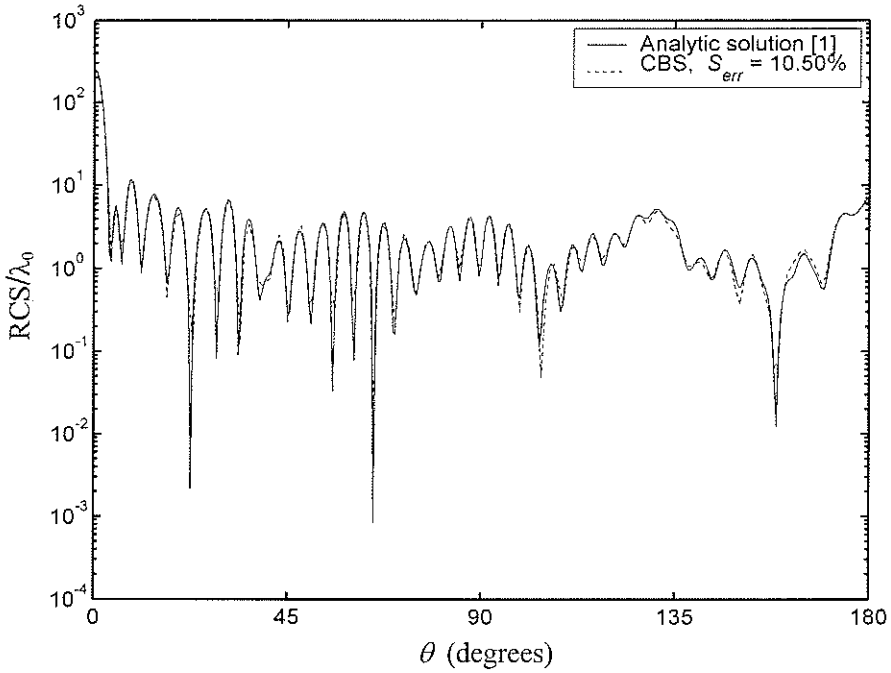

Fig. 4.9. Far-field RCS of the dielectric cylinder in Fig. 4.6.

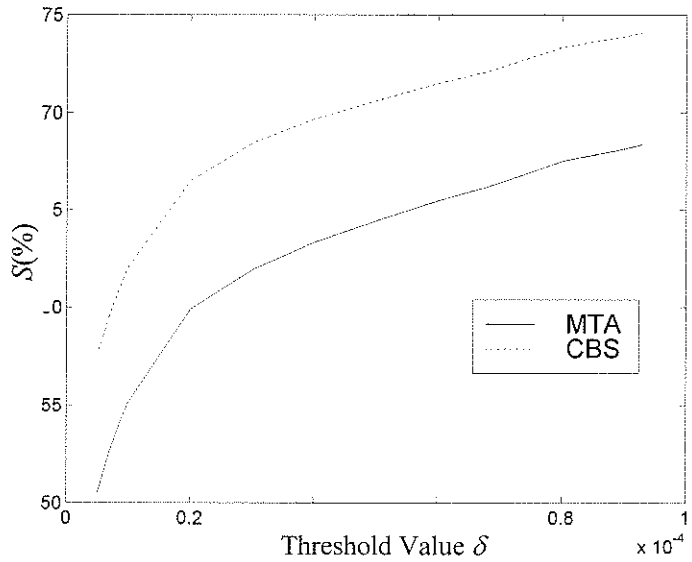

Fig. 4.10. Sparsity S as a function of threshold value δ for the dielectric cylinder in Fig. 4.13.

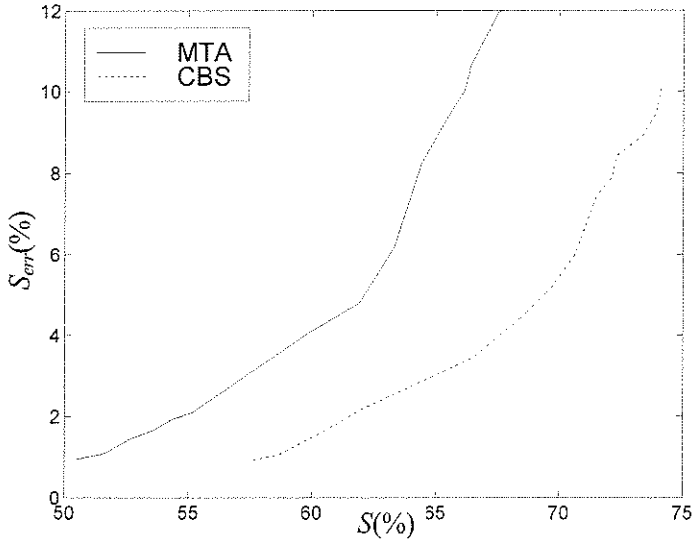

Fig. 4.11. Relative solution error S_{err} versus the matrix sparsity S for the dielectric cylinder in Fig. 4.13.

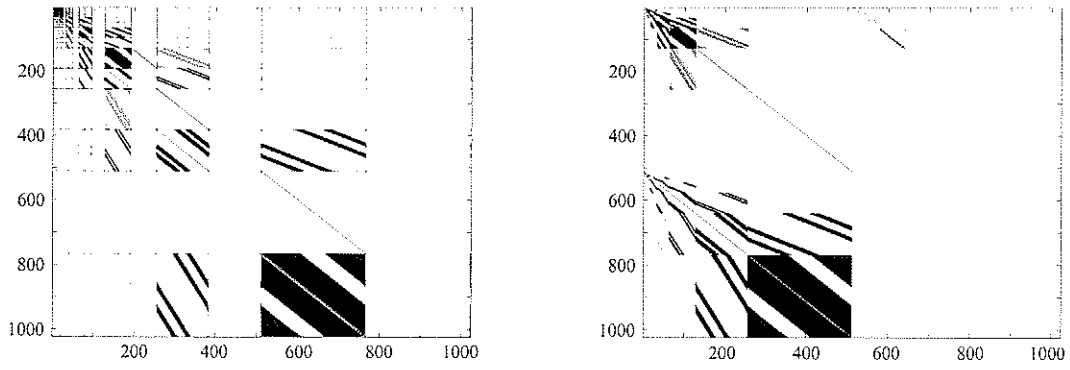

Fig. 4.12. Gray-scaled images of the transformed matrix $\boldsymbol{Z}'$ for the dielectric cylinder in Fig. 4.13, when $S_{err} = 10.05\%$: (a) $S = 66.17\%$ obtained with MTA and $\delta = 67.69 \times 10^{-6}$; (b) $S = 74.74\%$ obtained with CBS and $\delta = 92.94 \times 10^{-6}$.

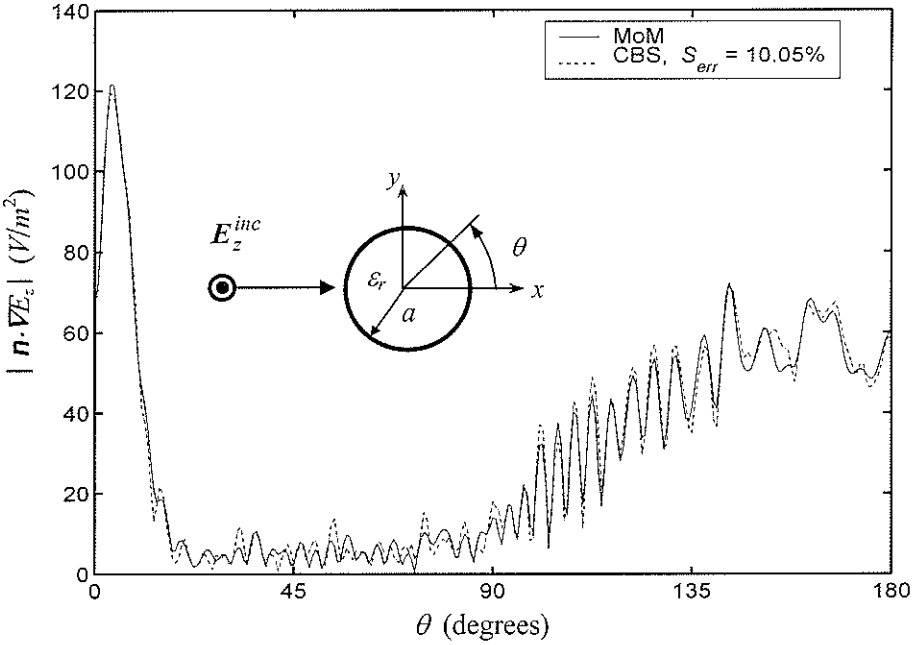

Fig. 4.13. $\boldsymbol{n}\cdot\nabla E_z$ on the surface of the dielectric cylinder of radius $k_0 a = 50$ and the relative permittivity $\varepsilon_r = 40$ for $E_z^{inc} = 1$ (V/m).

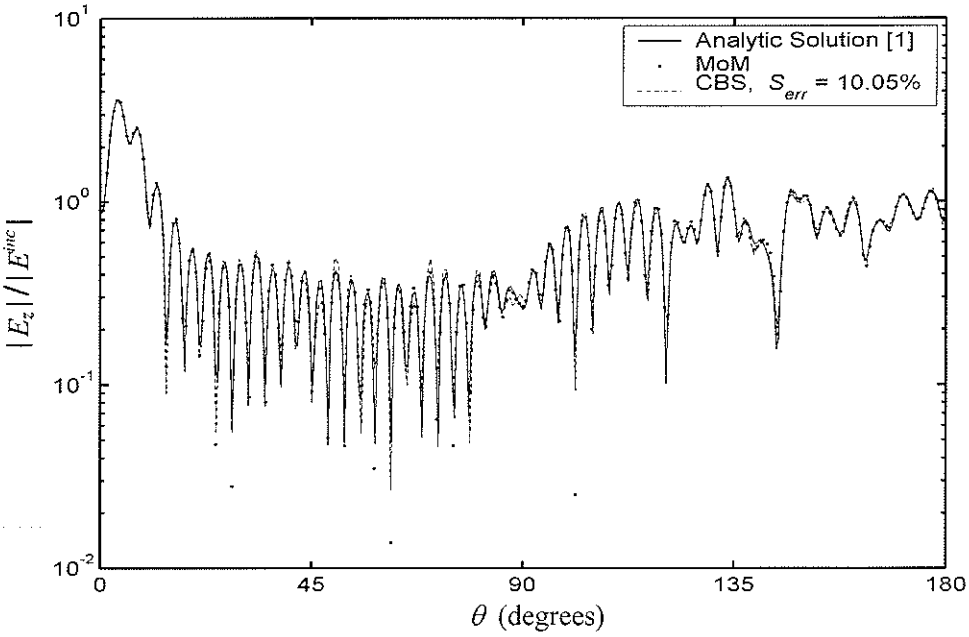

Fig. 4.14. E_z on the surface of the dielectric cylinder in Fig. 4.13.

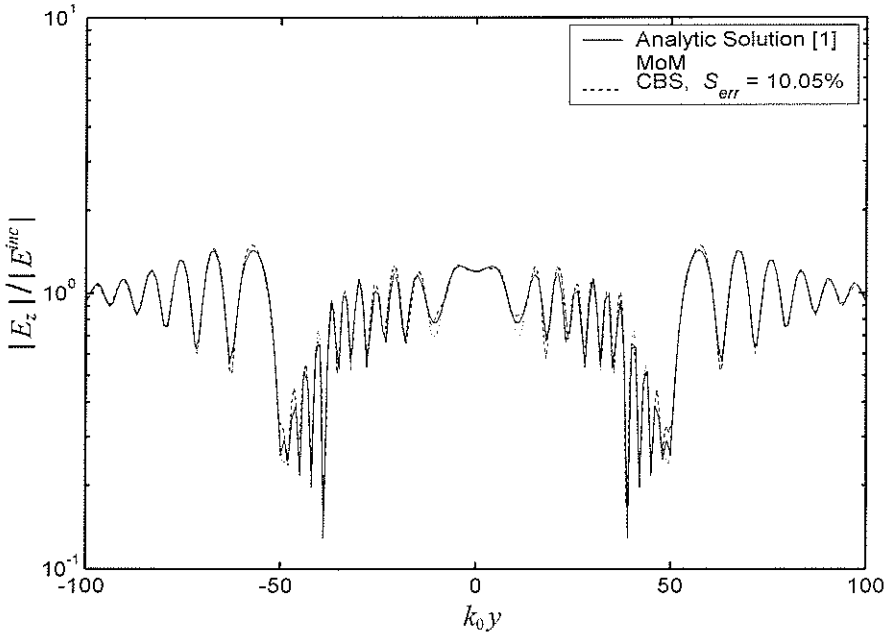

Fig. 4.15. E_z on the y – axis across the dielectric cylinder in Fig. 4.13.

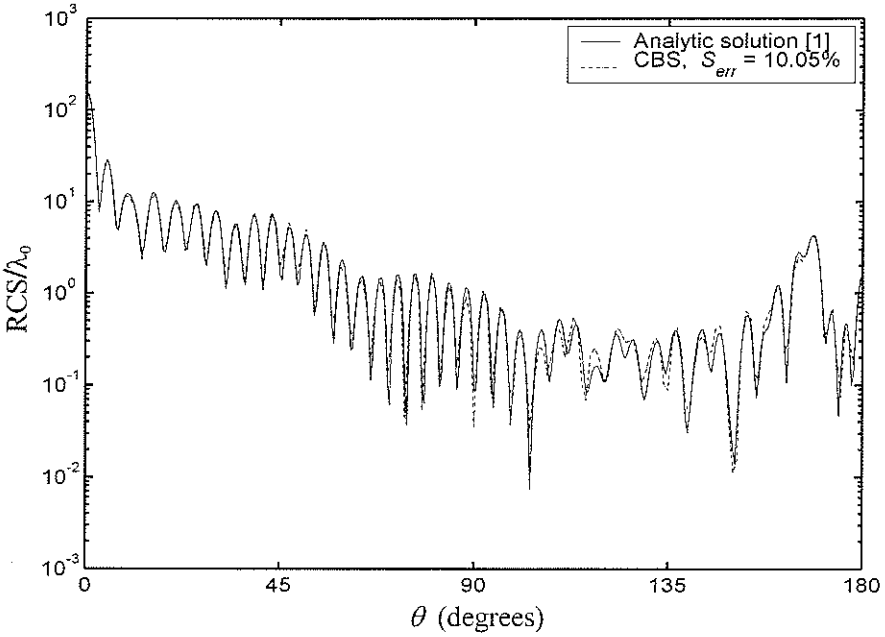

Fig. 4.16. Far-field RCS of the dielectric cylinder in Fig. 4.13.

Chapter 5

SCATTERING BY ARBITRARY BODIES OF REVOLUTION (BOR)

§5.1. Introduction

Scattering of electromagnetic waves by arbitrary BORs can be described by constructing coupled vector integro-differential equations which can be solved by taking advantage of the axial symmetry of the body [10], [13]. Considerable efforts have been made in recent years to enhance the computational efficiency for electrically large structures. The FFT was used in [23] to improve the matrix fill time. Entire-domain functions were also employed in order to reduce the size of moment-method matrices arising in the analysis of electrically large axially symmetric reflector antennas [25].

In this Chapter, the MTA with orthogonal wavelets is extended to the problem of scattering by arbitrary BORs. An efficient sparse solution technique that employs the generalized minimal residual (GMRES) method, which converges faster than other iterative methods [65], is demonstrated for the analysis of the electromagnetic scattering by a conducting BOR, where the mathematical model is reduced to a single vector integro-differential equation. A sparse LU decomposition method [60] with an approximate minimum degree ordering algorithm [56] is proposed for the case of dielectric BORs, whose moment-method matrices inherently possess a higher condition number. Numerical experiments are performed to evaluate the efficiency and accuracy of the solution techniques.

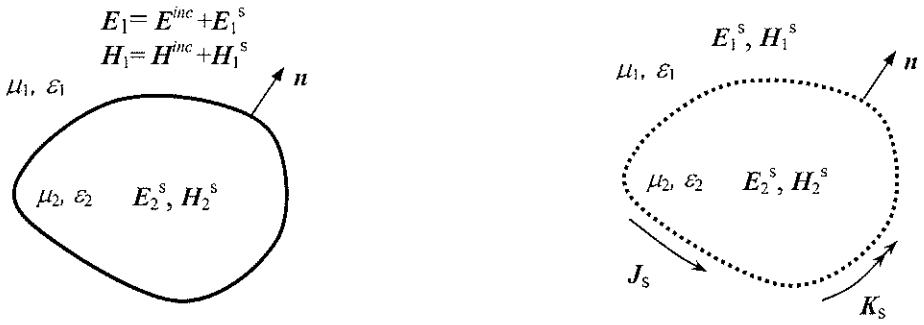

Fig. 5.1. Surface equivalence of an arbitrary homogeneous dielectric scatterer in an unbounded medium: (a) Original problem; (b) Replaced by the surface equivalent sources $\boldsymbol{J}_s = \boldsymbol{n} \times \boldsymbol{H}$ and $\boldsymbol{K}_s = -\boldsymbol{n} \times \boldsymbol{E}$.

§5.2. Surface Integral Equations

Consider a general radiation and scattering problem involving a homogeneous scatterer of permittivity ε_2 and permeability μ_2, illuminated by the incident fields $\boldsymbol{E}^{inc}$ and $\boldsymbol{H}^{inc}$ in an unbounded medium of ε_1 and μ_1 as shown in Fig. 5.1(a). According to the equivalent principle [1], the scatterer can be replaced by the surface current sources, $\boldsymbol{J}_s = \boldsymbol{n} \times \boldsymbol{H}$ and $\boldsymbol{K}_s = -\boldsymbol{n} \times \boldsymbol{E}$, which produce the scattered fields $\boldsymbol{E}^s$ and $\boldsymbol{H}^s$ as shown in Fig. 5.1(b). The integral equations for this problem can be obtained by requiring continuity of the fields tangential to the surface of the scatterer S

$$\boldsymbol{n}\times\boldsymbol{E}_1^s(\boldsymbol{J}_s,\boldsymbol{K}_s)+\boldsymbol{n}\times\boldsymbol{E}_2^s(\boldsymbol{J}_s,\boldsymbol{K}_s)=-\boldsymbol{n}\times\boldsymbol{E}^{inc} \tag{5.1}$$

$$\boldsymbol{n}\times\boldsymbol{H}_1^s(\boldsymbol{J}_s,\boldsymbol{K}_s)+\boldsymbol{n}\times\boldsymbol{H}_2^s(\boldsymbol{J}_s,\boldsymbol{K}_s)=-\boldsymbol{n}\times\boldsymbol{H}^{inc} \tag{5.2}$$

where $\boldsymbol{n}$ is the unit vector normal to the surface S of the body as shown in Fig. 5.1. The fields radiated by the equivalent currents in a homogenous region can be computed in terms of electric and magnetic vector and scalar potentials as

$$\boldsymbol{E}_l^s(\boldsymbol{J}_s,\boldsymbol{K}_s)=-j\omega\boldsymbol{A}_l-\nabla\Phi_l-\frac{1}{\varepsilon_l}\nabla\times\boldsymbol{F}_l \tag{5.3}$$

$$\boldsymbol{H}_l^s(\boldsymbol{J}_s,\boldsymbol{K}_s)=-j\omega\boldsymbol{F}_l-\nabla\Psi_l+\frac{1}{\mu_l}\nabla\times\boldsymbol{A}_l \tag{5.4}$$

with

$$\begin{cases}\boldsymbol{A}_l=\mu_l\iint_S\boldsymbol{J}_sG_l\,ds, & \Phi_l=\dfrac{1}{\varepsilon_l}\iint_S q_eG_l\,ds\\[2ex] \boldsymbol{F}_l=\varepsilon_l\iint_S\boldsymbol{K}_sG_l\,ds & \Psi_l=\dfrac{1}{\mu_l}\iint_S q_mG_l\,ds\end{cases} \tag{5.5}$$

where

$$G_l=e^{-j\beta_l|\boldsymbol{r}-\boldsymbol{r}'|}\big/(4\pi|\boldsymbol{r}-\boldsymbol{r}'|),\qquad l=1,2 \tag{5.6}$$

$j\equiv\sqrt{-1}$, $\beta_l=\omega\sqrt{\varepsilon_l\mu_l}$, and ε_l and μ_l are the permittivity and permeability, respectively, of the material outside and inside the body. A time-dependence factor $e^{j\omega t}$ is assumed but suppressed throughout. The electric and magnetic surface charge densities, q_e and q_m, are related to their corresponding surface current densities through the equation of continuity

$$q_e = -\frac{1}{j\omega}\nabla_s \cdot \boldsymbol{J}_s, \qquad q_m = -\frac{1}{j\omega}\nabla_s \cdot \boldsymbol{K}_s \tag{5.7}$$

Now, equations (5.1) and (5.2) can be written symbolically as

$$\begin{cases} \boldsymbol{n} \times \boldsymbol{E}^{inc} = \mathcal{L}_{11}(\boldsymbol{J}_s) + \mathcal{L}_{12}(\boldsymbol{K}_s) \\ \boldsymbol{n} \times \boldsymbol{H}^{inc} = \mathcal{L}_{21}(\boldsymbol{J}_s) + \mathcal{L}_{22}(\boldsymbol{K}_s) \end{cases} \tag{5.8}$$

with the integro-differential operators are

$$\begin{cases} \mathcal{L}_{11}(\boldsymbol{J}_s) = \boldsymbol{n} \times \int_S \{ j\omega \boldsymbol{J}_s(\boldsymbol{r}')(\mu_1 G_1 + \mu_2 G_2) \\ \qquad -[(\nabla_s' \cdot \boldsymbol{J}_s(\boldsymbol{r}'))/(j\omega)]\nabla(G_1/\varepsilon_1 + G_2/\varepsilon_2)\} ds' \\ \mathcal{L}_{12}(\boldsymbol{K}_s) = -\boldsymbol{n} \times \int_S \boldsymbol{K}_s(\boldsymbol{r}') \times \nabla(G_1 + G_2) ds' \\ \mathcal{L}_{21}(\boldsymbol{J}_s) = \boldsymbol{n} \times \int_S \boldsymbol{J}_s(\boldsymbol{r}') \times \nabla(G_1 + G_2) ds' \\ \mathcal{L}_{22}(\boldsymbol{K}_s) = \boldsymbol{n} \times \int_S \{ j\omega \boldsymbol{K}_s(\boldsymbol{r}')(\varepsilon_1 G_1 + \varepsilon_2 G_2) \\ \qquad -[(\nabla_s' \cdot \boldsymbol{K}_s(\boldsymbol{r}'))/(j\omega)]\nabla(G_1/\mu_1 + G_2/\mu_2)\} ds' \end{cases} \tag{5.9}$$

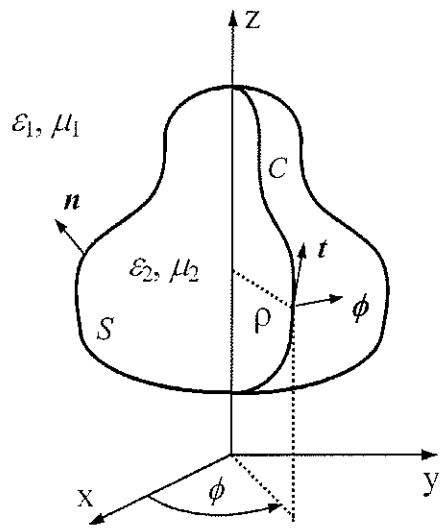

Fig. 5.2. Dielectric body of revolution.

§5.3. Method of Solution

When the scattering body is an arbitrary dielectric BOR about the z – axis, as shown in Fig. 5.2, (5.8) can be efficiently solved by taking advantage of the rotational symmetry. Because of this symmetry, a Fourier series expansion in the angle ϕ can reduce the problem to the solution of a system of orthogonal modes. The main advantage of using the Fourier modes is that the scattering problem can be solved mode by mode due their orthogonality.

The integro-differential equations (5.8) can be transformed into a system of linear algebraic equations through the application of the method of moments exploiting the system axisymmetry. Namely, the unknown current densities are first expressed in terms of Fourier modes as

$$\boldsymbol{M}_s(t,\phi) = \sum_n [\boldsymbol{M}_n^t(t) + \boldsymbol{M}_n^\phi(t)] e^{jn\phi}, \quad \boldsymbol{M}_s = \boldsymbol{J}_s, \boldsymbol{K}_s \tag{5.10}$$

where $\boldsymbol{M}_n^t$ and $\boldsymbol{M}_n^\phi$ are components along the tangential unit vectors $\boldsymbol{t}$ and $\boldsymbol{\phi}$, respectively, and t is the length variable along the generator curve C of the BOR. The current densities can further be expanded as

$$\begin{cases} \boldsymbol{J}_n^p(t) = \boldsymbol{p} \sum_{k=1}^{N} I_{nk}^{p,e} f_k(t) \\ \boldsymbol{K}_n^p(t) = \boldsymbol{p} \sum_{k=1}^{N} I_{nk}^{p,m} f_k(t), \qquad \boldsymbol{p} = \boldsymbol{t}, \boldsymbol{\phi} \end{cases} \tag{5.11}$$

where N is the total number of basis functions f_k used along C. Choosing the weighting functions

$$\boldsymbol{W}_{ni}^p(t) = \boldsymbol{p} w_i(t) e^{-jn\phi}, \qquad \boldsymbol{p} = \boldsymbol{t}, \boldsymbol{\phi}; \quad i = 1, 2, \cdots N \tag{5.12}$$

the application of MoM yields a system $\boldsymbol{ZI} = \boldsymbol{V}$ of $4N \times 4N$ linear equations for each n in the form

$$\begin{bmatrix} \boldsymbol{Z}_{11,n}^{tt} & \boldsymbol{Z}_{11,n}^{t\phi} & \boldsymbol{Z}_{12,n}^{tt} & \boldsymbol{Z}_{12,n}^{t\phi} \\ \boldsymbol{Z}_{11,n}^{\phi t} & \boldsymbol{Z}_{11,n}^{\phi\phi} & \boldsymbol{Z}_{12,n}^{\phi t} & \boldsymbol{Z}_{12,n}^{\phi\phi} \\ \boldsymbol{Z}_{21,n}^{tt} & \boldsymbol{Z}_{21,n}^{t\phi} & \boldsymbol{Z}_{22,n}^{tt} & \boldsymbol{Z}_{22,n}^{t\phi} \\ \boldsymbol{Z}_{21,n}^{\phi t} & \boldsymbol{Z}_{21,n}^{\phi\phi} & \boldsymbol{Z}_{22,n}^{\phi t} & \boldsymbol{Z}_{22,n}^{\phi\phi} \end{bmatrix} \begin{bmatrix} \boldsymbol{I}_n^{t,e} \\ \boldsymbol{I}_n^{\phi,e} \\ \boldsymbol{I}_n^{t,m} \\ \boldsymbol{I}_n^{\phi,m} \end{bmatrix} = \begin{bmatrix} \boldsymbol{V}_n^{t,e} \\ \boldsymbol{V}_n^{\phi,e} \\ \boldsymbol{V}_n^{t,m} \\ \boldsymbol{V}_n^{\phi,m} \end{bmatrix} \tag{5.13}$$

with the matrix elements

$$\begin{cases} [V_n^{p,e}]_i = \langle \boldsymbol{W}_{ni}^p, \boldsymbol{E}^{inc} \rangle \\ [V_n^{p,m}]_i = \langle \boldsymbol{W}_{ni}^p, \boldsymbol{H}^{inc} \rangle \\ [Z_{ab,n}^{pq}]_{ik} = \langle \boldsymbol{W}_{ni}^p, \mathcal{L}_{ab}(\boldsymbol{F}_{nk}^q) \rangle, \quad a, b = 1, 2;\ p, q = t, \phi;\ i, k = 1, 2, \cdots N \end{cases} \tag{5.14}$$

and $\boldsymbol{F}_{nk}^q = \boldsymbol{q} f_k(t) e^{jn\phi}$. The inner products in (5.14) can be evaluated in the form of integrals along the generator curve C of the body, for example

$$\begin{cases} [Z_{11,n}^{tt}]_{ik} = \int_C dt \int_C dt' \{ j\omega w_i(t) f_k(t') [\sin\gamma(t)\sin\gamma(t') \cdot [\mu_1 (g_{n+1}^{(1)} + g_{n-1}^{(1)}) \\ \qquad + \mu_2 (g_{n+1}^{(2)} + g_{n-1}^{(2)})]/2 + \cos\gamma(t)\cos\gamma(t')(\mu_1 g_n^{(1)} + \mu_2 g_n^{(2)})] \\ \qquad + [w_i'(t) f_k'(t')/(j\omega)](g_n^{(1)}/\varepsilon_1 + g_n^{(2)}/\varepsilon_2)\} \\ [Z_{22,n}^{t\phi}]_{ik} = \int_C dt \int_C dt' \{ -\omega w_i(t) f_k(t') \sin\gamma(t) \cdot [\varepsilon_1 (g_{n+1}^{(1)} - g_{n-1}^{(1)}) \\ \qquad + \varepsilon_2 (g_{n+1}^{(2)} - g_{n-1}^{(2)})]/2 + n[w_i'(t) f_k(t')/(\omega\rho(t'))](g_n^{(1)}/\mu_1 + g_n^{(2)}/\mu_2)\} \end{cases} \tag{5.15}$$

where $g_n^{(l)}$ represents the $n-$th Fourier mode of G_l in (5.6) and γ denotes the angle between the unit vectors $\boldsymbol{t}$ and $\boldsymbol{z}$, being positive if $\boldsymbol{t}$ points away from the $z-$axis and negative if $\boldsymbol{t}$ points towards the $z-$axis. Several formulas to facilitate the computation above should be noted:

$$\nabla' \cdot \boldsymbol{J}_s = \{ \frac{1}{\rho'} \frac{\partial}{\partial t'} [\rho' \boldsymbol{J}^t(t')] + \frac{jn}{\rho'} \boldsymbol{J}^{\phi}(t') \} e^{jn\phi'} \tag{5.16}$$

$$\begin{cases} G_l(t,t',\phi-\phi') = \dfrac{1}{2\pi}\sum_n g_n^{(l)}(t,t')e^{jn(\phi-\phi')} \\ \\ g_n^{(l)}(t,t') = \int_0^{2\pi} G_l(t,t',\alpha)e^{-jn\alpha}d\alpha \end{cases} \tag{5.17}$$

with the coordinate transform

$$\begin{cases} \boldsymbol{n} = \boldsymbol{x}\cos\gamma\cos\phi + \boldsymbol{y}\cos\gamma\sin\phi - \boldsymbol{z}\sin\gamma \\ \\ \boldsymbol{t} = \boldsymbol{x}\sin\gamma\cos\phi + \boldsymbol{y}\sin\gamma\sin\phi + \boldsymbol{z}\sin\gamma \\ \\ \boldsymbol{\phi} = -\boldsymbol{x}\sin\phi + \boldsymbol{y}\cos\phi \end{cases} \tag{5.18}$$

Finally, the unknown current density coefficients can be found by solving the matrix equations (5.8), and the far field and radar cross section (RCS) can be calculated through the procedure described in [10], [13]. In what follows, an efficient and accurate numerical solution of (5.8) is analyzed in detail.

§5.4. Solution Techniques for Sparse Matrix Equations

Although both orthogonal and semi-orthogonal wavelets have been frequently used for the solution of electromagnetic integral equations, yielding highly sparse moment-method matrices, we have shown in Chapter 3 that the condition number of $\boldsymbol{W}$ is 141 in the case of SOW with 8 vanishing moments, such that the condition number of the transformed matrices is considerably increased, while it is 1 in the case of the DOW, which is optimal. Here, the orthogonal wavelet transformation scheme is extended to the problem of scattering by arbitrary BORs.

Implementing a thresholding procedure with appropriate threshold value δ, the transformed matrix $\boldsymbol{Z}'$ becomes a sparse matrix. In order to accelerate the iterative solution algorithm, the elements of $\boldsymbol{Z}'$ are arranged using the "row-indexed sparse storage mode" [45], where the solution is practically proportional to the matrix sparsity in time.

§5.4.1. Conducting BORs

The GMRES iterative algorithm described in [65] is implemented to obtain the fast solution of the derived sparse matrix equation since it converges faster than other iterative algorithms and also due to the fact that the orthogonality of the wavelets used provides an efficient way to select the termination criterion for the iterative process. Since the Euclidean norm $\|\boldsymbol{W}\| = 1$ for the orthogonal wavelets, the residual error r for the solution of (5.13), defined by $r = \|\boldsymbol{ZI} - \boldsymbol{V}\| / \|\boldsymbol{V}\|$, is equal to the residual error $r' = \|\boldsymbol{Z'I'} - \boldsymbol{V'}\| / \|\boldsymbol{V'}\|$ for the solution of the transformed matrix equation (2.24) before thresholding. Recognizing this, a solution of (5.13) with a required accuracy ε is sought for by using the generalized minimal residual (GMRES) algorithm in two steps. First, the sparse matrix equation obtained after thresholding (5.13) with a threshold value δ is solved imposing the same accuracy ε such that the residual error r_δ for this matrix equation is minimized to r_δ^ε. Then, the error r is checked, and the iterative procedure is terminated if $r \le \varepsilon$, otherwise the GMRES algorithm is restarted with the new termination criterion $\left| r_\delta - r_\delta^\varepsilon + \Delta \right| \le \varepsilon_\delta$, $\Delta = \left| r - r_\delta^\varepsilon \right|$ being determined in the previous step and ε_δ being a predefined accuracy less than ε. Note that the error Δ is a quantification of the influence of thresholding on the residual error r. This error is usually small since a very small value of δ is used in practice. Thus, in the second

step the GMRES iterative process converges fast and the solution of (5.13) can be found by computing only one full matrix-vector multiplication used to evaluate r. This procedure was tested by numerical experiments and found to be more efficient than that used in [45], where a smaller value of the residual error is required for the termination criterion to ensure that the conjugate gradient iterative algorithm yields a solution of the original moment-method equation with the residual error ε.

§5.4.2. Dielectric BORs

The original MoM matrix $\boldsymbol{Z}$ inherently possesses a high condition number in the case of dielectric BORs. This is confirmed by numerical experiments conducted, where iterative solution algorithms for (5.13), such as the conjugate and bi-conjugate gradients, and also the GMRES method, fail to converge to an accuracy of 1% in the residual error for the problems considered in this paper.

The condition number of various wavelet transform matrices has been studied in Chapter 2. It was pointed out that the condition number of $\boldsymbol{W}$ is always 1 in the case of orthogonal wavelets, which is optimal. By using such wavelets, the condition number of $\boldsymbol{Z}$ in (5.13) will be preserved after the wavelet transformation. To treat more efficiently the matrix equations (2.24) and to take full advantage of the sparsity of the transformed impedance matrices, an improved sparse LU decomposition solver [60] has been implemented, which dynamically allocates the computer memory needed and employs an approximate minimum degree ordering algorithm [56] to further increase the sparsity of the computed L and U factors.

§5.5. Numerical Experiments

Based on the procedure described above, a computer program has been written to analyse the problem of electromagnetic wave scattering by an arbitrary BOR. The functions $f_k(t)$ in (5.11) and $w_i(t)$ in (5.12) were chosen to be triangular pulse functions, and elements of $\boldsymbol{Z}$ and $\boldsymbol{V}$ in (5.13) were evaluated following the procedure described in [13]. The Daubechies' wavelet [5] with 8 vanishing moments has been employed for the transform in (2.25). Since the main source of errors is the thresholding level in the transformed impedance matrices, the threshold value δ was taken as one of the input parameters of the computer program and an appropriate value of it has been selected. A numerical solution with 1% relative error in the residual vector norm was sought for the results generated. The sparsity of a matrix has been defined in (3.7). Numerical experiments were conducted for various BORs. The plane of incidence of plane wave is assumed to be at $\phi = 0^\circ$ and $\theta = 180^\circ$, and the current densities are obtained in the form

$$\begin{cases} \boldsymbol{J}_s(t,\phi) = \boldsymbol{t} J_s^t(t)\cos\phi + \boldsymbol{\phi} J_s^\phi(t)\sin\phi \\ \boldsymbol{K}_s(t,\phi) = \boldsymbol{t} K_s^t(t)\sin\phi + \boldsymbol{\phi} K_s^\phi(t)\cos\phi \,. \end{cases} \tag{5.19}$$

§5.5.1. Conducting BORs

A solution of (5.13) is sought by using the GMRES iterative process described above, with $\varepsilon = 0.01$ as in [45] and $\varepsilon_\delta = 0.0001$. Numerical experiments were performed on a Pentium 120 personal computer.

The first example considered is that of the conducting sphere with a radius $\beta_0 a$ illuminated by an axially incident plane wave as shown in Fig. 5.3, where β_0 is the wave number of the incident field in free space. To illustrate the efficiency of the present method, experiments were conducted for different large electrical dimensions namely $\beta_0 a = 25.6$, 51.2, and 102.4, while the number of basis functions per wavelength was kept 20 as in [23]. Figs. 5.2 and 5.3 show the computed $\boldsymbol{E}-$ and $\boldsymbol{H}-$plane radar cross section (RCS) for $\beta_0 a = 51.2$ obtained by the present method in comparison with that by the conventional MoM with the LU solver. The sparse matrix with S = 11.28%, obtained from $\boldsymbol{Z}'$ with a small threshold value $\delta = 9 \times 10^{-6}$ is shown in Fig. 5.5. Table 5.1 illustrates the efficiency of the method presented as compared to the MoM with the LU solver. A highly sparse matrix is produced with smaller δ in all cases, and the matrix sparsity increases with the increase of the matrix size since more wavelets now are involved. 45.04% to 80.09% reduction in CPU time can be observed, i.e. 1.9 to 5 times, with the time used to perform the FWT included. It should be remarked that the computational efficiency increases with the matrix size, which recommends the method presented for an efficient solution of electrically large problems.

The second example considered is that of a conducting cone with spherical caps illuminated by an axially incident plane wave as shown in Fig. 5.6. The efficiency of the proposed procedure is examined for fixed dimensions of the body, $\beta_0 a = 12$, $\beta_0 b = 6$, and $\beta_0 h = 48$, but with the total number N of basis functions considered along the generator curve of the body taken to be 256 and then increased to 512. A more densely sampling usually results in moment-method equations with a higher condition number. The computed $\boldsymbol{E}-$ and $\boldsymbol{H}-$plane RCS are plotted in Figs. 5.5 and 5.6, respectively, and the results

obtained by the MoM with the LU solver are also given as reference. As shown in Table 5.2, 48.92% and 78.29% reductions in CPU time are obtained in comparison with the MoM employing the LU solver for the case of $N = 256$ (matrix size 512×512) and 512 (matrix size 1024×1024), respectively. As expected, the reduction in computation time is increased as compared to the corresponding cases in the first example.

§5.5.2. Dielectric BORs

The first example considered is that of a dielectric sphere of relative permittivity $\varepsilon_r = 8$ and normalized radius $\beta_0 a$ in free space, illuminated by a plane wave, as shown in Fig. 5.8. To illustrate the efficiency of the presented method, computations were performed for different electric dimensions, namely $\beta_0 a = 12.8$, 25.6, and 51.2, while the number of basis functions per wavelength was kept 20.

The normalized values of $|J_s^t(t)|$, $|J_s^\phi(t)|$, $|K_s^t(t)|$, and $|K_s^\phi(t)|$ for the sphere with $\beta_0 a = 12.8$ and its RCS are plotted in Figs. 5.7, 5.8, and 5.9, respectively, where the results obtained by the conventional MoM with the LU decomposition algorithm are also given as reference. The structure of the sparse matrix with the sparsity $S = 33.42\%$ is indicated qualitatively in Fig. 5.11. As shown in Table 5.3, a 50% to 73% reduction in CPU time, including the time to perform the FWT, is achieved with respect to the reference method, i.e. about 2 to 4 times faster in the case of the larger sphere.

Another example given here is that of a cone-sphere object with the relative permittivity $\varepsilon_r = 12$, the cone angle $\alpha = 50^\circ$, and the sphere radius $\beta_0 a$ in free space, illuminated by a plane wave axially incident on the cone vertex, as shown in Fig. 6. Again, to examine the

efficiency of the method employed, the same numerical experiments as in the previous example were performed for various body dimensions, namely for $\beta_0 a = 10$, 20, and 40, with approximately 20 cells per wavelength along the object generator curve. For the case of $\beta_0 a = 10$ and $N = 128$, the surface electric and magnetic current densities, as well as the RCS computed by the presented method, are plotted in Figs. 5.11, 5.12, and 5.13, respectively, along with those obtained by the conventional MoM. As shown in Table 5.4, a 41% to 67% reduction in CPU time, including the time used to perform the FWT, is achieved with respect to the conventional method.

§5.6. Conclusions

A fast solution technique based on the FWT and using sparse matrix solvers has been investigated for the problem of wave scattering by a dielectric BOR, whose MoM matrix equation inherently possesses a high condition number. The MTA with orthogonal wavelets is adapted to obtain highly sparse matrices, as well as to preserve the condition number of the original moment-method matrices. The sparse structures of the resulting matrices are exploited to speed up their numerical solution.

A new approach is proposed for the case of conducting BORs, where a solution of the original moment-method equations is obtained by applying the GMRES iterative algorithm for achieving a given accuracy, taking into account the influence of thresholding by implementing an effective termination criterion that exploits the orthogonal property of wavelets. The computational efficiency of this method has been illustrated by comparing it with the conventional MoM using a direct solver for different numbers of basis functions per

wavelength. Various numerical results generated show that the method presented is an efficient tool for the analysis of wave scattering by conducting bodies of revolution

In the case of dielectric BORs, the MoM matrix equation inherently possesses a high condition number, such that iterative methods fail to converge to a 1% solution error. The improved sparse LU decomposition technique [60] with dynamic memory allocation and with an approximate minimum degree-ordering algorithm [56] is proposed to exploit the sparse structures of the resulting matrices. The computation efficiency of this method has been illustrated by comparison with the conventional MoM for various dimensions of different BORs. Numerical results obtained show that the method presented is highly efficient for the analysis of wave scattering, especially for bodies whose linear dimensions are large with respect to the wavelength. As seen from TABLES 5.3 and 5.4, the reduction of the computation time increases with the electric size of the body, the method developed being, for instance, more than three times faster when $\beta_0 a = 40$ for the cone-sphere scatterer. Accurate results are obtained not only for the far-field RCS, but also for the field quantities on the surface of the body.

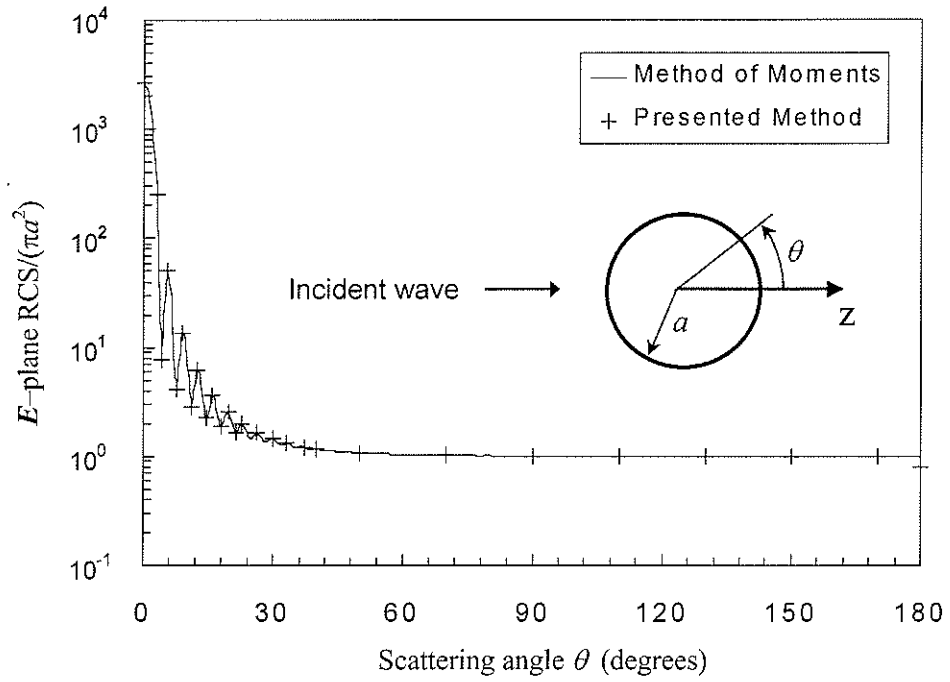

Fig. 5.3. $\boldsymbol{E}$ –plane RCS for a conducting sphere of radius $\beta_0 a = 51.2$.

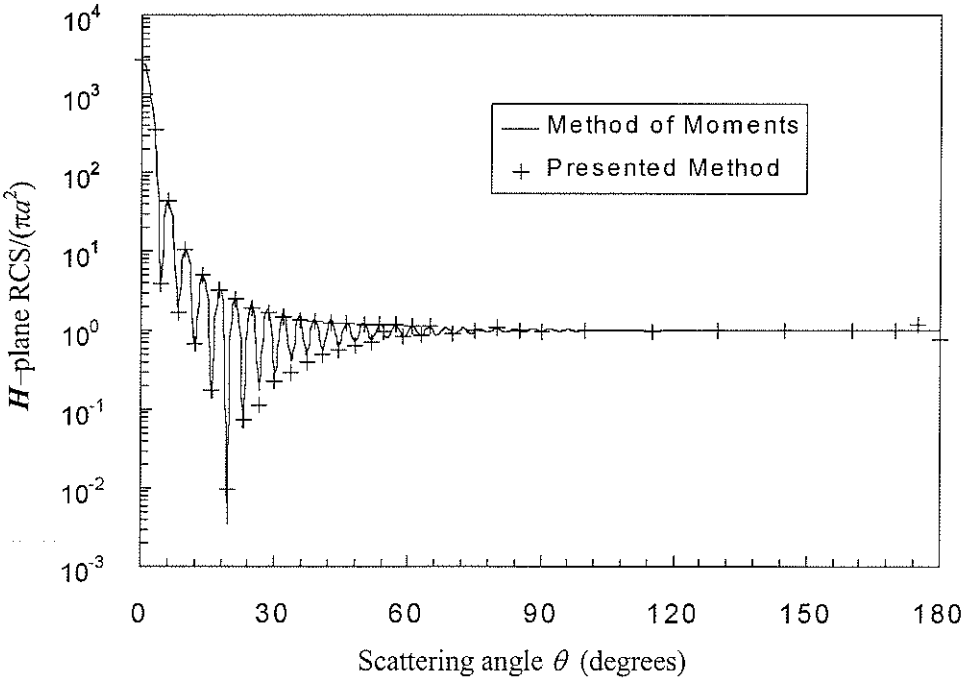

Fig. 5.4. $\boldsymbol{H}$ –plane RCS for the conducting sphere in Fig. 5.3.

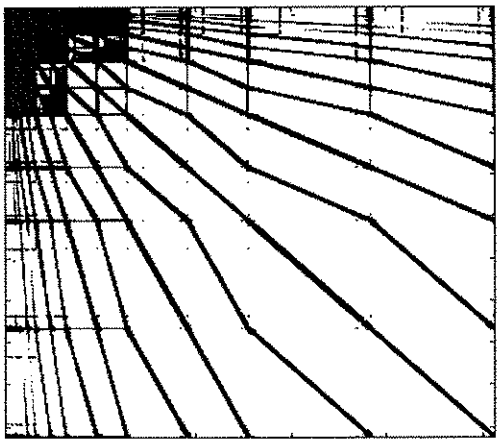

Fig. 5.5. Structure of the sparse matrix with $S = 88.72\%$ obtained after thresholding $\boldsymbol{Z}'$ with $\delta = 9 \times 10^{-6}$ for the conducting sphere in Fig. 5.3.

TABLE 5.1. EFFICIENCY FOR CONDUCTING SPHERES OF LARGE SIZES.

$\beta_0 a$	Matrix Size	Threshold Value δ	Sparsity S (%)	CUP Time in Seconds		Reduction in CPU Time (%)
				FWT + GMRES	LU	
25.6	512 × 512	3.5×10^{-5}	84.63	22.31 + 24.98	86.01	45.04
51.2	1024 × 1024	9×10^{-6}	88.72	91.83 + 154.47	761.41	67.65
102.4	2048 × 2048	6×10^{-6}	92.85	595.94 + 690.19	6462.85	80.09

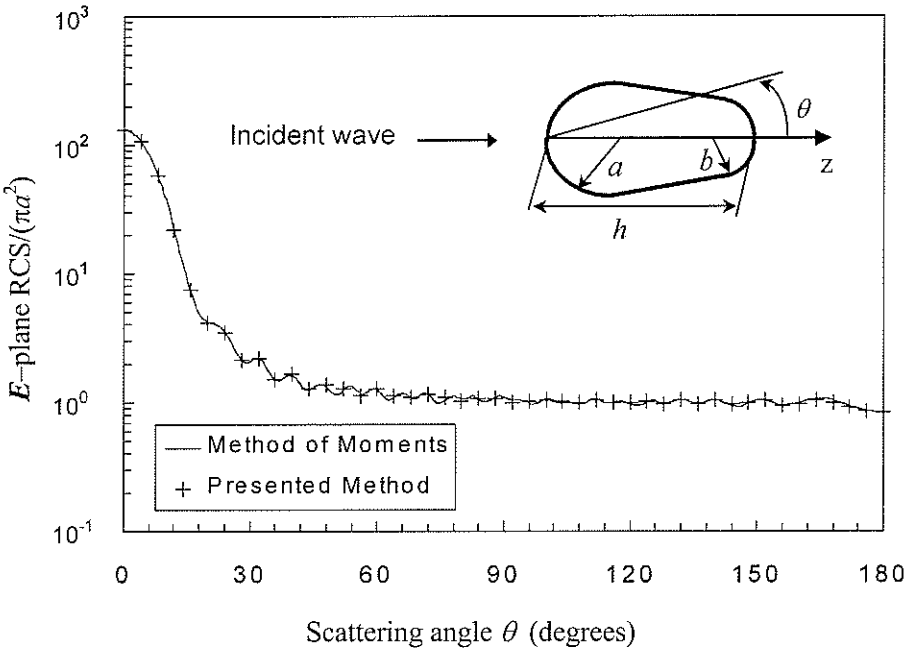

Fig. 5.6. $\boldsymbol{E}$ – plane RCS for a conducting cone with spherical caps, $\beta_0 a = 12$, $\beta_0 b = 6$, and $\beta_0 h = 48$, for N = 512 basis functions along the generator curve and a sparsity $S = 92.36\%$ of the matrix $\boldsymbol{Z}'$ after thresholding.

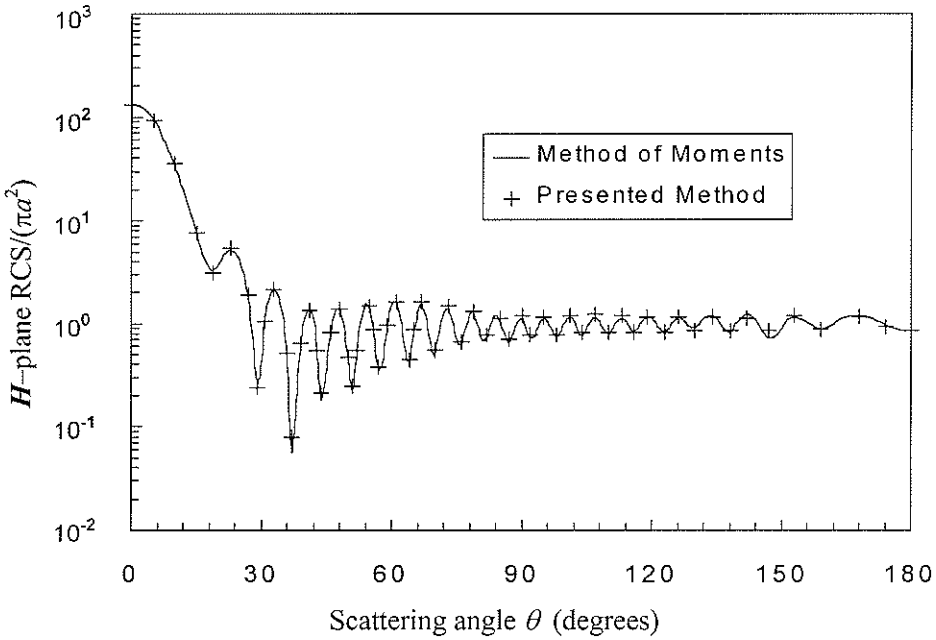

Fig. 5.7. $\boldsymbol{H}$ – plane RCS for the conducting cone with spherical caps in Fig. 5.6 for a sparsity $S = 92.36\%$ of the matrix $\boldsymbol{Z}'$ after thresholding.

TABLE 5.2. EFFICIENCY FOR CONDUCTING CONES WITH SPHERICAL CAPS.

N	Matrix Size	Threshold Value δ	Sparsity S (%)	CPU Time in Seconds		Reduction in CPU Time (%)
				FWT + GMRES	LU	
256	512×512	2×10^{-4}	88.47	22.41 + 21.53	86.01	48.92
512	1024×1024	2.1×10^{-6}	92.36	91.83 + 73.71	761.41	78.29

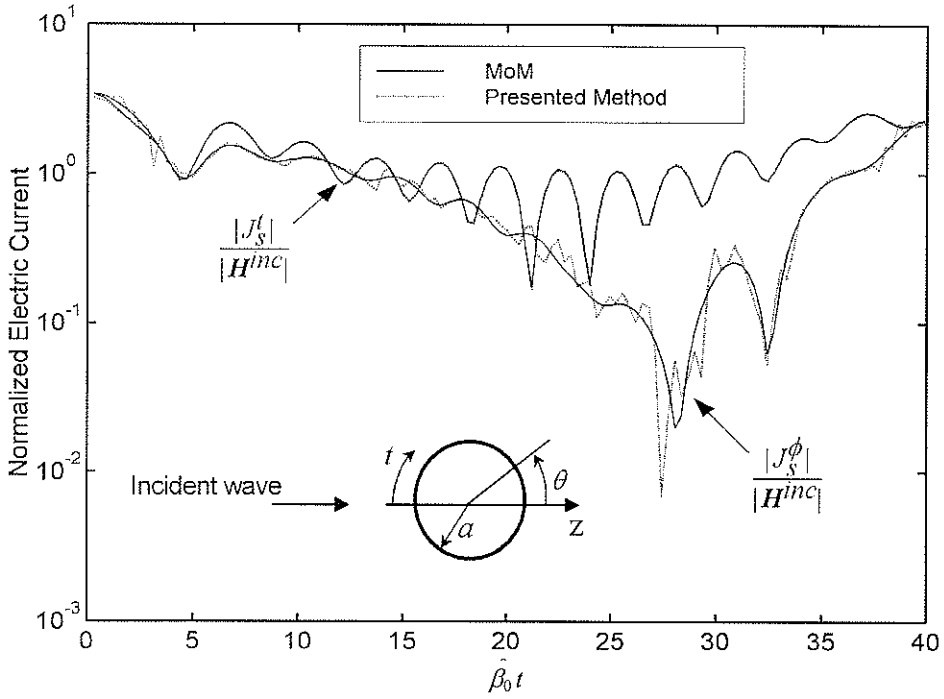

Fig. 5.8. Electric current density on a dielectric sphere of electric radius $\beta_0 a = 12.8$ and relative dielectric constant $\varepsilon_r = 8$, for $N = 128$ basis functions along the generator curve.

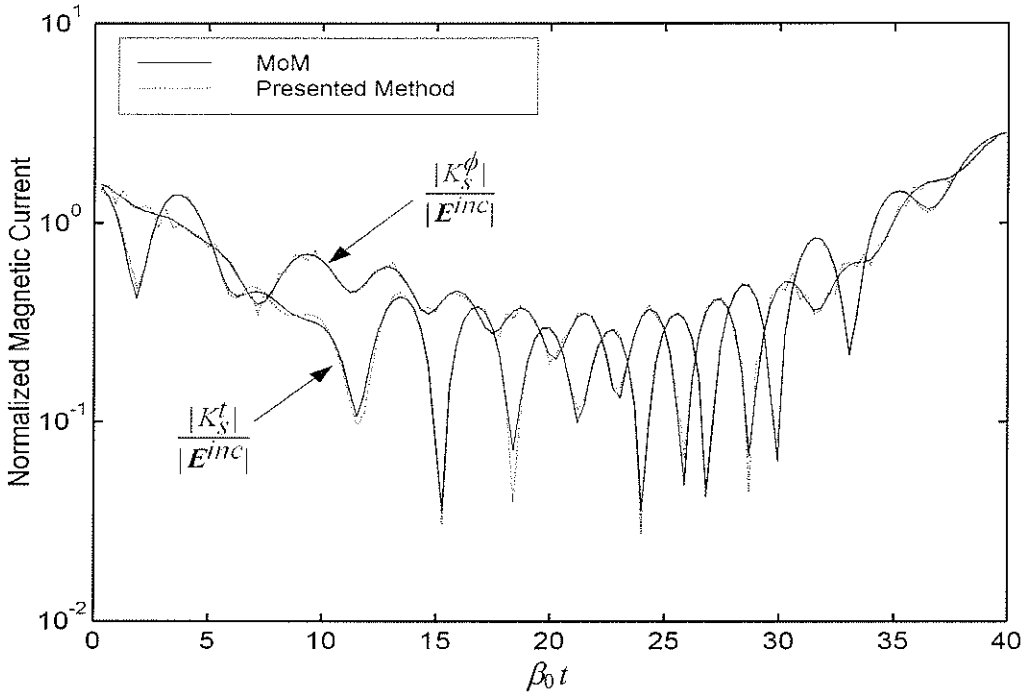

Fig. 5.9. Magnetic current density on the dielectric sphere in Fig. 5.8.

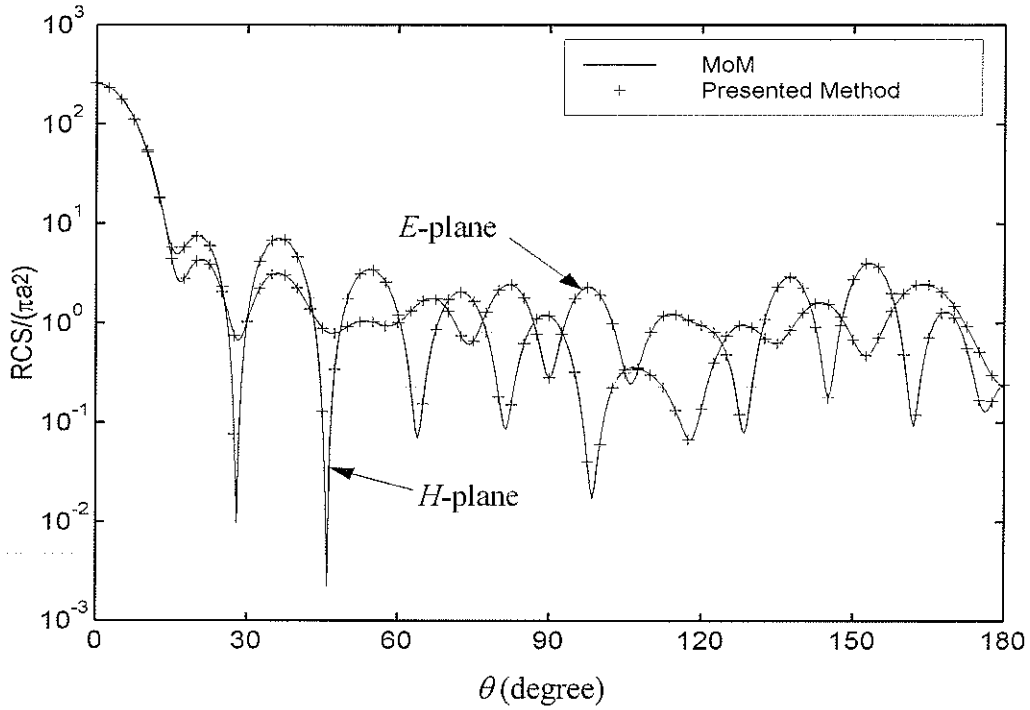

Fig. 5.10. Far-field RCS of the dielectric sphere in Fig. 5.8.

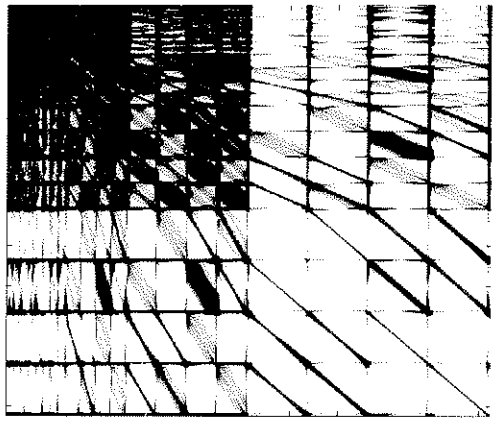

Fig. 5.11. Structure of the matrix with a sparsity $S = 66.58\%$ obtained after thresholding $\boldsymbol{Z}'$ for the dielectric sphere in Fig. 5.8.

TABLE 5.3. EFFICIENCY FOR DIELECTRIC SPHERES WITH $\varepsilon_r = 8$ AND RADIUS a.

$\beta_0 a$	N	Matrix Size	Sparsity S (%)	Reduction in CPU Time (%)
12.8	128	512 × 512	66.58	50.14
25.6	256	1024 × 1024	76.58	71.08
51.2	512	2048 × 2048	78.64	73.14

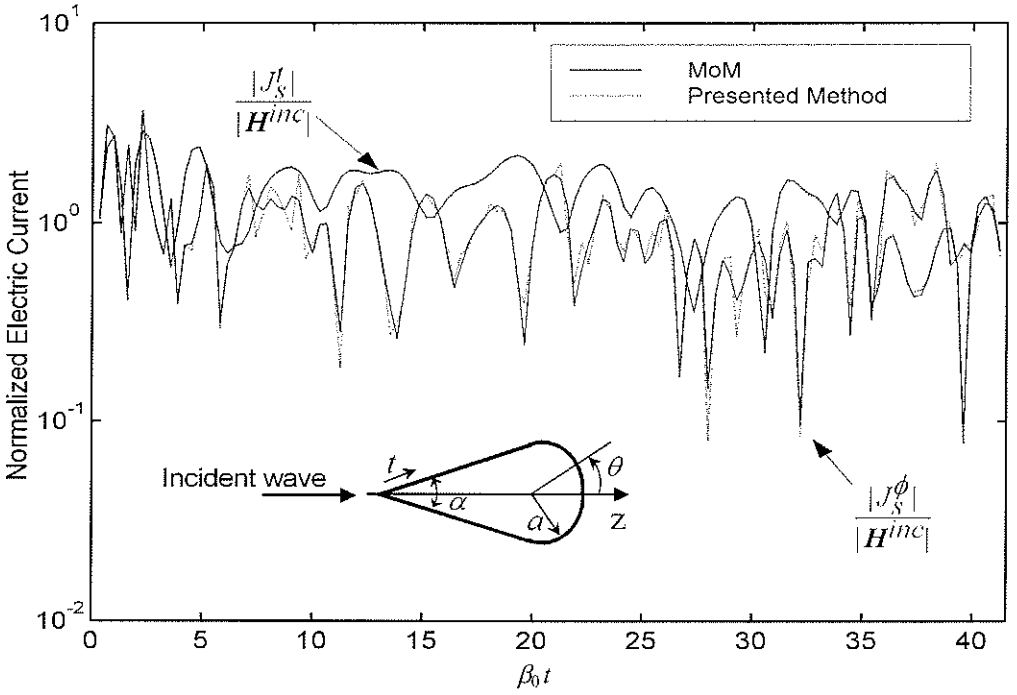

Fig. 5.12. Electric current density on a cone-sphere scatterer with $\varepsilon_r = 12$, $\alpha = 50^\circ$ and $\beta_0 a = 10$, for $N = 128$ basis functions along the generator curve.

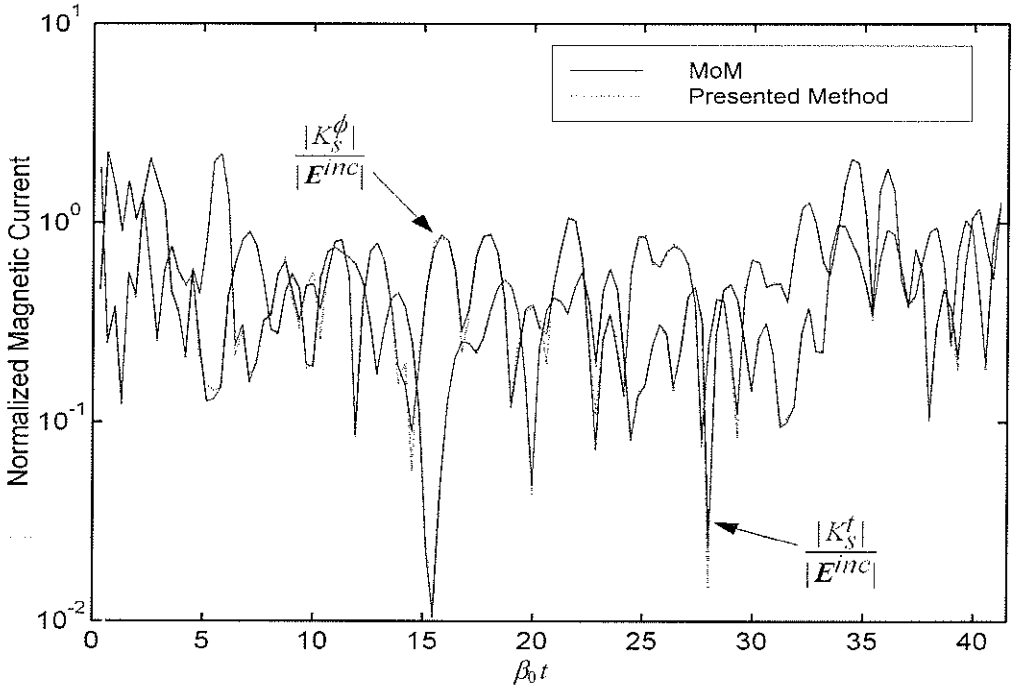

Fig. 5.13. Magnetic current density on the dielectric cone-sphere in Fig. 5.12.

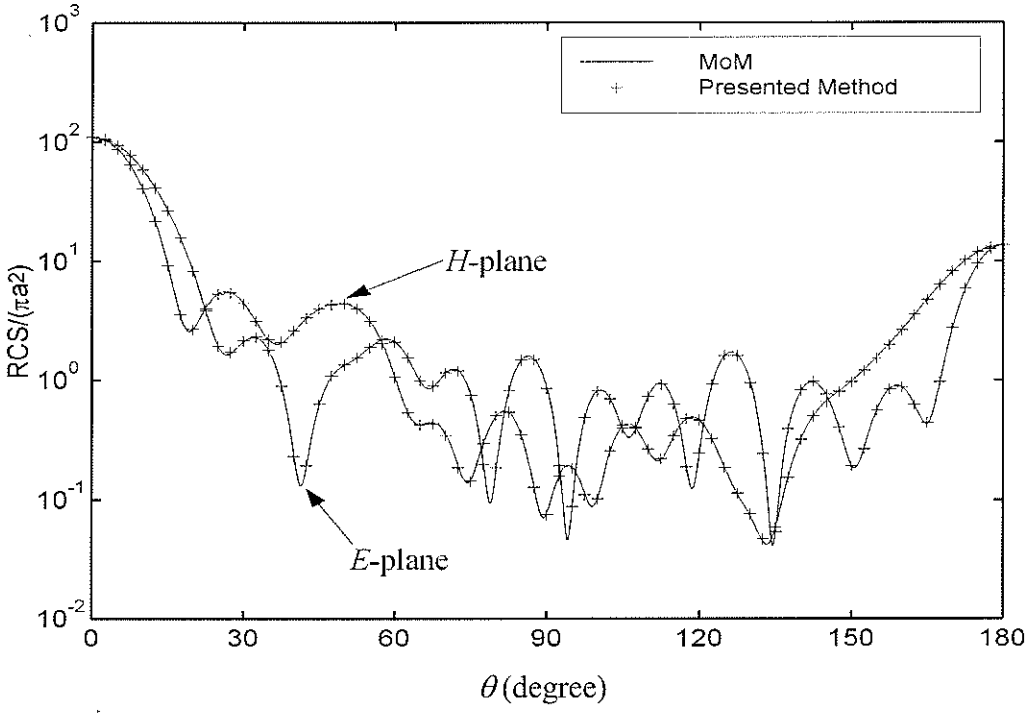

Fig. 5.14. Far-field RCS of the dielectric cone-sphere in Fig. 5.12.

TABLE 5.4. EFFICIENCY FOR DIELECTRIC CONE-SPHERES WITH $\varepsilon_r = 12$, $\alpha = 50^\circ$ AND RADIUS a.

$\beta_0 a$	N	Matrix Size	Sparsity S (%)	Reduction in CPU Time (%)
10	128	512 × 512	55.20	41.37
20	256	1024 × 1024	70.35	60.21
40	512	2048 × 2048	74.45	67.33

Chapter 6

SCATTERING BY 3-D INHOMOGENEOUS DIELECTRIC BODIES

§6.1. Introduction

The use of wavelets in the MoM results in highly sparse matrix equations, which can be solved efficiently by utilizing sparse matrix solvers. In [45], the computational complexity was studied when orthogonal wavelets, along with a sparse conjugate gradient solver, are employed for the solution of 2-D electromagnetic scattering problems. A sparse generalized minimal residual method and the MTA with orthogonal wavelets has been successfully applied to obtain fast solutions for the electromagnetic scattering by conducting bodies of revolution [81] and a sparse LU solver with the approximate minimum degree ordering algorithm and the MTA with orthogonal wavelets have also been proposed for the fast analysis of the electromagnetic scattering by dielectric bodies of revolution [82].

In this Chapter, a fast wavelet analysis method for the problem of wave scattering by 3-D inhomogeneous dielectric bodies of arbitrary geometry is presented. The fields scattered by such objects are modeled using a volume integral equation involving equivalent sources. The application of the MoM leads to matrix equations with a Toeplitz-block structure [48], [58], which is fully exploited to speed up the 3-D wavelet transform algorithm. Then, a sparse bi-conjugate gradient (BiCG) solver is employed to achieve a fast solution of the resultant systems of equations with a computation cost of $O(M)$, where M is the total number of unknowns. Numerical experiments are presented to show the efficiency of this procedure for lossless and also for lossy dielectric bodies with different geometric shapes.

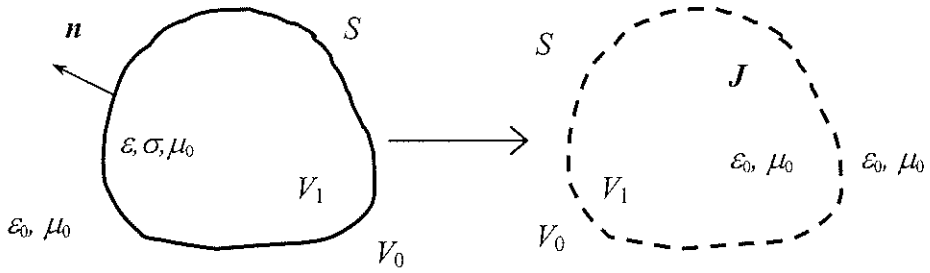

Fig. 6.1. Replacement of a lossy, inhomogeneous dielectric body by an equivalent volume current.

§6.2. Problem Formulation

Consider a lossy, inhomogeneous 3-D dielectric body V_1, enclosed by a surface S, of arbitrary shape, with the permittivity $\varepsilon(\boldsymbol{r})$ and conductivity $\sigma(\boldsymbol{r})$, located in free space V_0 as shown in Fig. 6.1(a). The body is replaced by a distribution of equivalent volume current density $\boldsymbol{J}$ as shown in Fig. 6.1(b), with

$$\boldsymbol{J}(\boldsymbol{r}) = \{\sigma(\boldsymbol{r}) + j\omega[\varepsilon(\boldsymbol{r}) - \varepsilon_0]\boldsymbol{E}(\boldsymbol{r})\} \equiv \tau(\boldsymbol{r})\boldsymbol{E}(\boldsymbol{r}) \tag{6.1}$$

where ε_0 is the free-space permittivity and $\boldsymbol{E}(\boldsymbol{r})$ is the total electric field intensity inside the body. The distribution of $\boldsymbol{J}$ is related to the scattered field at the observation point of position vector $\boldsymbol{r}$ through the integral equation,

$$\boldsymbol{E}^s(\boldsymbol{r}) = \int_{V_1} \overline{\boldsymbol{G}}(\boldsymbol{r},\boldsymbol{r}') \cdot \boldsymbol{J}(\boldsymbol{r}')dv' \tag{6.2}$$

where $\boldsymbol{r}'$ is the position vector of the source point and $\overline{\boldsymbol{G}}(\boldsymbol{r},\boldsymbol{r}')$ is the free-space dyadic Green function

$$\begin{cases} \overline{\boldsymbol{G}}(\boldsymbol{r},\boldsymbol{r}') = -j\omega\mu_0\left[\bar{\boldsymbol{I}} + \dfrac{\nabla\nabla}{k_0^2}\right] G(\boldsymbol{r},\boldsymbol{r}') \\ G(\boldsymbol{r},\boldsymbol{r}') = \dfrac{e^{-jk_0|\boldsymbol{r}-\boldsymbol{r}'|}}{4\pi|\boldsymbol{r}-\boldsymbol{r}'|} \end{cases} \tag{6.3}$$

μ_0 being the permeability of free space, $k_0 = \omega\sqrt{\varepsilon_0\mu_0}$ the wave number in free space, and $\bar{\boldsymbol{I}}$ the identity dyadic, i.e. $\bar{\boldsymbol{I}} = \boldsymbol{xx} + \boldsymbol{yy} + \boldsymbol{zz}$ in Cartesian coordinates.

Since the total electric field $\boldsymbol{E}(\boldsymbol{r})$ inside the body is the sum of the scattered field $\boldsymbol{E}^s(\boldsymbol{r})$ and the incident field $\boldsymbol{E}^{inc}(\boldsymbol{r})$, i.e.,

$$\boldsymbol{E}(\boldsymbol{r}) = \boldsymbol{E}^s(\boldsymbol{r}) + \boldsymbol{E}^{inc}(\boldsymbol{r}). \tag{6.4}$$

An integral equation satisfied by $\boldsymbol{J}$ can be written in the form

$$\frac{1}{\tau(\boldsymbol{r})}\boldsymbol{J}(\boldsymbol{r}) - \mathcal{L}(\boldsymbol{J}(\boldsymbol{r})) = \boldsymbol{E}^{inc}(\boldsymbol{r}) \tag{6.5}$$

where

$$\mathcal{L}(\boldsymbol{J}(\boldsymbol{r})) = \int_{V_1} \overline{\boldsymbol{G}}(\boldsymbol{r},\boldsymbol{r}') \cdot \boldsymbol{J}(\boldsymbol{r}')dv \tag{6.6}$$

Since $\mathcal{L}$ is a linear operator, the MoM can be applied to solve (6.5). Once $\boldsymbol{J}$ is found, $\boldsymbol{E}$ can be determined everywhere via (6.2)–(6.4).

§6.3. Numerical Method

In rectangular coordinates, $\overline{\boldsymbol{G}}(\boldsymbol{r},\boldsymbol{r}')\cdot\boldsymbol{J}(\boldsymbol{r}')$ in (6.6) can be expressed as

$$\overline{\boldsymbol{G}}\cdot\boldsymbol{J}=\begin{bmatrix} G_{11} & G_{12} & G_{13} \\ G_{21} & G_{22} & G_{23} \\ G_{31} & G_{32} & G_{33} \end{bmatrix}\begin{bmatrix} \boldsymbol{u}_1\cdot\boldsymbol{J} \\ \boldsymbol{u}_2\cdot\boldsymbol{J} \\ \boldsymbol{u}_3\cdot\boldsymbol{J} \end{bmatrix} \tag{6.7}$$

where $\boldsymbol{u}_p$, $p=1, 2, 3$ denotes a unit vector along $x-$, $y-$ or $z-$axis, respectively, and G_{pq} is given by

$$G_{pq}(\boldsymbol{r},\boldsymbol{r}')=-j\omega\mu_0\left(\delta_{pq}+\frac{1}{k_0^2}\frac{\partial^2}{\partial u_p\,\partial u_q}\right)G(\boldsymbol{r},\boldsymbol{r}'),\quad p,q=1,2,3 \tag{6.8}$$

with δ_{pq} being the Kronecker delta and G the scalar Green's function given in (6.3).

Equation (6.5) can be cast into a matrix equation through the MoM discussed in Chapter 2. Firstly, the unknown current density is expanded in terms of a set of subdomain basis functions $\{f_n^p(\boldsymbol{r});\, n\in[1,N],\, p\in[1,3]\}$, i.e.,

$$\boldsymbol{J}(\boldsymbol{r})=\sum_{n=1}^{N}\sum_{p=1}^{3}\boldsymbol{u}_p a_n^p f_n^p(\boldsymbol{r}),\qquad \boldsymbol{r}\in V_1 \tag{6.9}$$

Substituting (6.7) and (6.9) into (6.5) gives

$$\frac{1}{\tau(\boldsymbol{r})}\sum_{n=1}^{N}a_n^p f_n^p-\sum_{n=1}^{N}\sum_{q=1}^{3}a_n^q\langle G_{pq},f_n^q\rangle=\boldsymbol{u}_p\cdot\boldsymbol{E}^{inc}(\boldsymbol{r}),\quad p=1,2,3 \tag{6.10}$$

where $\langle\cdot\rangle$ indicates the inner product.

Consequently, after applying a weighted residual method with a set of weighting functions $\{\boldsymbol{w}_m(\boldsymbol{r}), m \in [1, N]\}$, where

$$\boldsymbol{w}_m(\boldsymbol{r}) = \sum_{p=1}^{3} \boldsymbol{u}_p w_m^p(\boldsymbol{r}) \tag{6.11}$$

we have

$$\sum_{n=1}^{N} a_n^p \langle w_m^p, \frac{1}{\tau(\boldsymbol{r})} f_n^p \rangle - \sum_{n=1}^{N}\sum_{q=1}^{3} a_n^q \langle w_m^p, \langle G_{pq}, f_n^q \rangle\rangle = \langle w_m^p, \boldsymbol{u}_p \cdot \boldsymbol{E}^{inc}(\boldsymbol{r})\rangle, \quad p = 1, 2, 3 \tag{6.12}$$

which can be written as a matrix equation of the form

$$\begin{bmatrix} \boldsymbol{Z}_{11} + \boldsymbol{D}_1 & \boldsymbol{Z}_{12} & \boldsymbol{Z}_{13} \\ \boldsymbol{Z}_{21} & \boldsymbol{Z}_{22} + \boldsymbol{D}_2 & \boldsymbol{Z}_{23} \\ \boldsymbol{Z}_{31} & \boldsymbol{Z}_{32} & \boldsymbol{Z}_{33} + \boldsymbol{D}_3 \end{bmatrix} \begin{bmatrix} \boldsymbol{I}_1 \\ \boldsymbol{I}_2 \\ \boldsymbol{I}_3 \end{bmatrix} = \begin{bmatrix} \boldsymbol{V}_1 \\ \boldsymbol{V}_2 \\ \boldsymbol{V}_3 \end{bmatrix} \tag{6.13}$$

or, more condensed, as $\boldsymbol{ZI} = \boldsymbol{V}$, with the elements of $\boldsymbol{I}_p$, $\boldsymbol{V}_p$, $\boldsymbol{D}_p$ and $\boldsymbol{Z}_{pq}$ given by

$$\begin{cases} [I_p]_m = a_m^p \\ [V_p]_m = \langle w_m^p(\boldsymbol{r}),\ \boldsymbol{u}_p \cdot \boldsymbol{E}^{inc}(\boldsymbol{r})\rangle \\ [D_p]_{mn} = \langle w_m^p(\boldsymbol{r}),\ \dfrac{1}{\tau(\boldsymbol{r})} f_n^p(\boldsymbol{r})\rangle \\ [Z_{pq}]_{mn} = -\langle w_m^p(\boldsymbol{r}),\ \langle G_{pq}, f_n^q(\boldsymbol{r})\rangle\rangle, \quad p, q = 1, 2, 3 \end{cases} \tag{6.14}$$

Here, $\boldsymbol{Z}_{pq}$ are Toeplitz matrices, $\boldsymbol{D}_p$ are banded matrices, and $\boldsymbol{Z}$ is symmetric.

A Galerkin's moment method with rooftop basis functions [48] has been implemented, where the elements in (6.14) are evaluated numerically, as well as a simple point-matching moment method [11], [16], where the elements in (6.14) are calculated analytically.

Equation (6.14) can be transformed into (2.24) using CBS with a 3-D wavelet transform matrix $\boldsymbol{W}$. The transformed matrix $\boldsymbol{Z}'$ is highly sparse after thresholding and, thus, a sparse iterative method such as the BiCG can be employed to achieve a fast solution of the resultant systems of equations with a computational cost of $O(M)$, where $M = 3N$, N being the number of basis functions used.

The conventional fast wavelet transform described in Appendix A for (2.25), and also in [24], requires a number of arithmetic operations of $O(M^2)$. However, it is noted that the submatrices $\boldsymbol{Z}_{pq}$ in (6.13) are Toeplitz matrices and $\boldsymbol{Z}$ is symmetric. Thus, a wavelet transform algorithm designed for Toeplitz matrices [73], [83] is utilized which significantly reduces the number of arithmetic operations by eliminating redundant operations in the wavelet transforms applied to column and row vectors of a Toeplitz matrix. The number of arithmetic operations necessary to perform this wavelet transform to (6.13), with 8 vanishing moments, is plotted as a function of the N in Fig. 6.2, which shows its efficiency with respect to the conventional FWT algorithm.

§6.4. Numerical Experiments

A computer program has been written with dynamic memory allocation, to implement the above mentioned technique. The MoM in [11], [16] is used to obtain the matrix equation (6.13), and Daubechies' wavelets with 8 vanishing moments are used to obtain the transformed matrix equation of the form (2.24). The sparsity S of a matrix is defined here as

its percentage content of zero elements, and the effect of the threshold is measured by the error function defined as

$$E_{err} = \frac{\| \boldsymbol{E} - \boldsymbol{E}_{\delta} \|}{\| \boldsymbol{E} \|} \times 100(\%) \tag{6.15}$$

where $\boldsymbol{E}$ is the total electric field intensity inside the scatterer obtained by directly solving (6.13) and $\boldsymbol{E}_{\delta}$ is the value obtained from the transformed equation (2.24) with a threshold value δ. The termination criterion for the sparse BiCG algorithm is chosen in terms of the relative residual error, namely $\| \boldsymbol{Z}'\boldsymbol{I}' - \boldsymbol{V}' \| / \| \boldsymbol{V}' \| < 10^{-4}$. To measure the performance of the presented method, the reduction in computational time is defined as

$$\eta_{\alpha} = \frac{T_{\alpha} - T}{T_{\alpha}} \times 100(\%), \quad \alpha = \text{LU, BiCG} \tag{6.16}$$

where T_{α} is the CPU time used to solve (6.13) by the standard α solver with α being either LU or BiCG, and T is the CPU time used by the presented method including the time used to perform the wavelet transform of (6.13). Further, η_{LU} represents the reduction in CPU time of the presented algorithm with respect to the standard LU solver, while η_{BiCG} is that with respect to the standard BiCG solver, and thus the latter is a quantitative measure of the contribution of using wavelets. Numerical experiments are conducted on a Pentium 800MHz personal computer.

The first illustrative example considered is that of a homogenous dielectric sphere with the electric radius $ka = 1.0$ and a relative permittivity $\varepsilon_r = 4.0$, as shown in Fig. 6.3. The incident wave is propagating in the $z-$direction and is polarized in the $x-$direction. The

geometry is modeled by using $8\times8\times8$ cubic cells of equal size. When S = 90.05%, the sparse structure of $\boldsymbol{Z}'$ is shown in Fig. 6.4, and the far-field RCS is plotted in Fig. 6.3, where the solution obtained when S = 0% and the Mie series solution are given as reference. The performance of the presented algorithm is shown in Table 6.1, where a reduction of $\eta_{LU} \approx 96\%$ can be observed, while η_{BiCG} is about 17~26%. In other words, the presented method is faster than the conventional MoM using standard LU solver about 25 times, and than that using the standard BiCG solver about 1.3 times. This is due to the fact that the problem considered is well conditioned such that the BiCG solver converges rapidly to a relative residual 10^{-4} within 15 iterations.

A second example is that of inhomogeneous dielectric block in the form of a rectangular parallelepiped of electric size $ka = 0.5$, $kb = 0.5$, and $kc = 1.0$, with the relative permittivity distributed as $\varepsilon_r(x) = \varepsilon_{r,\min} + (\Delta\varepsilon/2a)(x + a - \Delta x/2)$, where $\varepsilon_{r,\min} = 2.5$, $\Delta\varepsilon = 1.0$, and Δx is the cell width in the $x-$direction, $\Delta x = a/4$, as shown in Fig. 6.3. The geometry is modeled by using $8\times8\times16$ cubic cells of equal size. When S = 86.31%, the sparse structure of $\boldsymbol{Z}'$ is shown in Fig. 6.4, and the far-field RCS is plotted in Fig. 6.3, where the result obtained without thresholding, i.e., S = 0%, is also plotted as a reference. The performance of this algorithm is indicated in Table 6.2, which shows that the CPU time reductions are about $\eta_{LU} \approx 78\%$ and $\eta_{BiCG} \approx 53 \sim 63\%$. It should be remarked that the computational efficiency increases with the matrix size, which recommends the method presented for an efficient solution of electrically large problems.

A third example considered is that of a lossy dielectric block in the form of a rectangular parallelepiped of electric size $ka = 1.0$, $kb = 0.5$, and $kc = 0.5$, with

$\varepsilon_r = 7.45$ and $\sigma = 0.889 S/m$, illuminated by an incident wave propagating in the $z-$direction with $x-$polarization, as shown in Fig. 6.8. The geometry is modeled by using $16 \times 8 \times 8$ cubic cells of equal size. When $S = 73.81\%$, the sparse structure of $\boldsymbol{Z}'$ is shown in Fig. 6.9, and the far-field RCS is plotted in Fig. 6.10, where the result obtained without thresholding, i.e., $S = 0\%$, is also plotted as a reference. The performance of this algorithm is indicated in Table 6.3. An efficiency of $\eta_{\mathrm{LU}} \approx \eta_{\mathrm{BiCG}} = 67 \sim 78\%$ is achieved in this case. Note that η_{LU} is decreased and η_{BiCG} is increased in comparison with the previous cases. This is mainly due to the larger magnitude of $\tau(\boldsymbol{r})/j\omega\varepsilon_0 = \varepsilon_r + \sigma / j\omega\varepsilon_0 - 1$ in (6.1), which makes the values of the elements of the submatrices $\boldsymbol{D}_p$ in (6.14) smaller, and worsens the condition number of the global matrix $\boldsymbol{Z}$ and thus increases the number of iterations of the BiCG solver.

§6.5. Conclusions

The application of wavelet transform to the problem of wave scattering by 3-D inhomogeneous dielectric bodies of arbitrary geometry is investigated in this chapter. The fields scattered by such dielectric objects are modeled using a volume integral equation with equivalent sources, whose corresponding MoM matrix equation has a Toeplitz-block structure, which is fully exploited to speed up the 3-D wavelet transform utilizing the efficient algorithm designed for Toeplitz matrices in [73]. A highly sparse matrix equation is derived after applying the wavelet transform, whose solution can be obtained by using an efficient sparse BiCG algorithm. Numerical experiments are conducted for lossless homogenous dielectric spheres with relatively small permittivity which is well conditioned, lossless inhomogeneous parallelepipeds of electrically large size, and lossy

homogenous dielectric parallelepipeds whose MoM matrices have a larger condition number. It has been shown that the method presented gives an efficient fast solution technique for the analysis of wave scattering by 3-D inhomogeneous dielectric bodies of arbitrary geometry.

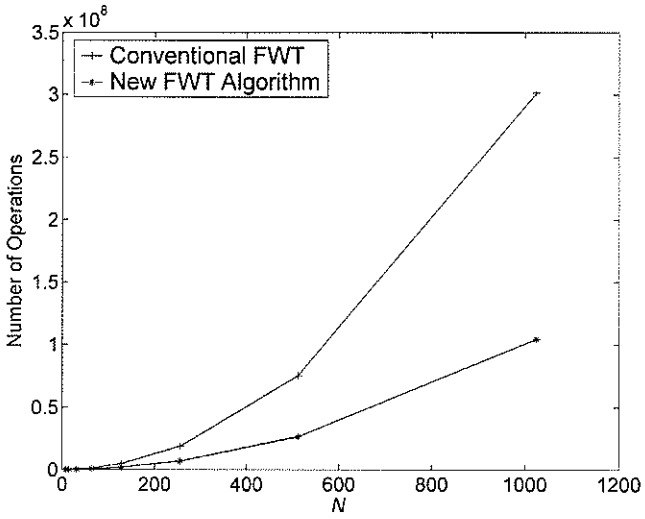

Fig. 6.2. Number of arithmetic operations used to perform the wavelet transform with 8 vanishing moments for the matrix $\boldsymbol{Z}$ in (6.14) as a function N, where $3N$ is the number of unknowns.

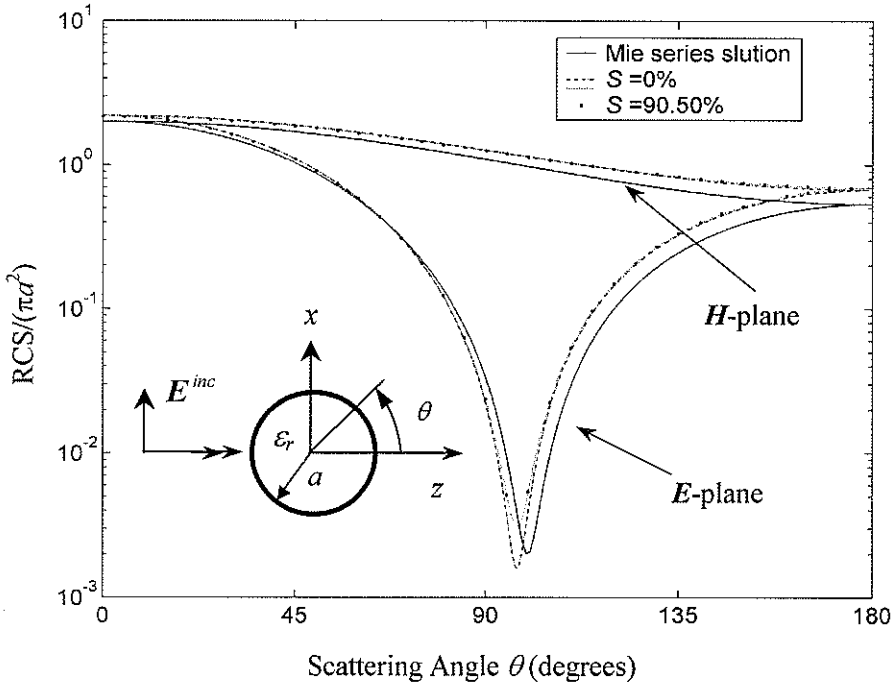

Fig. 6.3. Far-field RCS of a homogenous dielectric sphere of radius $ka = 1.0$ and relative permittivity $\varepsilon_r = 4.0$.

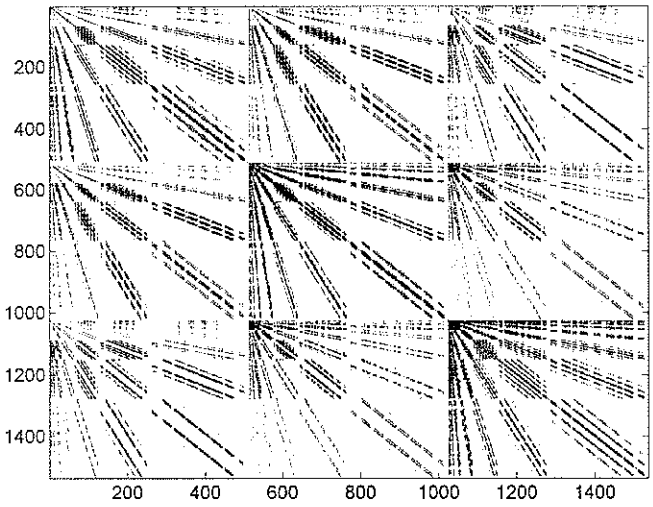

Fig. 6.4. Gray-scaled image of the sparse matrix with S = 90.05% for the spherical scatterer in Fig. 6.3.

TABLE 6.1. COMPUTATION EFFICIENCY FOR THE SPHERE IN FIG. 6.3; η_α IS DEFINED IN (6.16).

δ	S(%)	E_{err}(%)	CPU time (s)	η_α (%)	
			FWT + BiCG	α = LU	α = BiCG
2×10^{-3}	73.77	1.31	7.75 + 3.41	95.85	17.03
5×10^{-3}	84.42	2.44	7.75 + 2.66	96.13	22.60
8×10^{-3}	88.72	3.40	7.75 + 2.25	96.28	25.65
1×10^{-2}	90.50	4.36	7.75 + 2.09	96.34	26.84

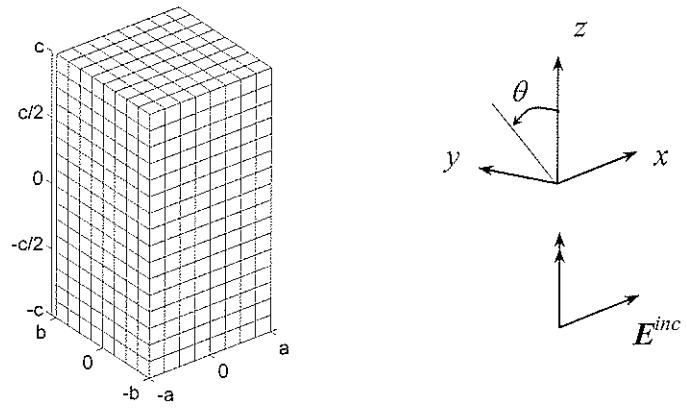

Fig. 6.5. Inhomogeneous rectangular block scatterer of size $ka = 0.5$, $kb = 0.5$, and $kc = 1.0$, with $\varepsilon_r(x) = \varepsilon_{r,\min} + (\Delta\varepsilon/2a)(x + a - \Delta x/2)$, where $\varepsilon_{r,\min} = 2.5$, $\Delta\varepsilon = 1.0$, and $\Delta x = a/4$.

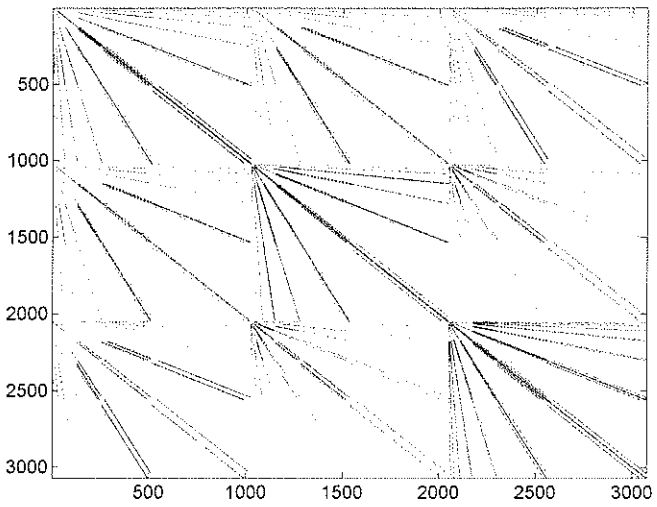

Fig. 6.6. Gray-scaled image of the sparse matrix with $S = 86.31\%$ for the inhomogeneous rectangular block scatterer in Fig. 6.5.

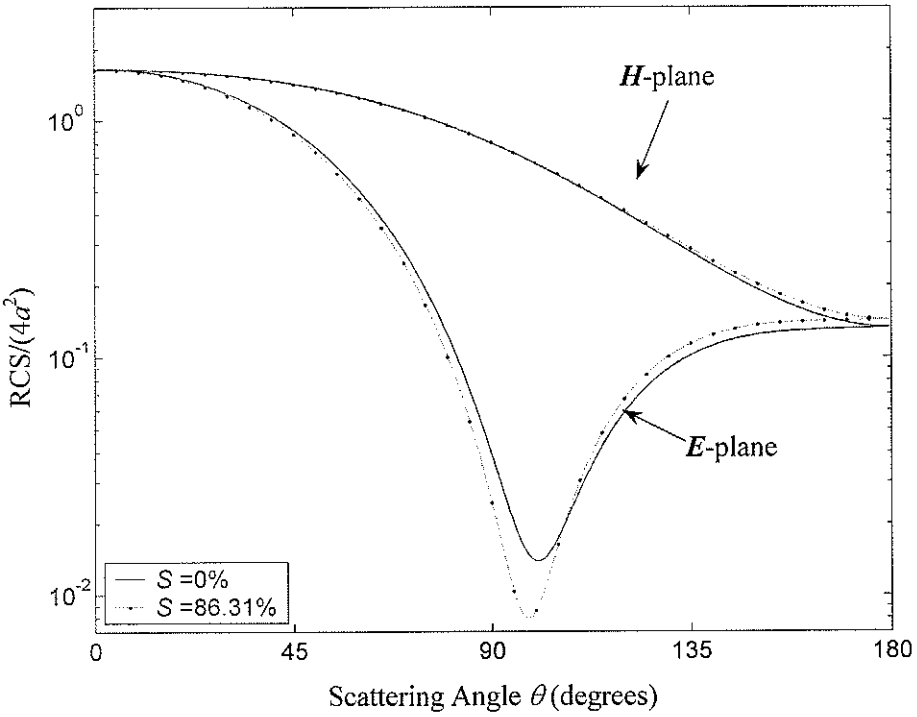

Fig. 6.7. Far-field RCS of the inhomogeneous rectangular block scatterer in Fig. 6.5.

TABLE 6.2. COMPUTATION EFFICIENCY FOR THE INHOMOGENEOUS RECTANGULAR BLOCK IN FIG. 6.5; η_α IS DEFINED IN (6.16).

δ	S(%)	E_{err}(%)	CPU time (s)	η_α (%)	
			FWT + BiCG	α = LU	α = BiCG
1×10^{-3}	71.66	0.58	23.86 + 21.85	97.94	53.06
3×10^{-3}	82.01	1.31	23.86 + 17.81	98.12	57.21
5×10^{-3}	86.31	1.74	23.86 + 13.22	98.33	61.92
8×10^{-3}	89.53	2.43	23.86 + 11.78	98.39	63.40

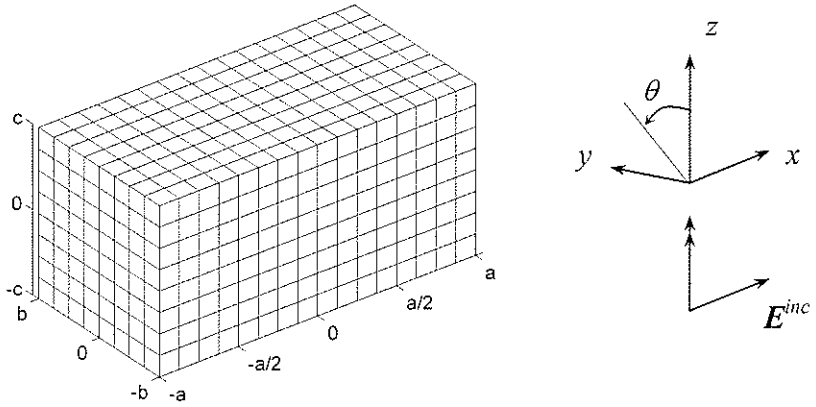

Fig. 6.8. Lossy rectangular block scatterer of size $ka = 1.0$, $kb = 0.5$, and $kc = 0.5$, with $\varepsilon_r = 7.45$ and $\sigma = 0.889$ S/m.

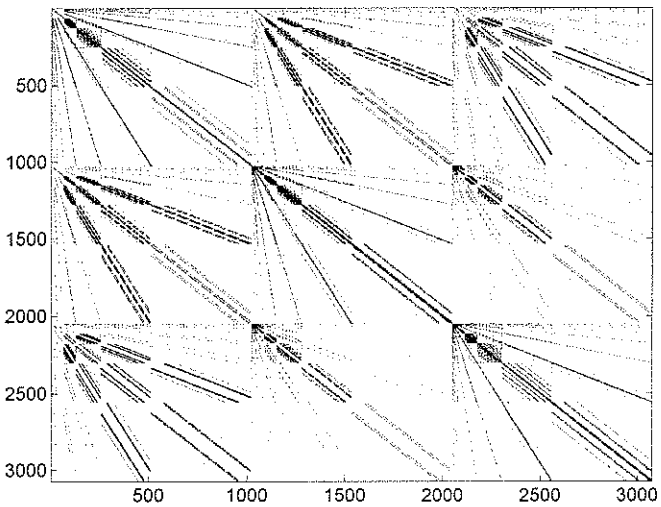

Fig. 6.9. Gray-scaled image of the sparse matrix with $S = 73.81\%$ for the lossy rectangular block scatterer in Fig. 6.8.

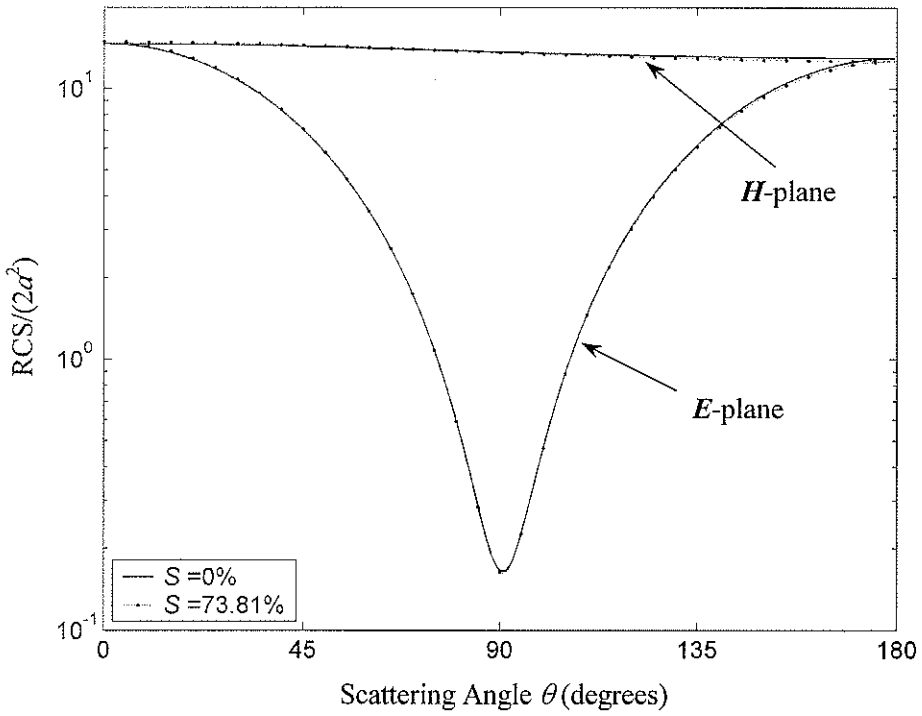

Fig. 6.10. Far-field RCS of the lossy rectangular block scatterer in Fig. 6.8.

TABLE 6.3. COMPUTATION EFFICIENCY FOR THE LOSSY RECTANGULAR BLOCK IN FIG. 6.8; η_α IS DEFINED IN (6.16).

δ	S(%)	E_{err}(%)	CPU time (s)	η_α (%)	
			FWT + BiCG	α = LU	α = BiCG
3×10^{-2}	61.40	2.55	23.86 + 700.44	67.33	67.20
5×10^{-2}	67.92	4.68	23.86 + 573.61	73.05	72.95
8×10^{-2}	73.81	8.89	23.86 + 454.21	78.44	78.35

Chapter 7

CONCLUSIONS AND FUTURE WORK

§7.1. Conclusions

In this work, the application of wavelets for a fast solution of electromagnetic integral equations is studied. Wavelets offer the advantages of highly sparse moment-method matrices, as well as a natural mechanism for a multilevel analysis, and thus are a powerful mathematical tool for the numerical solution of integral equations.

Orthogonal wavelets provide a unitary transformation and are the optimal category of wavelets in terms of the matrix condition number when used for the solution of electromagnetic integral equations. More highly sparse moment-method matrices can be obtained at the cost of worsening the matrix condition number with the use of semi-orthogonal wavelets. The condition number of the matrices in the semi-orthogonal wavelet domain is higher than that of the moment-method matrices, about $10^2 \sim 10^4$ times higher for the case of 8 vanishing moments, for example. The optimal number of vanishing moments in a family of wavelets is 8, when the total number of unknowns is less than 5000.

Two applications of orthogonal wavelets, the MTA and the CBS, produce highly sparse moment-method matrices and both are efficient means for a fast solution of electromagnetic integral equations. The CBS gives rise to more sparse matrices than the MTA, about 7% more for the problems of scattering by two-dimensional dielectric bodies considered in the

work. The MTA, however, simply requires one-dimensional wavelets, and provides a problem-independent transformation.

The MTA with orthogonal wavelets has been efficiently extended to the analysis of scattering by BORs, which is performed by constructing coupled vector integro-differential equations by taking advantage of the axial symmetry of the body. Efficient solution techniques for solving the resultant sparse matrix equations have also been proposed. The presented solution technique using GMRES is an efficient means for sparse matrix equations, which is demonstrated for the analysis of conducing BORs. A sparse LU solver with the approximate minimum degree-ordering algorithm [56] can be advantageously applied to the solution of matrix equations that possess a higher condition number, when iterative methods like the CG and GMRES fail to converge, e.g., for the analysis of dielectric BORs.

Finally, the application of wavelets is further extended to the analysis of scattering by 3-D inhomogeneous bodies of arbitrary geometry formulated as a volume integral equation involving equivalent sources [83]. An efficient wavelet transform algorithm designed for Toeplitz matrices [73] is employed to speed up the 3-D wavelet transformations, and a sparse BiCG algorithm is implemented to obtain a fast solution of the resultant sparse matrix equation. Numerical experiments conducted have shown that the presented procedure is highly efficient.

The main contributions of this work are now summarized as follows:

- The performance of semi-orthogonal and orthogonal wavelets, when used for a fast solution of integral equations, has been studied systematically, and it has

been pointed out for the first time that the orthogonal wavelets are optimal in terms of the matrix condition number.

- The MTA and the CBS have been implemented for the solution of coupled scalar integral equations and have been efficiently used for the analysis of scattering by two-dimensional dielectric bodies.

- The use of wavelets has been extended to solving single vector integro-differential equations that arise in the analysis of scattering by conducting BORs, as well as to coupled vector integro-differential equations formulated for the analysis of scattering by dielectric BORs.

- The application of wavelets has been successfully implemented for the analysis of scattering by 3-D inhomogeneous bodies of arbitrary geometry, which is formulated as a volume integral equation. An efficient wavelet transform algorithm for Toeplitz matrices is utilized and a sparse BiCG solver is employed to obtain a fast solution of the resultant sparse matrix equations.

- Several solution techniques for sparse matrices, obtained with the use of wavelets, have been investigated. A sparse CG solver is efficiently used for a fast solution of Fredholm integral equations. A sparse BiCG algorithm with an efficient wavelet transform technique for Toeplitz matrices is also presented for the fast solution of 3-dimensional volume integral equations associated with scattering problems by 3-dimenaional inhomogeneous bodies. Also, two solution techniques have been proposed for the analysis of scattering by bodies of revolution. The one using a sparse GMRES has been demonstrated for the analysis of scattering by conducting bodies of revolution. The other one, using a

sparse LU solver with an approximate minimum degree ordering algorithm is especially recommended for problems whose resultant moment-method matrices possess a higher condition number.

§7.2. Future Work

A number of areas for future work on the application of wavelets in computational electromagnetics have been identified.

- Multilevel algorithm

  As already discussed in Chapter 2, the multilevel algorithm is one of efficient fast solution techniques for integral equations. The rectangular and the triangular functions combined with multigrids were employed to implement the multilevel iterative algorithm in [31] and [78], respectively. In [68], we also implemented a multilevel algorithm utilizing the multi-p hierarchical basis functions. These algorithms have a significant drawback, i.e., the condition number increases with the increment of the polynomial degree of the basis functions used. A multilevel algorithm was also implemented based on the FMM, which requires hierarchical grouping of grids (a tree structure of spatial decomposition). Wavelets are optimal hierarchical basis functions and provide a natural mechanism for multilevel algorithms. The resulting matrices obtained with the use of wavelets in MoM have a hierarchical structure as shown in Fig. 2.4, which provides simple multilevel operators, prolongation and projection operators. Moreover, the implementation of the multilevel algorithms using wavelets is much easier than others discussed above.

- Inverse problems

  The CG-FFT method has been successfully utilized for the inverse problems related to ultrasonic imaging in [51] and acoustic imaging in [53]. The inverse problems are driven by a forward solver. The methods described in this work have been proven to be efficient means for the electromagnetic scattering, and can be further applied to electromagnetic inverse problems. The algorithm in Chapter 6 is especially recommended for use in general three-dimensional microwave imaging.

- Spectral domain methods

  The spectral domain method has been successfully applied to a class of electromagnetic problems involving the microstrip-type structures. One of the key problems in this method is the selection of the basis functions and test functions, which determines the convergence of the integrals in the Fourier domain, related to the evaluation of the elements of the MoM matrices [30]. Wavelets with compact support both in time and Fourier domains are available in literature, and provide an important property, i.e., localization both in time and Fourier domains, which can be further exploited in the spectral domain method.

- Genetic algorithms

  The genetic algorithm is one of the global optimization methods based on the concept of natural selection and genetics. By searching through an encoded variable space, the genetic algorithm iteratively improves a population of solutions, and thus is a class of computationally intensive problems [69]. The

applications of fast solution techniques described in the work will dramatically improve the performance of genetic algorithms for electromagnetic inverse or optimization problems.

- Wavelets versus wavelet packets

  As discussed in Chapter 1, two categories of wavelet packets, namely the best basis algorithms [59], [66], [67], [74] and the predefined algorithms [75], [84], have been used in computational electromagnetics. The use of wavelet packets generates sparser MoM matrices than those obtained with the use of the wavelet transforms since more wavelets that have vanishing moments are involved. The wavelet transform, however, is the simplest form of wavelet packet transforms [67], [75], and thus is less expensive than a wavelet packet transform. A quantitative comparison of the wavelet transform versus a wavelet packet transform needs to be investigated by considering the trade-off between the computational cost of transform algorithms and that for solving the resultant sparse matrix equations.

Appendix A

WAVELETS

§ A.1 Biorthogonal Wavelets

Biorthogonal wavelets have been considered to gain more flexibility in the construction of wavelets since they only require that $\{\phi(x-n); n \in \boldsymbol{Z}\}$ form a Riesz bases of $\boldsymbol{V}_0$. Since (2.1) and (2.2), there exist two sequences $\{h_n\}$ and $\{g_n\}$ such that the scaling function ϕ and the wavelet function ψ satisfy the following equation

$$\begin{cases} \phi(x) = \sqrt{2}\sum_n h_n \phi(2x-n) \\ \psi(x) = \sqrt{2}\sum_n g_n \phi(2x-n) \end{cases} \tag{A.1}$$

with $\boldsymbol{V}_j = Span\{\phi_{j,n} = 2^{j/2}\phi(2^j x - n); n \in \boldsymbol{Z}\}$ and $\boldsymbol{W}_j = Span\{\psi_{j,n} = 2^{j/2}\psi(2^j x - n)\}$ generating a primary multiresolution analysis (MRA).

Similarly, their dual functions $\widetilde{\phi}$ and $\widetilde{\psi}$ satisfy

$$\begin{cases} \widetilde{\phi}(x) = \sqrt{2}\sum_n \widetilde{h}_n \widetilde{\phi}(2x-n) \\ \widetilde{\psi}(x) = \sqrt{2}\sum_n \widetilde{g}_n \widetilde{\phi}(2x-n) \end{cases} \tag{A.2}$$

and $\widetilde{V}_j = Span\{\widetilde{\phi}_{j,n} = 2^{j/2}\widetilde{\phi}(2^j x - n)\}$ and $\widetilde{W}_j = Span\{\widetilde{\psi}_{j,n} = 2^{j/2}\widetilde{\psi}(2^j x - n)\}$ are the dual MRA approximation spaces. A complete development of biorthogonal wavelets with spline functions is given in [5]. Figs. A.1 and A.2 show the biorthogonal scaling functions and wavelets constructed with rectangular and triangular pulse functions. The biorthogonal scaling functions and wavelets are symmetric and compactly supported. Moreover, all the filter coefficients are dyadic and rational and thus are very suitable for fast computations since division by 2 can be done very fast on a digital computer. Another attractive property is that the closed-form expressions for the scaling function and their wavelet are available at all x. The disadvantages are that they do not generate orthogonal MRA, and the support widths for the primary and dual scaling functions are different.

§ A.2 Semi-Orthogonal Wavelets

C. K. Chui introduced the semi-orthogonal wavelets [6], [7], [26]. Semi-orthogonal wavelets are biorthogonal wavelets that generate an orthogonal MRA. These semi-orthogonal wavelets are based upon the cardinal B-Splines, as are the Battle-Lemarié orthogonal wavelets. For an index k, define the scaling function

$$\phi(x) = N_k(x) \tag{A.3}$$

where $N_k(x)$ is the cardinal B-spline that is expressed recursively as a convolution $N_k = N_{k-1} * N_1$ with the rectangular pulse function $N_1(x) = \chi_{[0,1]}(x)$. The dilated and translated sequence $\{\phi_{j,n} = 2^{j/2}\phi(2^j x - n); n \in \mathbf{Z}\}$ forms a Riesz basis for V_j, the function space consisting of all splines of order $k-1$. The general two-scale relationship for these scaling functions is given by the well-known B-spline identity

$$N_k(x) = \sum_{n=1}^{k} 2^{-k+1} \binom{k}{n} N_k(2x-n) \tag{A.4}$$

which gives the sequence $\{h_n\}$ in (A. 1). The corresponding wavelets are given by [6]

$$\psi(x) = \sum_{n \in Z} g_n N_k(2x-n) \tag{A.5}$$

with the sequence $\{g_n\}$ given by

$$g_n = g_{k,n} = \frac{(-1)^n}{2^{k-1}} \sum_{l=0}^{k} \binom{k}{l} N_{2k}(n-l+1), \qquad 0 \le j \le 3k-2 \tag{A.6}$$

Associated with the primary functions ϕ and ψ are dual functions $\tilde{\phi}$ and $\tilde{\psi}$, which are given by [6], [46]

$$\begin{cases} \tilde{\phi}(x) = \sum_{n \in Z} 2\tilde{h}_n \tilde{\phi}_k(2x-n) \\ \tilde{\phi}(x) = \sum_{n \in Z} 2\tilde{g}_n \tilde{\phi}_k(2x-n) \end{cases} \tag{A.7}$$

with

$$\begin{cases} \tilde{h}_n = \sum_{l \in Z} g_{n+2k-1-2l} \alpha_l^{(k)} \\ \tilde{g}_n = \sum_{l \in Z} h_{n+2k-1-2l} \alpha_l^{(k)} \end{cases} \tag{A.8}$$

and the sequence $\{\alpha_j^{(k)}\}$ is uniquely determined by using the interpolatory property of the fundamental spline of order $2k$

$$L_{2k}(m) = \sum_{j \in Z} \alpha_j^{(k)} N_{2k}(m + k - j) = \delta_{k,0} \tag{A.9}$$

$\delta_{k,0}$ is the standard Kronecker delta function. Note that the infinite sequence $\{\alpha_j^{(k)}\}$ is of exponential decay, so are $\{\tilde{h}_n\}$ and $\{\tilde{g}_n\}$.

The collections $\{\tilde{\phi}_{j,k}; k \in \boldsymbol{Z}\}$ and $\{\tilde{\psi}_{j,k}; k \in \boldsymbol{Z}\}$ form the dual MRA approximation subspaces $\tilde{\boldsymbol{V}}_j$ and $\tilde{\boldsymbol{W}}_j$ which are mutually orthogonal,

$$\tilde{\boldsymbol{V}}_j \perp \boldsymbol{W}_{j'} \qquad \boldsymbol{V}_j \perp \tilde{\boldsymbol{W}}_{j'} \qquad j \neq j' \tag{A.10}$$

Consequently, $\tilde{\boldsymbol{W}}_{j'} \perp \boldsymbol{W}_j$ and $\tilde{\boldsymbol{V}}_{j'} \perp \boldsymbol{V}_j$. Thus the primary and dual functions generate an orthogonal MRA. The functions ϕ and ψ are compactly supported. Their dual functions $\tilde{\phi}$ and $\tilde{\psi}$, however, are not compactly supported. For an index k, the support widths for ϕ and ψ are $[0, k]$ and $[0, 2k-1]$, respectively. When $k = 1$, the result is the Harr system. For $k > 1$, the wavelets are constructed of splines of degree $k - 1$. Semi-orthogonal wavelets are symmetric for even k and antisymetric for odd k. Semi-orthogonal wavelets with $k = 2, 5, 8$, are shown in Fig. A.3.

§ A.3 Orthogonal Wavelets

The construction of orthogonal wavelets is based on an MRA where the collection of the scaling function $\{\phi(x-n); n \in \mathbf{Z}\}$ forms an orthogonal basis of V_0, instead of a Riesz basis. The scaling function and wavelets satisfy (A.1) with

$$g_n = (-1)^n h_{1-n}, \quad \sum_n h_n^2 = 2 \tag{A.11}$$

Two simple examples of orthogonal wavelets are the Harr wavelets and the Shannon wavelets. The Harr wavelets are not continuous in time domain, and the Shannon wavelets decay very slowly. The Mayer wavelets were constructed by using polynomials and decay faster than any inverse polynomial. The scaling function and wavelet function have closed-form expressions only in Fourier domain, and are infinitely supported in time domain as shown in Fig. A.4.

Battle (1987) and Lemariè (1988) constructed, independently, a family of orthogonal wavelet bases [5], which decay exponentially, faster than Meyer wavelets. The Battle-Lemariè wavelets are constructed by orthogonalizing B-spline functions. As a result, closed form expressions for the scaling function and the wavelet are no longer available. The Battle-Lemarié wavelets with N vanishing moments are piecewise polynomial of degree $N-1$, and thus belong to C^{N-2} (i.e., which have $N-2$ times continuous derivatives); $\phi(x)$ is always symmetric, while $\psi(x)$ is symmetric for odd N and antisymmetric for even N about $x = 1/2$ axis. They are infinitely supported just like the Meyer wavelets.

In 1988, Daubechies introduced a family of wavelets that are not only orthonormal, but also have compact support both in the time and Fourier domains [5]. The development of this

family has had a profound impact and these wavelets are used extensively in practice. Several members of this family are displayed in Fig. A.5. These wavelets are also indexed by a positive integer N, where N is the number of vanishing moments. They are supported on an interval of length $2N-1$, and the smoothness increases as N increases. Unfortunately, as proved in [5], orthogonal wavelet bases, except the Haar wavelets, with compact support are asymmetric, and no closed-form expressions are available.

Another family of orthonormal wavelets constructed by Daubechies is the family of coiflets, named by her in honor of wavelet researcher Ronald Coifman, who suggested a wavelet-based MRA in which the scaling function also has vanishing moments [5]. There are no closed form expressions, too. Some examples are given in Fig. A.6. It is clear from the figure that ϕ and ψ are much more symmetric than those of Daubechies' wavelets, at the expense of their support width, i.e., coiflets with k vanishing moments have typically support width $3k-1$, as compared to $2k-1$ for the Daubechies' wavelets shown in Fig. A.4.

§ A.4 The Fast Wavelet Transform Algorithm

The fast wavelet transform (FWT) algorithm [24] is extremely useful in practical applications such as the wavelet-based MoM for the numerical solution of integral equations. Like the FFT (fast Fourier transform), the FWT of length N only needs $O(N \log N)$ arithmetic operations. Without loss of generality, let us consider for illustration the biorthogonal FWT algorithm.

With (2.3), a function $f_j \in \boldsymbol{V}_j$ can be written as the sum of a function $f_{j-1} \in \boldsymbol{V}_{j-1}$ and $q_{j-1} \in \boldsymbol{W}_{j-1}$

$$f_j(x) = \sum_k s_{j,k}\phi_{j,k}(x) = f_{j-1} + q_{j-1} \tag{A.12}$$

with

$$\begin{cases} f_{j-1} = \sum_l s_{j-1,l}\phi_{j-1,l}(x) \\ q_{j-1} = \sum_l d_{j-1,l}\psi_{j-1,l}(x) \end{cases} \tag{A.13}$$

where the scaling function coefficients $s_{j,k}$ and wavelet function coefficients $d_{j,k}$ are given by

$$s_{j,k} = \langle f, \tilde{\phi}_{j,k} \rangle, \quad d_{j,k} = \langle f, \tilde{\psi}_{j,k} \rangle \tag{A.14}$$

Due to (A.2), the following relationships exist

$$s_{j-1,l} = \sqrt{2}\sum_k \tilde{h}_{k-2l} s_j, \quad d_{j-1,l} = \sqrt{2}\sum_k \tilde{g}_{k-2l} d_j \tag{A.15}$$

Thus, for given coefficients $s_{J,k}$ at any level J, all the lower level coefficients $s_{j,k}$ and $d_{j,k}$, for $j < J$, can be easily computed. The forward fast transform or decomposition algorithm is shown schematically in Fig. A.7(a), where the arrows represent the decomposition computations.

The inverse FWT algorithm can be derived from the relationship

$$s_{j,l} = \sqrt{2}\sum_k h_{k-2l} s_{j-1,k} + \sqrt{2}\sum_k g_{k-2l} d_{j-1,k} \tag{A.16}$$

A schematic representation of the inverse FWT is shown in Fig. A.7(b).

The filter coefficients completely characterize wavelet bases. It is easily seen that the support width of the wavelets is closely related, proportionally, to the number of arithmetic operations.

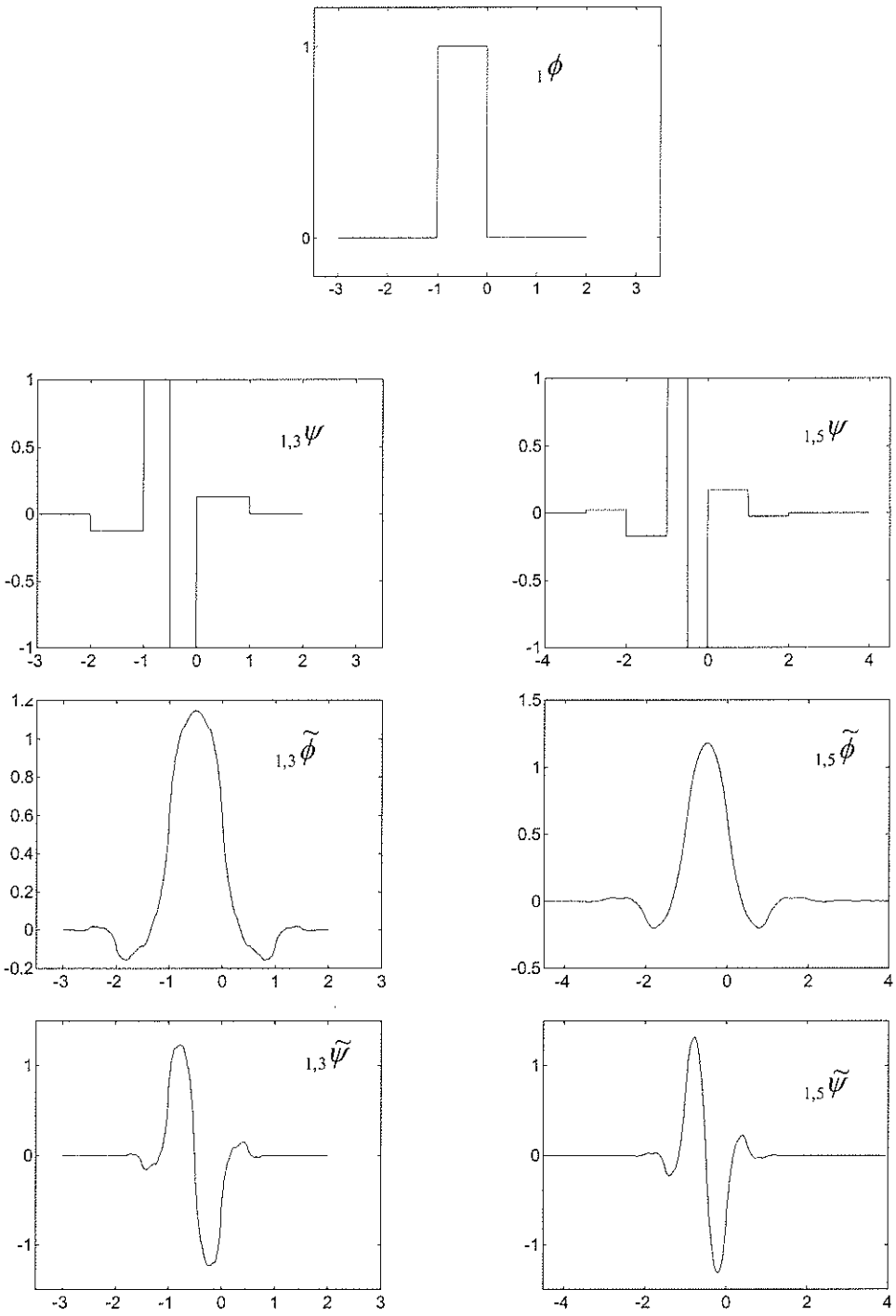

Fig. A.1. Biorthogonal scaling functions ${}_N\phi$, ${}_{N,\tilde{N}}\tilde{\phi}$ and wavelets ${}_{N,\tilde{N}}\psi$, ${}_{N,\tilde{N}}\tilde{\psi}$ for $N=1$, $\tilde{N}=3,5$, where support ${}_{N,\tilde{N}}\tilde{\phi}=[-\tilde{N},\tilde{N}]$, support ${}_{N,\tilde{N}}\psi={}_{N,\tilde{N}}\tilde{\psi}=[-(\tilde{N}-1)/2,(\tilde{N}+1)/2]$.

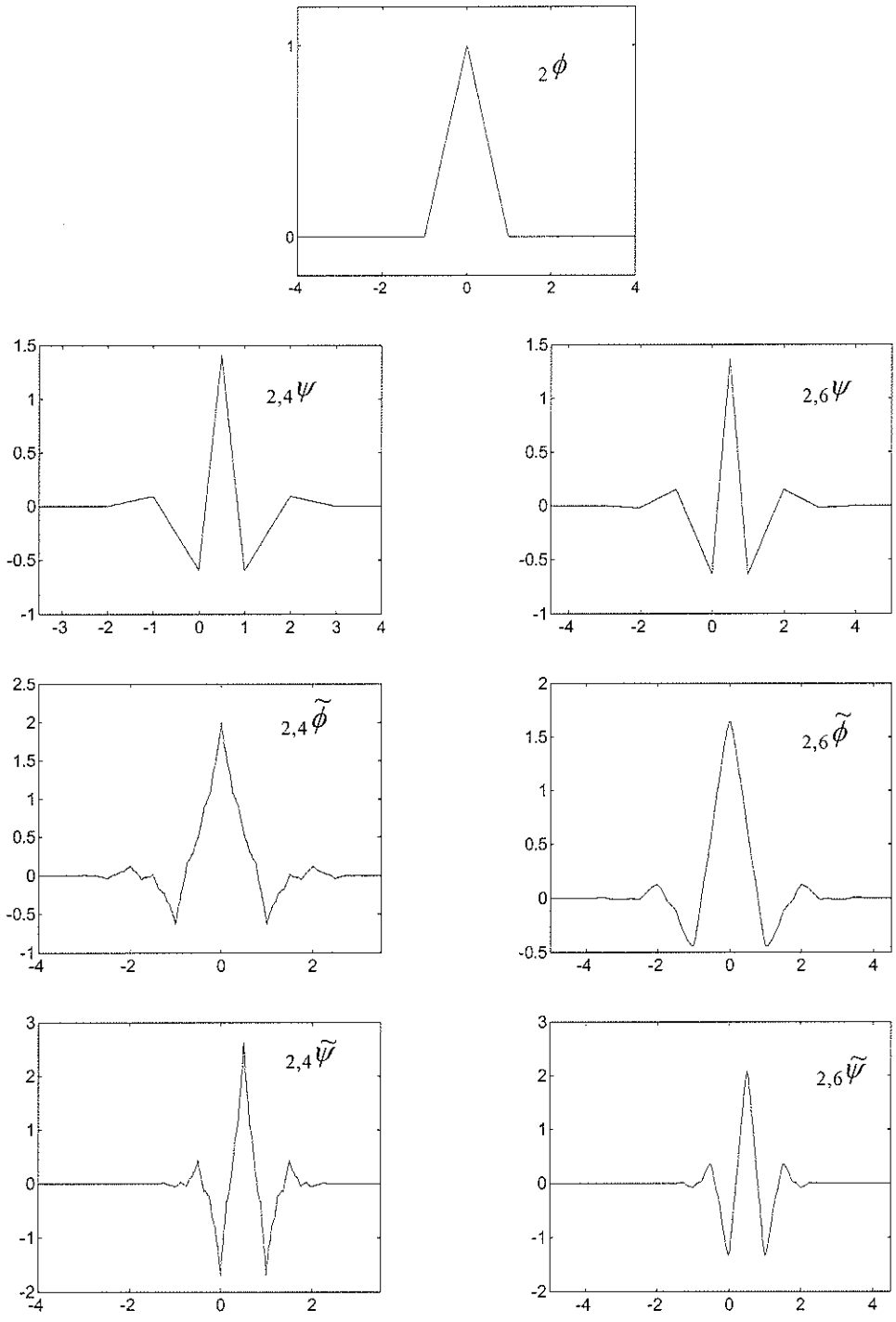

Fig. A.2. Biorthogonal scaling functions ${}_N\phi$, ${}_{N,\tilde{N}}\tilde{\phi}$ and wavelets ${}_{N,\tilde{N}}\psi$, ${}_{N,\tilde{N}}\tilde{\psi}$ for $N=2$, $\tilde{N}=4,6$, where support ${}_{N,\tilde{N}}\tilde{\phi}=[-\tilde{N},\tilde{N}]$, support ${}_{N,\tilde{N}}\psi={}_{N,\tilde{N}}\tilde{\psi}=[-\tilde{N}/2,\tilde{N}/2+1]$.

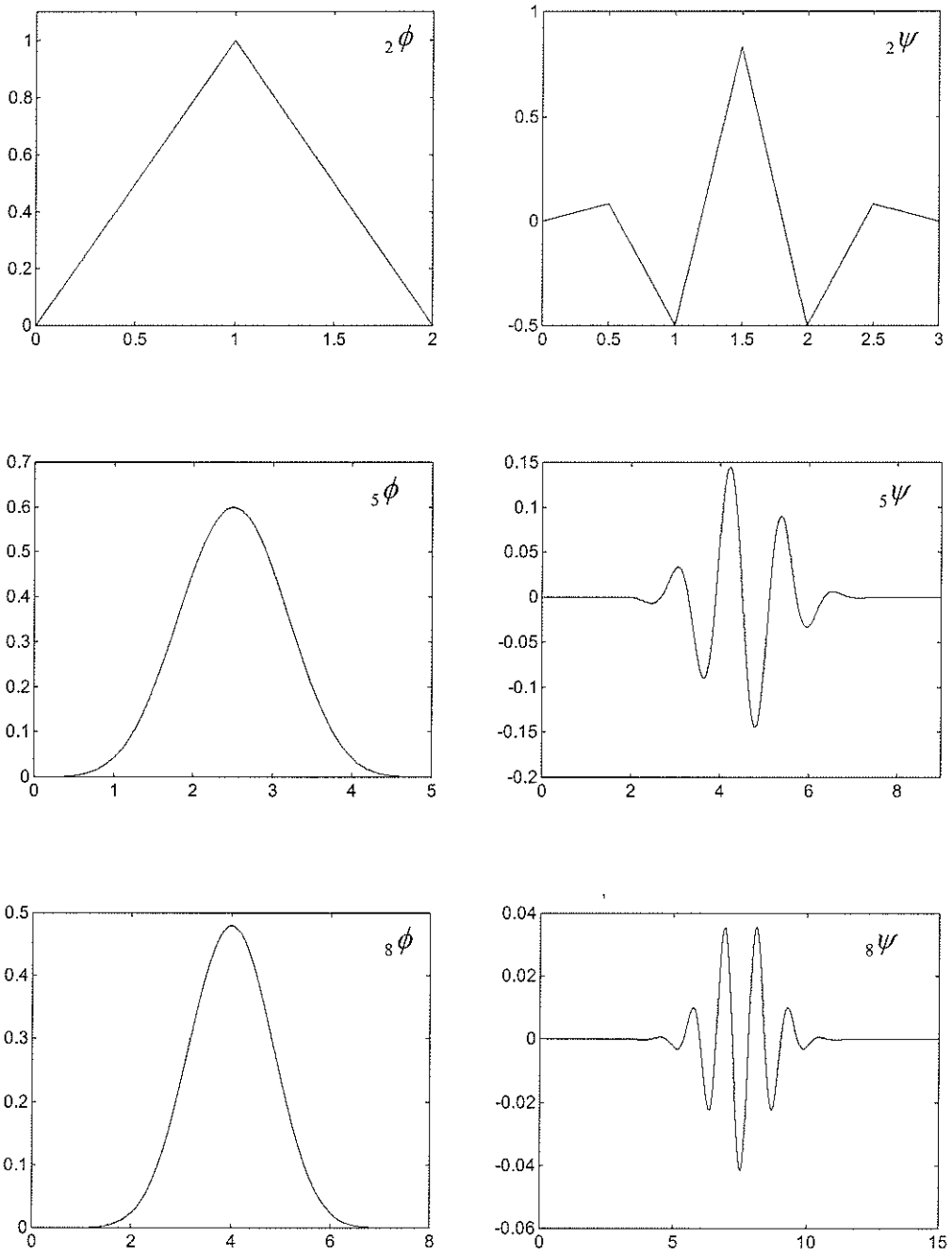

Fig. A.3. Semi-orthogonal scaling function ${}_k\phi$ and wavelets ${}_k\psi$ with k vanishing moments, for $k = 2$, 5, and 8, where support ${}_k\phi = [0, k]$ and support ${}_k\psi = [0, 2k-1]$.

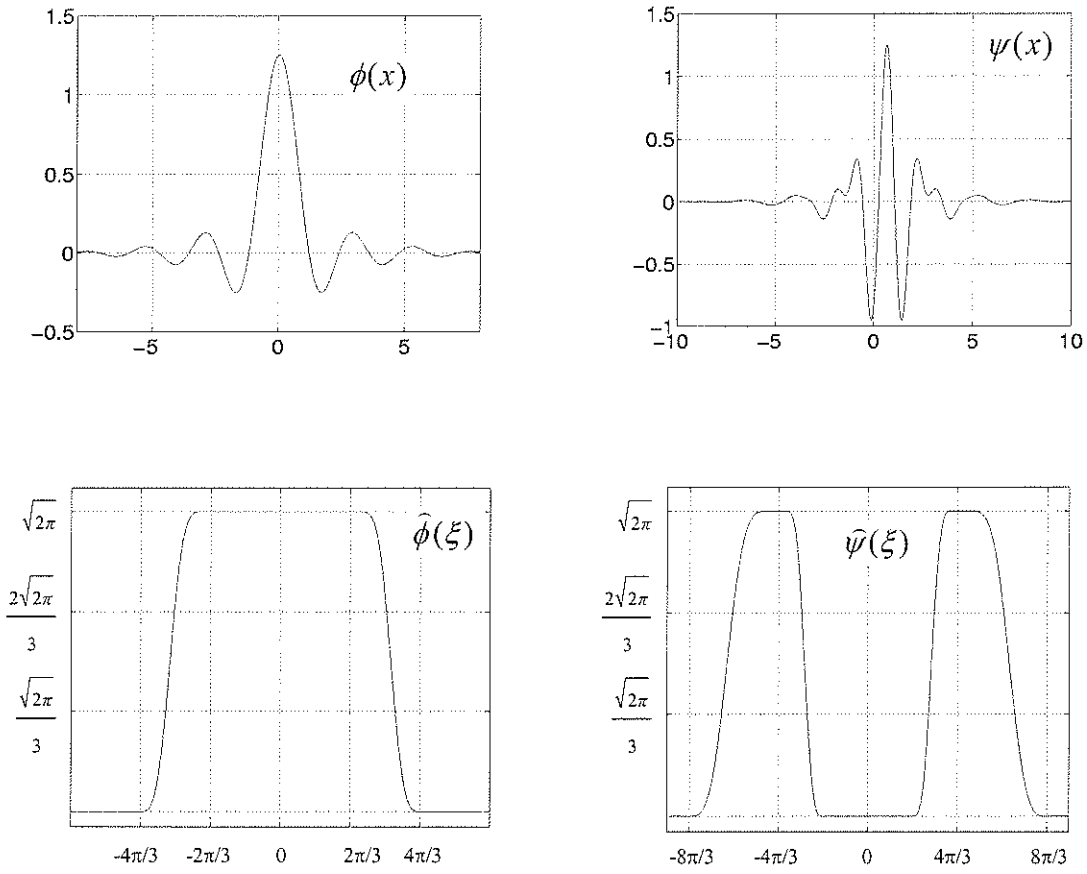

Fig. A.4. Scaling function $\phi(x)$ and wavelet function $\psi(x)$ and their Fourier transformations $\hat{\phi}(\xi)$ and $\hat{\psi}(\xi)$ for the Mayer wavelets.

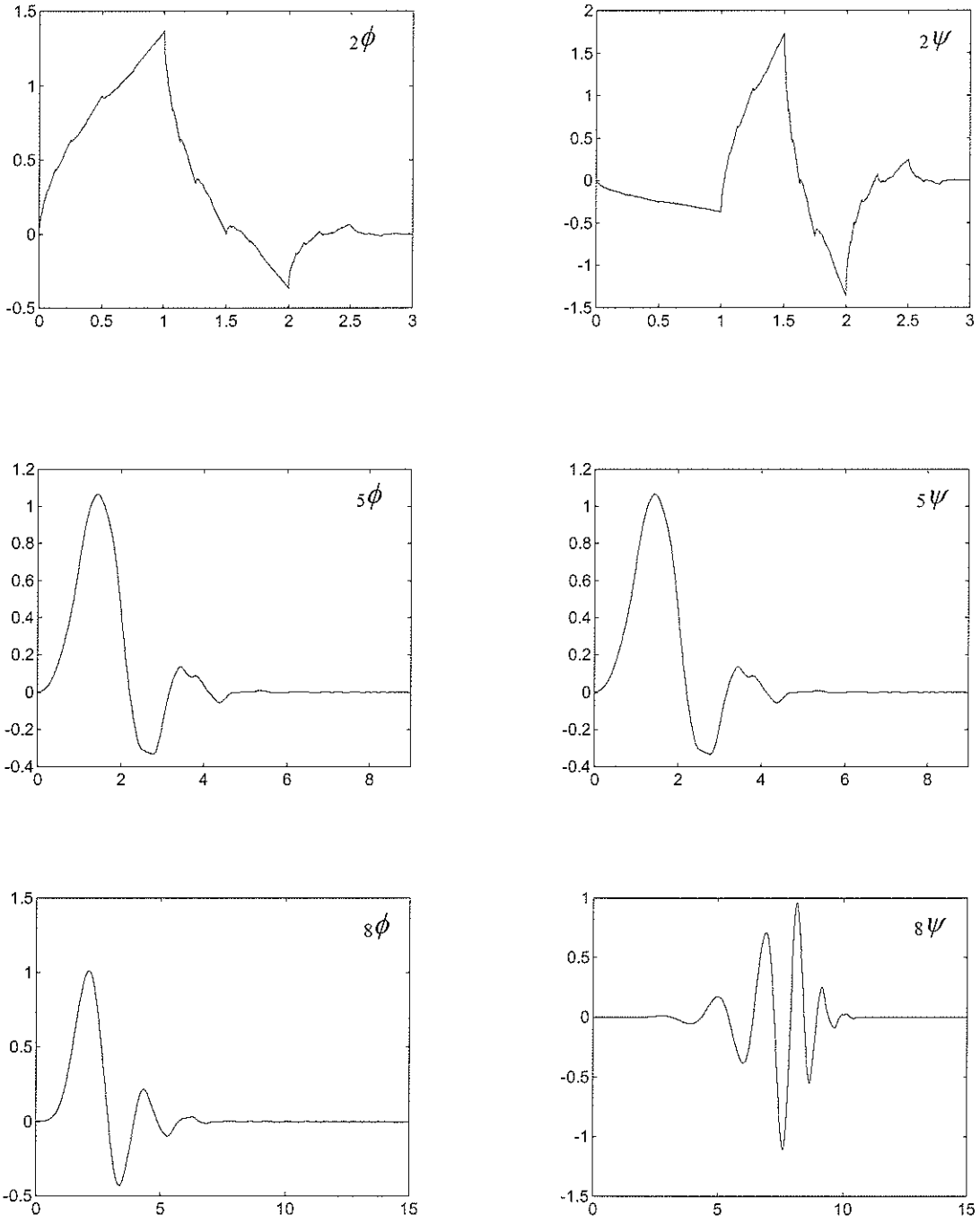

Fig. A.5. Daubechies' wavelets ${}_N\phi$ and ${}_N\psi$ with a number N of vanishing moments and a support width $2N-1$, for $N=2$, 5, and 8.

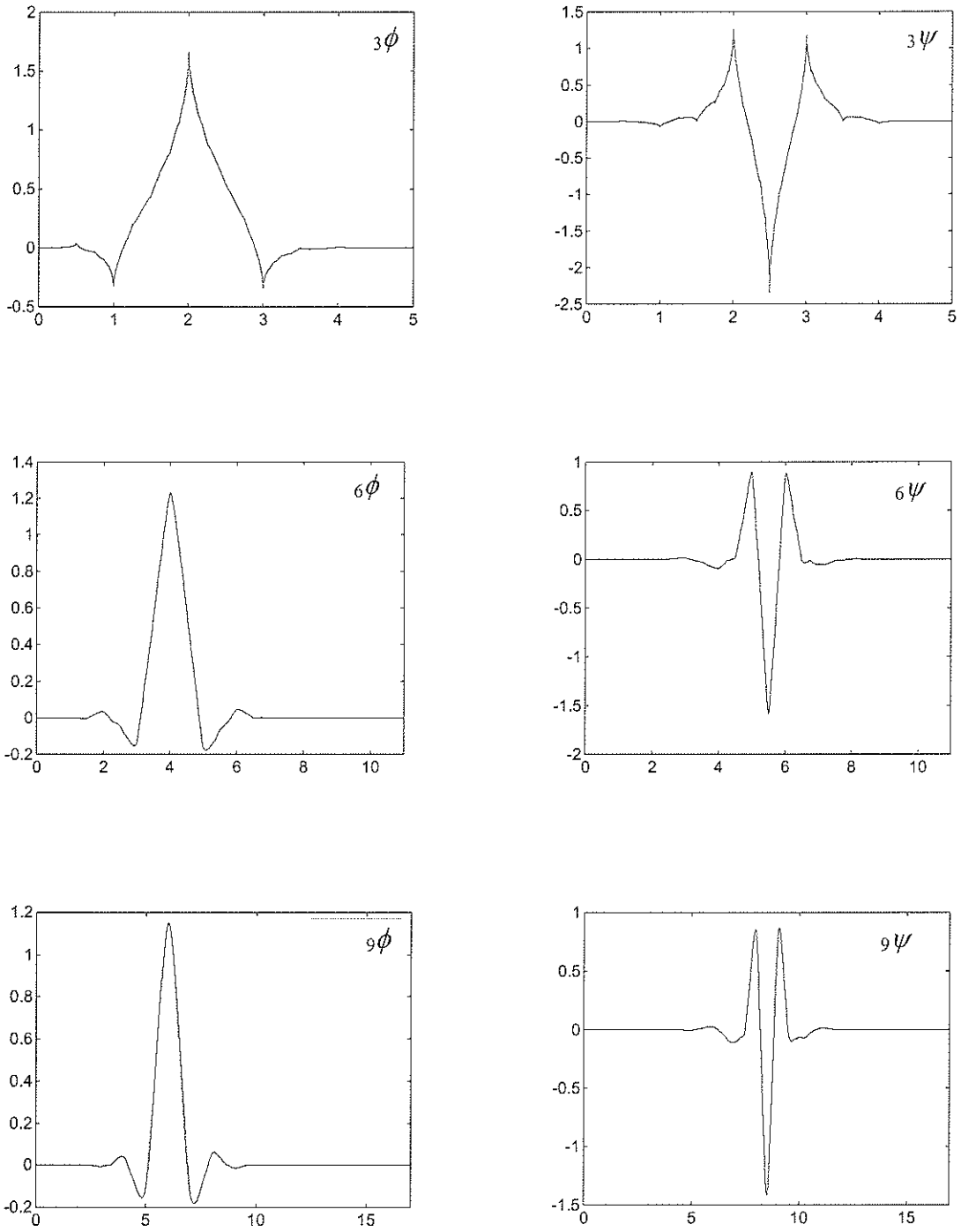

Fig. A.6. Coiflets ${}_N\phi$ and ${}_N\psi$ with N vanishing moments and support width $3N-1$ for $N=3$, 6, and 9.

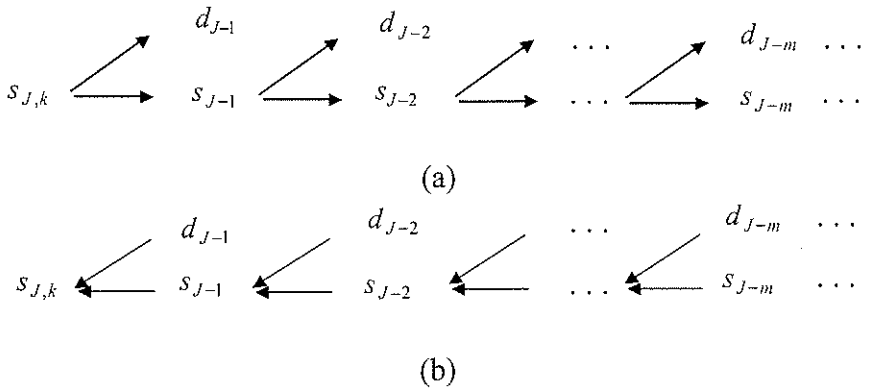

Fig. A.7. Fast wavelet transform scheme: (a) forward algorithm; (b) inverse algorithm.

Appendix B

COMPUTATION OF SEMI-ORTHOGONAL WAVELETS

In order to work only with integers, let

$$\begin{cases} \Psi(x) = (2k-1)!\,\psi(x) \\ \Psi(x) = \dfrac{1}{2^{k-1}} \displaystyle\sum_{j=0}^{3k-2} (-1)^j \gamma_j^k N_k(2x-j) \end{cases} \tag{B.1}$$

with $N_k(x)$ and $\psi(x)$ being given in (A.5) and (A.6), respectively.

In comparison with (A.6), we obtain

$$\begin{cases} \gamma_j^k = \displaystyle\sum_{l=0}^{k} b_l^k \chi^{2k-1}(j-l) \\ \chi^{2k-1}(j) = (2k-1)!\; N_{2k}(j+1) \\ b_l^k = \dbinom{k}{l} = \dfrac{k!}{l!(k-l)!} \end{cases} \tag{B.2}$$

The sequence $\{\gamma_j^k; j \in [0, 3k-2]\}$ is totally positive. Utilizing the notations in Fig. B.1, the computational procedure for the sequence $\{\gamma_j^k\}$ is schematically described in Fig. B.2.

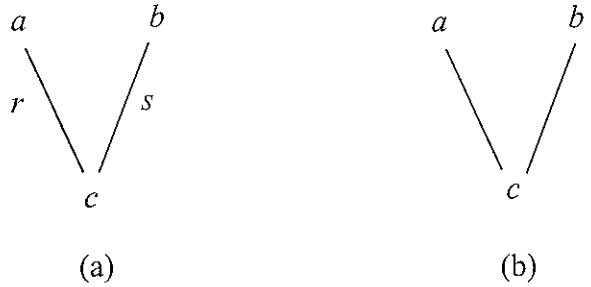

Fig. B.1. Notations: (a) $c = ra + sb$, (b) $c = a + b$.

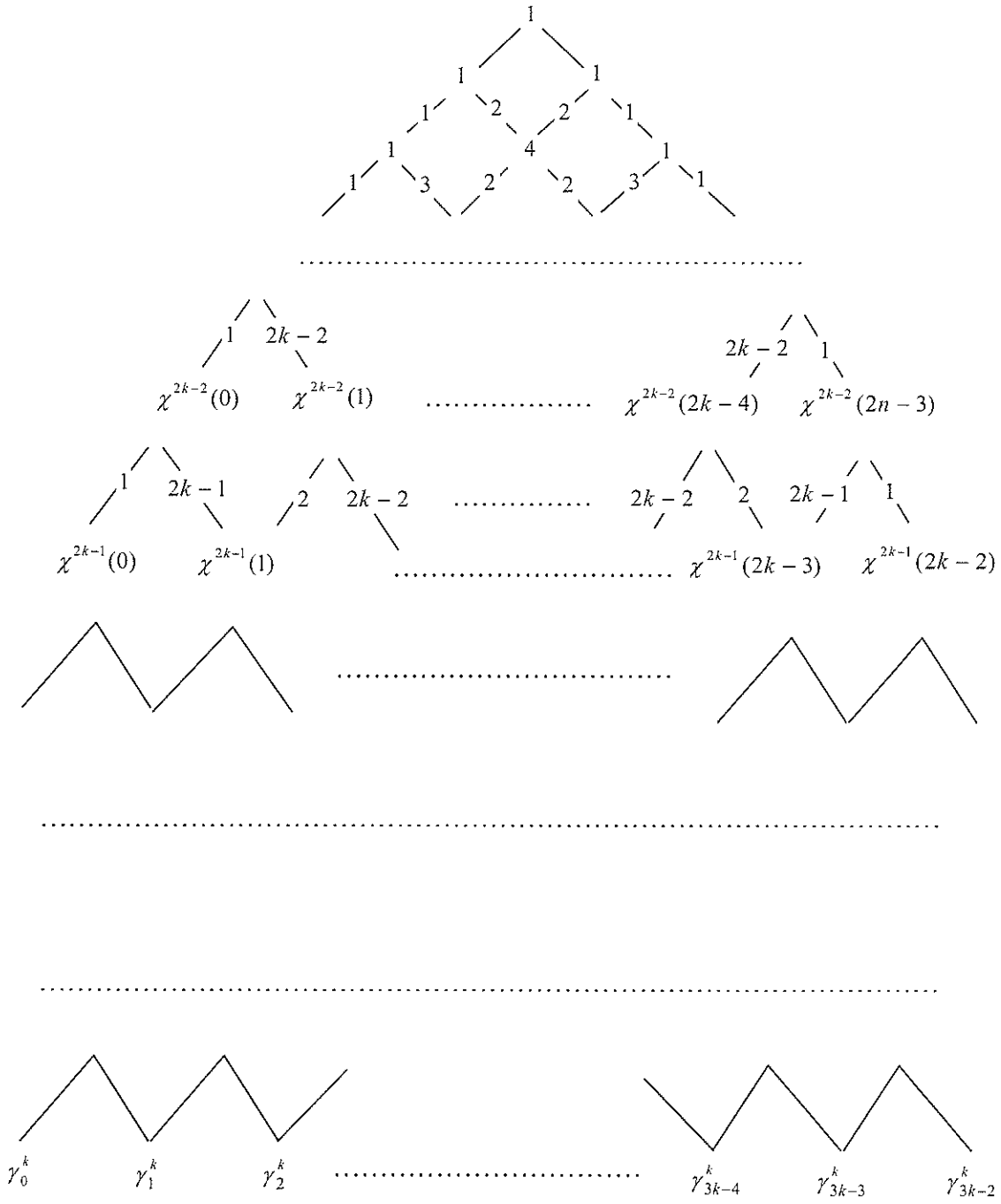

Fig. B.2. Computation of the sequence $\{\gamma_j^k; j \in [0,3k-2]\}$.

Appendix C

SOFTWARE STRUCTURE

The structure chart of a software system illustrates the partitioning of the system into modules showing their hierarchy, organization, and communications, and is also a powerful means of documentation of a software system that helps the designers. The structure chart symbols defined in [3] are used in this appendix.

Although several computer programs in Fortran 90 with the memory being allocated dynamically have been implemented for the research work in this thesis, they share the common structure as depicted in Fig. C.1. The modules for solving matrix equations and the fast wavelet transforms used in Fig. C.1 are packaged separately and described in Figs. C.2 and C.3, respectively.

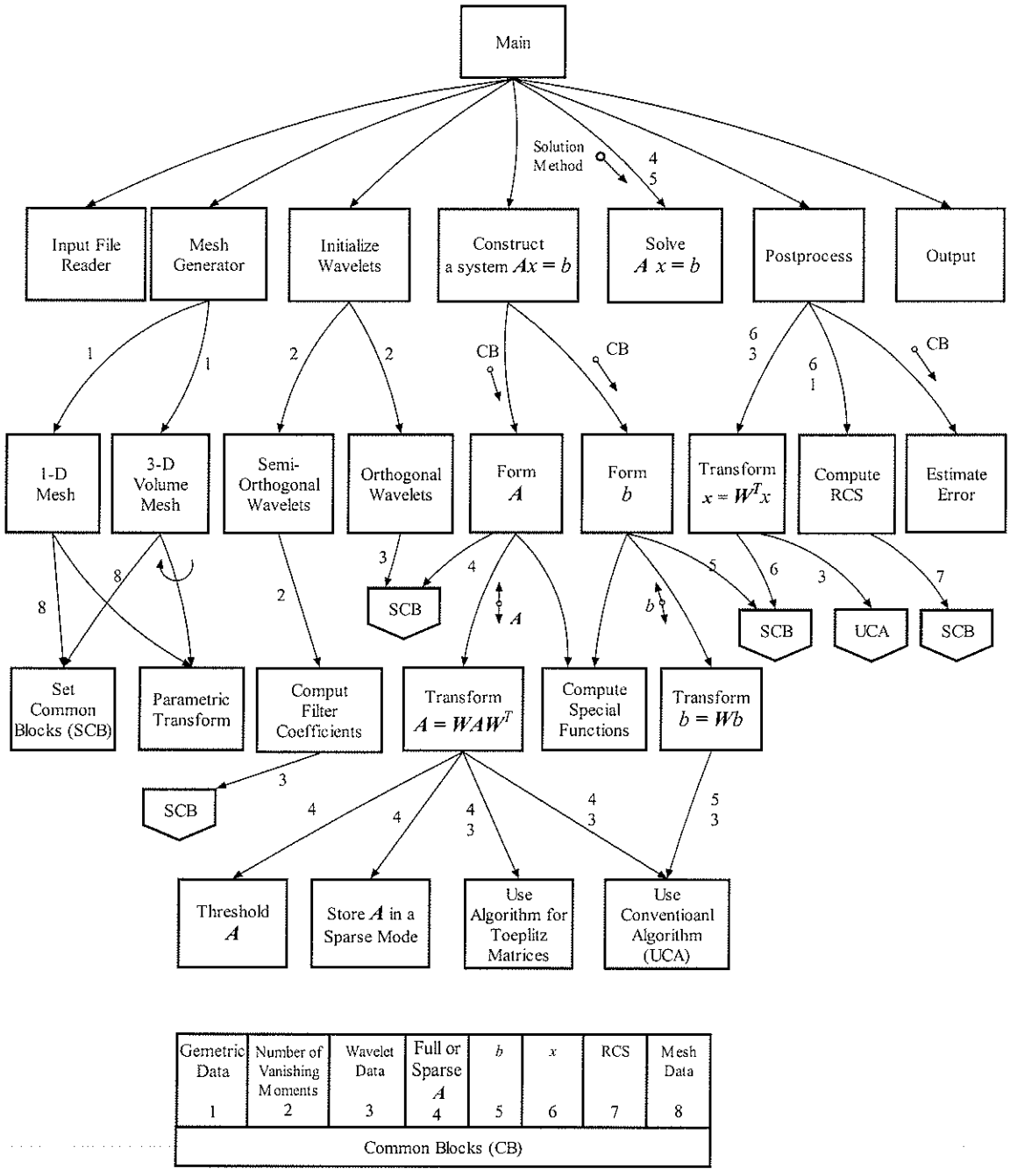

Fig. C.1. Structure chart of the software system used.

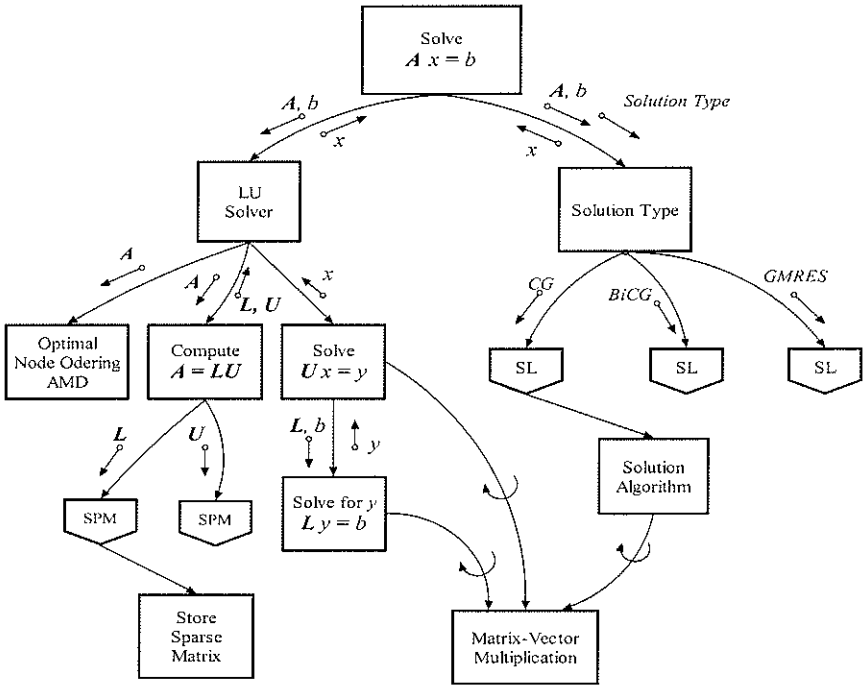

Fig. C.2. Structure chart of the solution module for matrix equations.

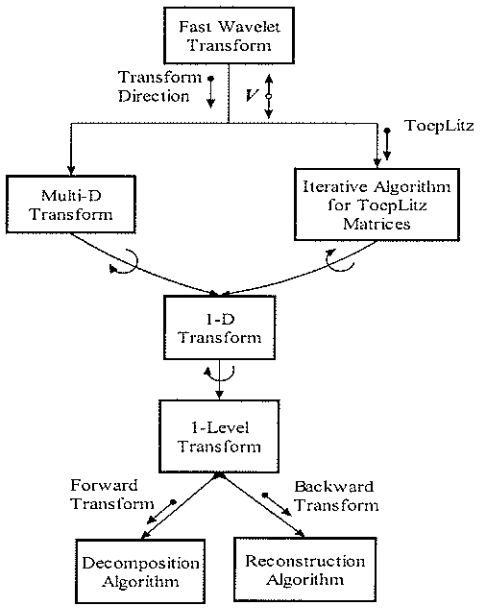

Fig. C.3. Structure chart of the fast wavelet transform module for a give matrix V of order $n \times m$.

REFERENCES

(In chronological order)

Books

[1] R. F. Harrington, *Time-Harmonic Electromagnetic fields*, New York: McGraw-Hill, 1961.

[2] S. V. Richard, *Matrix Iterative Analysis*, New Jersey: Englewood Cliffs, 1962.

[3] Meilir Page-Jones, *The Practical Guide to Structured Systems Design*, Englewood Cliffs, New Jersey, 1988.

[4] Y. Meyer, *Wavelets and Operators*, Cambridge University Press, 1992.

[5] I. Daubechies, *Ten Lectures on Wavelets,* Philadelphia: SIAM, 1992.

[6] C. K. Chui, *An Introduction to Wavelets*, Boston, MA: Academic, 1992.

[7] C. K. Chui, *Wavelets: A Tutorial in Theory and Applications,* Boston, MA: Academic, 1992.

[8] D. B. Ingham and Y. Yuan, *The Boundary Element Method for Solving Improperly Posed Problems*, Boston: Computational Mechanics, 1994.

[9] W. Hackbusch, *Integral Equations,* Berlin: Birkhäuser, 1995.

Papers

[10] J. R. Mautz and R. F. Harrington, "Radiation and scattering from bodies of revolution," *Appl. Sci. Res.*, vol. 20, pp. 405–435, June 1969.

[11] D. E. Levesay and K. Chen, "Electromagnetic fields inside arbitrarily shaped biological bodies," *IEEE Trans. Microwave Theory Tech.*, vol. 22, pp. 1273–1280, December 1974.

[12] A. Jannies, "Influence of eigenvalue spectrum on the convergence rate of the conjugate gradient method," *J. Inst. Math. Appl.,* vol. 20, pp. 61–72, 1976.

[13] T. K. Wu and L. L. Tsu, "Scattering from arbitrarily-shaped dielectric bodies of revolution," *Radio Sci.,* vol. 12, pp. 709–718, Oct. 1977.

[14] A. Brandt, "Multi-level adaptive solutions to the boundary value problems, "*Math. Comp.*, vol. 31, pp. 333–390, 1977.

[15] W. L. Miranker and V. Y. Pan, "Methods of aggregation, "*Linear Algebra Appl.*, vol. 29, pp. 231–237, 1980.

[16] S. Lee, J. Boersma, C. Law, and G. A. Deschamps, "Singularity in Green's function and its numerical evaluation," *IEEE Trans. Antennas Propagat.,* vol. 28, pp. 311–317, May 1980.

[17] P. W. Hemker and H. Schippers, "Multiple grid methods for the solution of Fredholm integral equations of the second kind," *Math. Comput.*, vol. 36, pp. 215–232, 1981.

[18] F. Chatelin and W. L. Miranker, "Acceleration by aggregation of successive approximation methods," *Linear Algebra Appl.,* vol. 43, pp. 17–47, 1982.

[19] M. F. Catedra, "Solution of some electromagnetic problems using the fast Fourier transform with conjugate gradient method," *Electron. Letter,* vol. 22, no. 9, pp. 1049–1051, 1986.

[20] A. F. Peterson, C. F. Smith, and R. Mittra, "Eigenvalues of the moment-method matrix and their effect on the convergence of the conjugate gradient algorithm," *IEEE Trans. Antennas Propagat.,* vol. 36, pp. 1177–1179, Aug, 1988.

[21] M. F. Catedra and J. G. Guevas, "A scheme to analyze conducting plates of resonant size using the conjugate gradient method and the fast Fourier transform," *IEEE Trans. Antennas Propagat.*, vol. 36, pp. 1744–1752, December 1988.

[22] V. Rokhlin, "Rapid solution of integral equations of scattering theory in two dimensions," *J Comput. Phys.*, vol. 86, pp. 414–439, February 1990.

[23] S. D. Gedney and R. Mittra, "The use of FFT for the efficient solution of the problem of electromagnetic scattering by a body of revolution," *IEEE Trans. Antennas Propagat.*, vol. 38, pp. 312–322, March 1990.

[24] G. Beylkin, R. Coifman, and V. Rokhlin, "Fast wavelet transforms and numerical algorithms I," *Commun. Pure Appl. Math.*, vol. 44, pp. 141–183, 1991.

[25] M. R. Barclay and V. T. Rush, "Moment-method analysis of large axially symmetric reflector antennas using entire-domain functions," *IEEE Trans. Antennas Propagat.*, vol. 39, pp. 491–496, April 1991.

[26] C.K. Chui and J. Wang, "On compactly supported spline wavelets and a duality principle," *Trans. Amer. Math. Soc.*, vol. 330, pp. 903–915, 1992.

[27] P. Zwamborn and P. M. van den Berg, "The three-dimensional weak form of conjugate gradient FFT method for solving scattering problems," *IEEE Trans. Microwave Theory Tech.*, vol. 9, pp. 1757–1766, September 1992.

[28] B. Alpert, "A class of bases in $\boldsymbol{L^2(R)}$ for the sparse representation of integral operators," *SIAM J. Math. Anal.*, vol. 24, pp. 245–262, January, 1993.

[29] B. Alpert, G. Beylkin, R. Coifman and V. Rokhlin, "Wavelet-like bases for the fast solution of second-kind integral equations," *SIAM J. Sci. Comput.*, vol. 14, pp. 159–184, January, 1993.

[30] M. I. Aksun and R. Mittra, "Choice of expansion and testing functions for the method of moments applied to a class of electromagnetic problems," *Trans. Microwave Theory Tech.*, vol. 41, pp. 503–509, March 1993.

[31] K. Kalbasi and K. R. Demarest, "A multilevel formulation of the method of moments," *IEEE Trans. Antennas Propagat.*, vol. 41, pp. 589–599, May 1993.

[32] F. X. Canning, "Improved impedance matrix localization method," *IEEE Trans. Antennas Propagat.*, vol. 41, pp. 659–667, May 1993.

[33] B. Z. Steinberg and Y. Leviatan, "On the use of wavelet expansions in the method of moments," *IEEE Trans. Antennas Propagat.*, vol. 41, pp. 610–619, May 1993.

[34] R. Coifman, V. Rokhlin, and S. Wandzura, "The fast multipole method for the wave equations: a pedestrian prescription," *IEEE Antennas Propagat. Mag.*, vol. 35, pp. 7–12, June 1993.

[35] R. L. Wagner, G. P. Otto, and W. C. Chew, "Fast wavelet mode computation using wavelet-like basis functions, " *IEEE Trans. Microwave Theory Tech.*, vol. 42, no. 2, pp. 234–240, February 1994.

[36] J. Basterrechea and M. F. Cátedra, "Computation of microstrip S-parameters using a CG-FFT Scheme," *IEEE Trans. on Microwave Theory and Techniques*, vol. 42, no. 2, pp. 234–240, February 1994.

[37] B. Z. Steinberg, "A multiresolution theory of scattering and diffraction," *Wave Motion,* vol. 19, pp. 213–232, 1994.

[38] G. W. Pan and X. Zhu, "The application of adaptive wavelet expansion method in the computation of parameter matrices of multiple lossy transmission lines," *IEEE AP-S Symposium*, pp. 29–32, June 1994.

[39] R. Wagner and W. C. Chew, "A ray-propagation fast multipole algorithm," *Micro. Opt. Tech. Lett.*, vol. 7, no. 10, pp. 435–438, July 1994.

[40] K. F. Sabet and Linda P.B. Katehi, "Analysis of integrated millimeter-wave and submillimeter-wave waveguides using orthonomal wavelet expansions," *IEEE Trans. Microwave Theory Tech.*, vol. 42, pp. 2412–2422, Dec. 1994.

[41] G. Wang and G. W. Pan, "Full wave analysis of microstrip floating line structures by wavelet expansion methods," *IEEE Trans. Microwave Theory Tech.*, vol. 43, pp. 131–142, Jan. 1995.

[42] G. Wang, "A hybrid wavelet expansion and boundary element analysis of electromagnetic scattering from conducting objects," *IEEE Trans. Antennas Propagat.*, vol. 43, pp. 170–178, February 1995.

[43] G. Wang, G. W. Pan, and B. K. Gilbert, "A hybrid wavelet expansion and boundary element analysis for multiconductor transmission lines in multilayered dielectrics," *IEEE Trans. Microwave Theory Tech.*, vol. 43, pp. 664–675, March 1995.

[44] J. C. Goswami, A. K. Chan, and C. K. Chui, "On solving first-kind integral equations using wavelets on a bounded interval," *IEEE Trans. Antennas Propagat.*, vol. 43, pp. 614–622, June 1995.

[45] R. L. Wagner and W. C. Chew, "A study of wavelets for the solution of electromagnetic integral equations," *IEEE Trans. Antennas Propagat.*, vol. 43, pp. 802–810, August 1995.

[46] C. K. Chui, J. C. Goswami, A. K. Chan, "Fast integral wavelet transform on a dense set of the time-scale domain," *Numeri. Math.,* vol. 70, pp. 283–302, 1995.

[47] J. M. Song and W. C. Chew, "Multilevel fast multipole algorithm for solving combined field integral equation of electromagnetic scattering," *Micro. Opt. Tech. Lett.,* vol. 10, no. 1, pp 14–19, September 1995.

[48] H. Gan and W. C. Chew, "A discrete BCG–FFT algorithm for solving 3–D inhomogeneous scatterer problems," *J. Electromag. Waves Appl.*, vol. 9, no. 10, pp. 1339–1357, 1995.

[49] G. Wang, "On the utilization of periodic wavelet expansions in the moment methods," *IEEE Trans. Microwave Theory Tech.*, vol. 43, pp. 2495–2498, October 1995.

[50] N. Hu and I. N. Katz, "Multi-*p* method: Iterative algorithm for the *p*-version of finite element analysis," *SIAM J. Sci. Comput.,* vol. 16, pp. 1308–1338, Nov. 1995.

[51] J.H. Lin and W.C. Chew, "Ultrasonic imaging by local shape function method with CG-FFT," *IEEE Trans. Ultrasonics, Ferroelectrics, and Frequency Control*, vol. 43, no. 5, pp. 956–969, 1996.

[52] J. Salonen, A. Koski, F. Cameron, K. Forsman, and L. Kettunen, "Solving dense nonsymmetric linear systems arising from integral formulations," *IEEE Mag.*, vol. 32, pp. 1377–1380, May 1996.

[53] C.C. Lu, J.H. Lin, W.C. Chew and G.P. Otto, "Image reconstruction with acoustic measurement using distorted Born iterative method," *Ultrasonic Imaging,* vol. 18, pp. 140–156, 1996.

[54] K. F. Sabet and Linda P. B. Katehi, "A study of dielectric resonators based on two-dimensional fast wavelet algorithm," *IEEE Microwave and Guided wave Letters*, vol. 6, pp. 19–21, Jan. 1996.

[55] B. Z. Steinberg, "A multiresolution study of two-dimensional scattering by metallic cylinders," *IEEE Trans. Antennas Propagat.*, vol. 44, pp. 572–579, April 1996.

[56] P. R. Amestoy, T. A. Davis, and I. S. Duff, "An approximate minimum degree ordering algorithm," *SIAM J. Matrix Anal. Appl.*, vol. 17, no. 4, pp. 886–905, 1996.

[57] G. W. Pan, "Orthogonal wavelets with application in electromagnetics," *IEEE Trans. Mag.*, vol. 32, pp. 659–667, May 1996.

[58] J. H. Lin and W. C. Chew, "BiCG-FFT T-matrix method for solving for the scattering solution from inhomogeneous bodies," *IEEE Trans. Microwave Theory Tech.*, vol. 44, no. 7, pp. 1150–1155, July 1996.

[59] Z. Baharav and Y. Leviatan, "Impedance matrix compression using adaptively constructed basis functions," *IEEE Trans. Antennas Propagat.*, vol. 44, pp. 1231-1238, September 1996.

[60] T. A. Davis and I. S. Duff, "An unsymmetric-pattern multifrontal method for sparse LU factorization," *SIAM J. Matrix Anal. Appl.*, vol. 18, no. 1, pp. 140–158, 1997.

[61] W. C. Chew, J. M. Jin, C. C. Liu, and J. M. Song, "Fast solution methods in electromagnetics," *IEEE Trans. Antennas Propagat.*, vol. 45, pp. 533–543, March 1997.

[62] G. Wang, "Application of wavelets on the interval to the analysis of thin-wire antennas and scatterers" *IEEE Trans. Antennas Propagat.*, vol. 45, pp. 885–893, May 1997.

[63] Z. Xiang and Y. Lu, "An efficient wavelet matrix transform approach for efficient solutions of electromagnetic integral equations," *IEEE Trans. Antennas Propagat.*, vol. 45, pp. 1205–1213, August 1997.

[64] R. D. Nevels, J. C. Goswami, and H. Tehrani, "Semi-orthogonal versus orthogonal wavelet basis sets for solving integral equations," *IEEE Trans. Antennas Propagat.*, vol. 45, pp. 1332–1339, Sept. 1997.

[65] P. N. Brown and H. F. Walker, "GMRES on (nearly) singular systems," *SIAM J. Matrix Anal. Appl.*, vol. 18, pp. 37–51, 1997.

[66] Z. Baharav and Y. Leviatan, "Impedance matrix compression (IMC) using iteratively selected wavelet basis," *IEEE Trans. Antennas Propagat.*, vol. 46, pp. 226–233, February 1998.

[67] W. L. Golik, "Wavelet packets for fast solution of electromagnetic integral equations," *IEEE Trans. Antennas Propagat.*, vol. 46, pp. 618–634, May 1998.

[68] W. Quan and I. R. Ciric, "On the use of multi-*p* hierarchical bases for the solution of integral equations," *Antenna Technology and applied electromagnetics*, Ottawa, Canada, August, 1998.

[69] W. Quan and I. R. Ciric, "Electromagnetic imaging of conducting cylinders by applying a genetic algorithm," *Antenna Technology and applied electromagnetics*, Ottawa, Canada, August, 1998.

[70] W. Quan and I. R. Ciric, "A comparative study of wavelet matrix transform for the solution of integral equations," *IEEE Antennas and Propagation Society Symposium,* Orlando, Florida, July 1999.

[71] W. Quan and I. R. Ciric, "On the semi-orthogonal wavelet matrix transform approach for the solution of Integral equations," *IEEE Antennas and Propagation Society Symposium,* Orlando, Florida, July 1999.

[72] W. Quan and I. R. Ciric, "On the condition number of wavelet transform matrices used for the solution of integral equations," *International Union of Radio Science (URSI) 26th General Assembly*, Toronto, August 1999.

[73] F. Arguello, M. Armor, M. Boo, and J. D. Bruguera, "Algorithm for wavelet transform of Toeplitz matrices," *Electronic Lett.,* vol. 35, no. 10, pp. 775–776, 1999.

[74] H. Deng and H. Ling, "Fast solution of electromagnetic integral equations using adaptive wavelet packet transform," *IEEE Trans. Antennas Propagat.*, vol. 47, pp. 674-682, April 1999.

[75] H. Deng and H. Ling, "On a class of predefined wavelet packet bases for efficient representation of electromagnetic integral equations," *IEEE Trans. Antennas Propagat.*, vol. 47, pp. 1772–1779, December 1999.

[76] D. Zahn, K. Sarabandi, K. Sabet, and J. Harvey, "Numerical simulation of scattering from rough surfaces: a wavelet-based approach," *IEEE Trans. Antennas Propagat.*, vol. 48, pp. 246–253, February 2000.

[77] W. Golik, "Sparsity and conditioning of impedance matrices obtained with semi-orthogonal and bi-orthogonal wavelet bases," *IEEE Trans. Antennas Propagat.*, vol. 48, pp. 473–481, April 2000.

[78] C. Su and T. K. Sarkar, "Adaptive multiscale moment method (AMMM) for analysis of scattering from perfectly conducting plates," *IEEE Trans. Antennas Propagat.*, vol. 48, pp. 932–938, June 2000.

[79] N. Guan, K. Yashiro, and S. Ohkawa, "On a choice of wavelet bases in the wavelet transform approach," *IEEE Trans. Antennas Propagat.*, vol. 48, pp. 1186–1191, August 2000.

[80] R. Loison, R. Gillard, J. Citerne, G. Piton, and H. Legay, "A Multiresolution MoM analysis of multiport structures using matched terminals," *IEEE Trans. Microwave Theory Tech.*, vol. 49, no. 1, pp. 119–127, January 2001.

[81] W. Quan and I. R. Ciric, "Use of wavelets for an efficient solution of electromagnetic scattering by conducting bodies of revolution," *IEEE Trans., Mag.* vol. 37, pp. 3281–3284, Sept. 2001.

[82] I. R. Ciric and W. Quan, "A fast wavelet solution of electromagnetic scattering by dielectric bodies of revolution," *IEEE Trans. Mag.*, vol. 38, pp. 725–728, March 2002.

[83] W. Quan and I. R. Ciric, "Wavelet analysis of wave scattering by 3-D inhomogeneous dielectric bodies, "*Progress in Electromagnetics Research Symposium* (*PIERS*), Singapore, January 2003.

[84] H. Deng and H. Ling, "An efficient wavelet preconditioner for iterative solution of three-dimensional electromagnetic integral equations," *IEEE Trans. Antennas Propagat.*, vol. 51, pp. 654–660, March 2003.